Intrinsic ocean variability modulated by the atmosphere in the Gulf of Mexico : an ensemble modelling study

Beatriz Garcia Gomez

THÈSE

Pour obtenir le grade de

DOCTEUR DE L'UNIVERSITE GRENOBLE ALPES

Spécialité : Océan, Atmosphère, Hydrologie (CEOAH)

Arrêté ministériel : 25 mai 2016

Présentée par

Beatriz Ixetl GARCIA GOMEZ

Thèse dirigée par **Thierry PENDUFF**, Directeur de Recherche , Université Grenoble Alpes
codirigée par **Bernard BARNIER**, Directeur de Recherche, Université Grenoble Alpes

préparée au sein de **l' Institut des Géosciences de l'Environnement**
dans **l'École Doctorale Terre, Univers, Environnement**

Variabilité intrinsèque de l'océan modulée par l'atmosphère dans le Golfe du Mexique: une étude par modélisation d'ensemble.

Intrinsic ocean variability modulated by the atmosphere in the Gulf of Mexico: an ensemble modelling study.

Thèse soutenue publiquement le **17 juillet 2020,**
devant le jury composé de :

Monsieur THIERRY PENDUFF
Directeur de recherche, Université Grenoble Alpes, Directeur de thèse
Madame ANNE MARIE TREGUIER
Directeur de recherche, CNRS/ IFREMER , Rapporteur
Monsieur BRUNO ZAKARDJIAN
Professeur des Universités, Universite Toulon , Rapporteur
Madame NADIA AYOUB
Chargé de recherche, CNRS/ LEGOS, Examinateur
Monsieur BERNARD BARNIER
Directeur de recherche, Université Grenoble Alpes, Co-directeur de thèse
Monsieur ERIC BLAYO
Professeur des Universités, Université Grenoble Alpes, Président

Abstract

The Gulf of Mexico (GoM) is of primary societal and economic importance for the countries that surround it. The ocean circulation and dynamics in the GoM are characterized by an intense mesoscale activity that is mostly associated with the Loop Current (LC) and the eddies that separate from it. Some studies have highlighted the variability of this current system that is driven by the atmospheric variability (i.e. the forced part). Other studies focus on the intrinsic part of the variability, which spontaneously emerges from ocean flows and that has a chaotic behavior. The contributions of atmospheric and oceanic sources of the ocean variability in the GoM are not well known, although this question is central for understanding and forecasting the ocean flows in that region. Our objective is to study the interplay between the ocean intrinsic variability and the atmospheric forcing in the GoM, using a regional 20-year, $1/4^\circ$ 50-member ensemble ocean simulation. We show that at most time scales, the simulated variability approximately matches altimeter observations in magnitude and spatial distribution. Our analyses also suggest that observed time series of Sea Level Anomaly (SLA) are not long enough presently to yield a robust description of the dynamics of the LC, in particular the timing of eddy sheddings. The daily SLA variability is then analyzed probabilistically from ensemble PDFs, and entropy-based metrics that we introduce. We identify regions (Gulf Stream, LC, central GoM, Caribbean Sea) where the subannual SLA variability is mostly intrinsic, with a persistently small sensitivity to the atmospheric forcing. This conclusion holds at annual and interannual periods as well in the first 3 regions listed above. The constraint exerted by the atmosphere on the intrinsic variability fluctuates more in other regions: hurricane and winter storms drive sharp entropy drops along their paths, in particular near the coasts along which subsequent storm surges propagate; interannual forcing anomalies can also exert large constraints on the ensemble members, yielding large-scale entropy anomalies that slowly propagate westward across the Caribbean Sea. The multi-scale oceanic variability in the whole region is thus the complex result of intrinsic/chaotic ocean dynamics modulated by the atmosphere, and can be fruitfully studied using ensemble modelling strategies.

Keywords: Gulf of Mexico, ocean, circulation, variability, intrinsic, atmosphere.

Abstract

Le Golfe du Mexique (GoM) est un bassin océanique d'une importance sociétale et économique primordiale pour les pays qui l'entourent. La circulation et la dynamique océanique dans le GoM sont caractérisées par une activité mésoéchelle intense qui est principalement associée au Loop Current (LC) et aux tourbillons qui s'en séparent. Certaines études ont mis en évidence la part forcée de la variabilité de l'océan dans ce bassin, c'est-à-dire celle qui est contrôlée par la variabilité atmosphérique. D'autres études se concentrent sur la partie intrinsèque de la variabilité, qui émerge spontanément des non-linéarités de la dynamique océanique et qui a un comportement chaotique. Les contributions des sources atmosphériques et océaniques de la variabilité de la circulation océanique dans le GoM ne sont pas bien connues, bien que cette question soit centrale pour la compréhension et la prévision de sa variabilité. Notre objectif est d'étudier l'interaction entre la variabilité intrinsèque océanique et le forçage atmosphérique dans le golfe du Mexique, en utilisant un ensemble de 50 simulations océan-banquise régionales de 20 ans à la résolution de $1/4°$. Nous montrons qu'à la plupart des échelles de temps, la variabilité simulée correspond approximativement aux observations altimétriques en termes d'intensité et de distribution spatiale. Nos analyses suggèrent aussi que les séries temporelles observées de l'anomalie du niveau de la mer (SLA) ne sont pas assez longues actuellement pour fournir une description robuste de la dynamique du LC, en particulier des évènements d'éjection de tourbillons. La variabilité journalière de SLA est alors analysée de manière probabiliste à partir des PDF d'ensemble, et d'une métrique basée sur l'entropie que nous introduisons. Nous identifions les régions (Gulf Stream, CL, centre du GoM, mer des Caraïbes) où la variabilité subannuelle de la SLA est principalement intrinsèque, avec une forte et persistante insensibilité au forçage atmosphérique. Cette conclusion s'applique aussi aux périodes annuelles et interannuelles dans les 3 premières régions mentionnées ci-dessus. La contrainte exercée par l'atmosphère sur la variabilité intrinsèque fluctue davantage dans d'autres régions : les ouragans et les tempêtes hivernales entraînent de fortes chutes d'entropie sur leur trajectoire, en particulier près des côtes le long desquelles se propagent les ondes de tempête induites ; les anomalies interannuelles du forçage peuvent également exercer de fortes contraintes sur tous les membres de l'ensemble, produisant des anomalies d'entropie à grande échelle qui se propagent lentement vers l'ouest à travers la mer des Caraïbes. La variabilité océanique multi-échelle de la région est donc la résultante complexe d'une dynamique intrinsèque chaotique de l'océan modulée par l'atmosphère, et peut être étudiée de manière fructueuse en utilisant des stratégies de modélisation d'ensemble.

Mots clés: Golfe du Mexique, océan, circulation, variabilité, intrinsèque, atmosphère.

Acknowledgements

I want to acknowledge my thesis supervisors Thierry Penduff and Bernard Barnier. Thank you for all your help, knowledge, discussions, and thank you for your patience.

I would also acknowledge Jean-Marc Molines and Jean-Michel Brankart, who were always willing to help me during the development of this work. Thank you infinitely for all you taught me.

Thank you to Julien Jouanno and Julio Sheinbaum, who were also an essential part of this work. Thank you for all your ideas, discussions, and teachings.

I would like to thank Mexico's government and CONACYT for funding for my Ph.D. and this research work. No. CVU 436743.

Thanks to the MEOM group for their welcome and thanks to all the people who always help each other. A special thanks to Josiane, who always makes our academic and administrative life a little easier.

Thank you to all my friends. You have been significant support in the good and bad times, whether you live in the same city or across the world. As always, a special thanks to my best friends, without whom it would have been impossible for me to continue. Thank you: Liz, Rene, Barbi, Chuy, Yai, Ross.

Thank you to my family, who inspires me to be a better person and always supports me. I hope I can inspire you a little.

Specially thank you to my parents, who are my inspiration and biggest support. I love you.

Contents

List of Figures

List of Tables

Chapter 1

Introduction

The general topic of this thesis is the variability of the ocean circulation in the Gulf of Mexico (GoM) and its surrounding basins (Fig.1.1). The state of the ocean in this region and its variability are of major importance for the economy of the surrounding countries (Mexico, Cuba, USA), for the forecast of extreme weather events such that hurricanes, and influences in the meridional transport of heat in the North Atlantic.

The economy of the countries surrounding the GoM takes great benefit from the resources available in the Gulf. Thousands of drilling platforms concentrated in the bay of Campeche and the western Gulf region are extracting oil and gas. The Gulf of Mexico has a rich biodiversity and fisheries are extremely productive, shrimps, oysters, and lobsters being among its largest fish products. Recreation and touristic activities are also a significant part of the economy. The sustainability and productivity of these economic activities are all influenced, to various degrees, by the ocean circulation. Operating the off-shore drilling platforms needs a good knowledge of ocean currents, living resources and touristic activity are threatened by large oil spills as the one that occurred on April 2010 at the Deepwater Horizon platform, and the warm waters present in the Gulf in fall can feed energy to extremely powerful and devastating storms such as the Katrina Hurricane in 2005. The waters of the GoM also receive the freshwater from important river systems and the pollution they transport spreads into the Gulf. Consequently, all economic sectors express a high demand of accurate knowledge, understanding and forecasting ability of the ocean physical properties in the Gulf.

Many of the economic activities occurring in the GoM may also be sensitive to a warming climate, especially those that depend on the rich biodiversity present in the Gulf, but also those that are impacted by extreme storm events. The GoM circulation is fully integrated to the western boundary current system of the North Atlantic (Fig. 1.2) which has a crucial role in the variability of the climate of the Americas, of the North Atlantic and of Europe. Understanding the role of the dynamics occurring in the Gulf in this complex system is thus of importance for an in depth understanding of the North Atlantic circulation and its role in the climate of this part of the world.

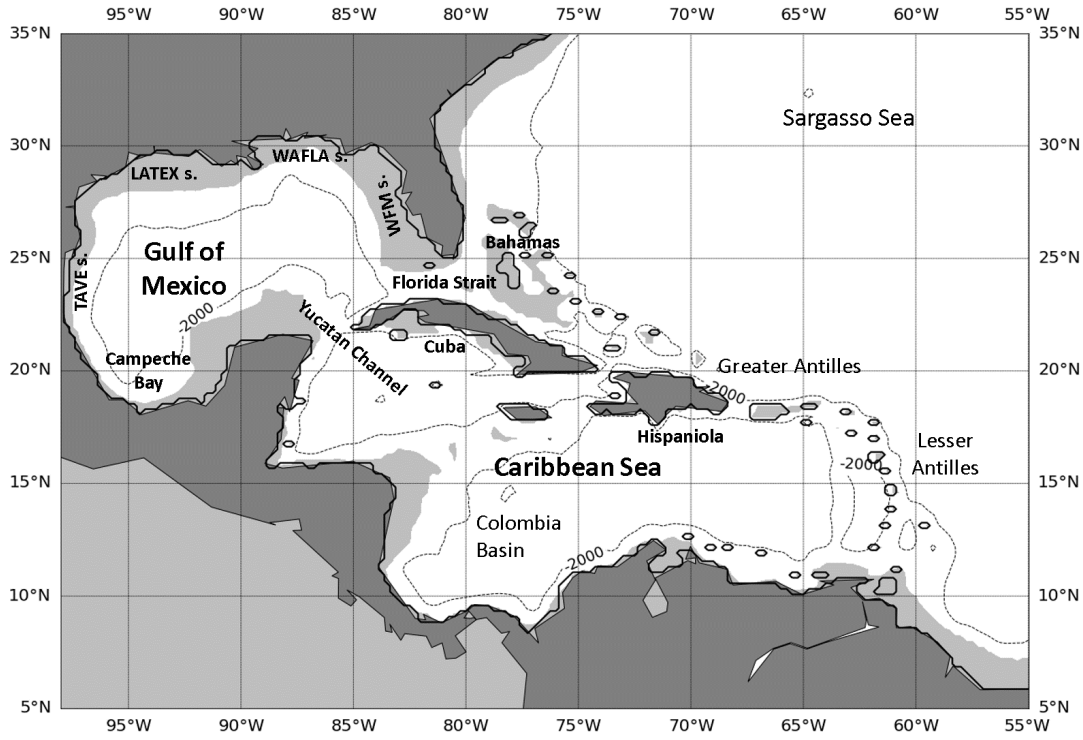

FIGURE 1.1: Map of the west Subtropical North Atlantic Ocean and the name of the main regions. The gray shade represents the waters shallower than 200 m. "s" is the abbreviation of shelf

The GoM belongs to the North Atlantic Basin and represents its westernmost part (Fig. 1.2). It communicates with the Caribbean Sea through the Yucatan Channel and with the western North Atlantic through the Florida Strait. It extends over 1600 km from west to east and 900 km from north to south and covers an area of nearly 1.5 million km2. Its depth is shallow along the coastal continental shelves (200 m) and reaches up to more than 4000 m in the abyssal plain of its central part.

The upper North Atlantic circulation can be schematized in two major components, the horizontal currents which are mainly wind-driven, and a thermohaline meridional cell that involves the transformation of warm to cold water at high latitudes (Schmitz and McCartney, 1993). The thermohaline circulation plays an essential part in the climate variability and has some crucial components in the North Atlantic Ocean. The surface circulation of the North Atlantic (Fig. 1.2) clearly places the Gulf of Mexico in the core of the circulation at subtropical latitudes. The main circulation feature, the subtropical gyre, is constituted by a primary flow that comes from the eastern tropical Atlantic reaching the West with the North Equatorial Current and across the equator with the North Brazil Current. The main flow enters the Caribbean Sea through the

Antilles and enters the Gulf of Mexico by the Yucatan Channel (Johns et al., 2002). The flow into the Gulf is called the Loop Current (LC). From the Yucatan Channel, the LC extends more or less far into the Gulf before exiting through the Florida Straits. The flow continues northward, becoming the Florida current and then the Gulf Stream. The Gulf Stream is one of the major currents of the world ocean. This complete system is also known as the western boundary current system of the North Atlantic, and it is essential as the primary carrier of heat from low to high latitudes.

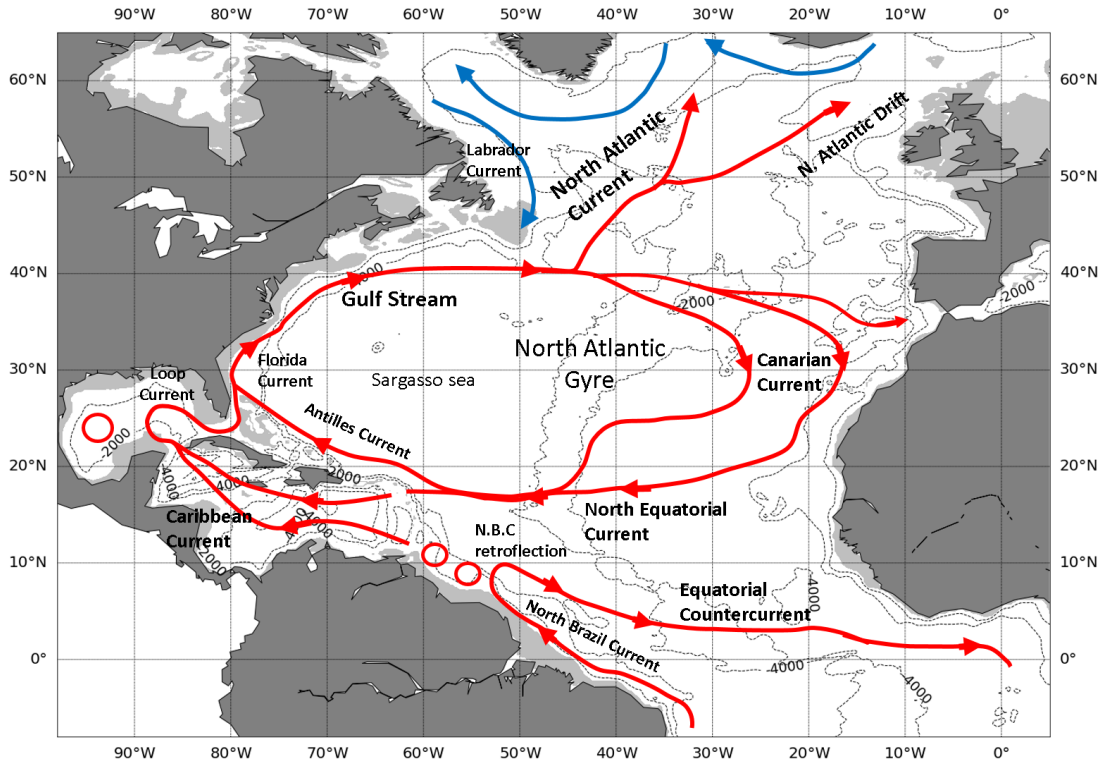

FIGURE 1.2: Map of the North Atlantic Ocean and general representation of the surface currents. Circulation based in Schmitz and McCartney (1993). The grey shade represents shallow waters($<$ 200m). Black dashed lines represent the 2000, and 4000 m isobaths.

The GoM is described as an oceanic basin with a strong turbulent activity associated with a large mesoscale activity (Hamilton et al., 1999). The circulation of the GoM and its variability have been extensively studied and documented. However, to what extent the variability is intrinsic and spontaneously emerges from the ocean or due to the atmospheric forcing remains an open and important question. Several studies suggest that the GoM circulation is mainly forced by the atmosphere (Oey, 2003; Chang and Oey, 2010a; Chang and Oey, 2013). Other studies suggest that the variability in the Gulf is intrinsic and chaotic in some regions (the Loop Current) and forced in others (e.g., the shelf break Leben, 2005; Cardona and Bracco, 2016).

The leading circulation in the Gulf, (as illustrated in Fig. 1.3) is the Loop Current and the anticyclonic eddies that detach from it, called Loop Current Eddies (LCEs) (Hamilton et al., 1999). These eddies, which extend over 800-1000m in the vertical (Hamilton et al., 1999; Portela et al., 2018), travel to the West along three main paths (Vukovich, 2007). While the LCEs travel to the west, they interact with other eddies and with topography (mainly the continental shelves) dissipating anticyclonic vorticity (Hamilton et al., 1999; DiMarco et al., 2005; Vukovich, 2007). The separation of a LC eddy from the Loop Current is a complex event not yet fully understood and challenging to simulate and forecast. Several authors suggest that different processes could be involved in the LC eddy shedding, and we describe them in a following subsection.

The GoM and adjacent oceanic regions are forced by easterly winds whose seasonal variability, some studies suggest, could explain what appears to be a seasonality in Loop Current eddy shedding periods (Chang and Oey, 2010b; Chang and Oey, 2013). The wind-stress curl within the GoM has a well-defined dipolar structure with positive (negative) values in its southern (northern) half (Velasco and Winant, 1996). The mean wind-stress over the southern GoM is thought to be the main mechanism responsible for the cyclonic circulation in the area (Campeche bay). This cyclonic circulation is generally confined (over closed barotropic geostrophic contours, f/H) to the southwestern part of the basin, and takes the form of a quasi-permanent cyclonic eddy which strongly interacts with LCEs and other eddies (Vázquez de la Cerda et al., 2005; Pérez-Brunius et al., 2013).

The wind stress is also thought to be the primary driver of the circulation on the northern and western continental shelves (Morey et al., 2005; DiMarco et al., 2005; Zavala-Hidalgo et al., 2014). The circulation over the GoM continental shelf has a primary seasonal variability, and is spatially divided in four main sectors (Fig. 1.1): the West Florida shelf (WFS), the Mississippi-Alabama-Florida shelf (MAFLA), the Lousiana-Texas shelf (LATEX), and the Tamaulipas-Veracruz shelf (TAVE). The ocean circulation over the shelf has a primary seasonal variability. During fall and winter, the current is mainly southward on the TAVE shelf and westward on LATEX and MAFLA shelves, making a counterclockwise circulation over the whole continental shelf. In spring, the TAVE shelf circulation reverses northward while the LATEX shelf circulation remains westward; these opposing currents generate a zone of convergence. The reversal of the circulation continues during summer extending to the LATEX and MAFLA shelves generating a clockwise circulation. The along-coast circulation in the WFS remains all the year to the north (Morey et al., 2005; Zavala-Hidalgo et al., 2014). As a side note, published in a recent study, Gómez-Valdivia and Parés-Sierra (2020) suggest that the LC

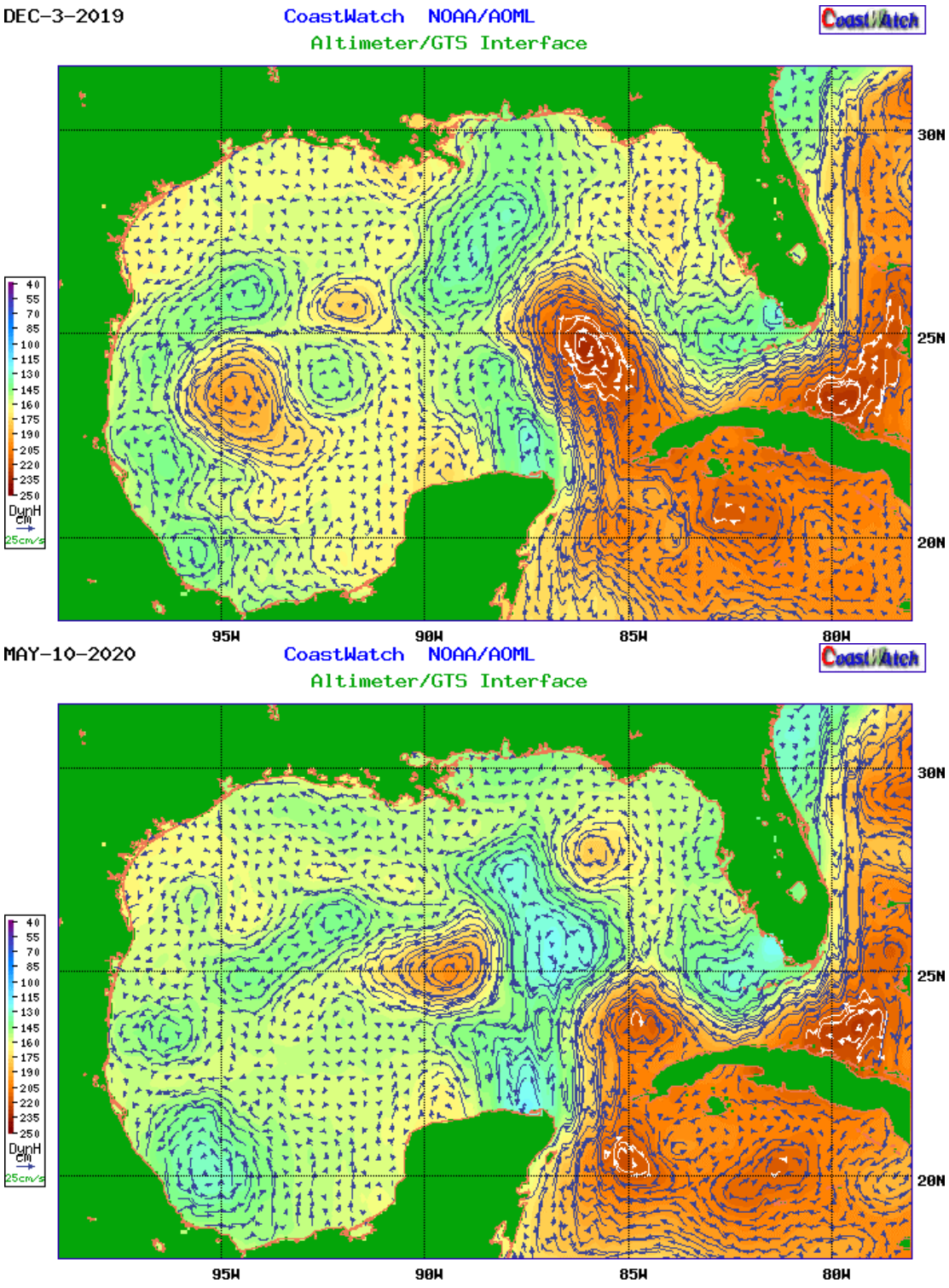

FIGURE 1.3: Instantaneous geostrophic currents (arrows) and Sea Surface Height (color) at two different times in Winter and Spring, illustrating the eddy rich circulation, the Loop Current and the shedding of Loop Current Eddy (From https://www.aoml.noaa.gov/phod/dhos/altimetry.php).

(anticyclonic) eddies arrival substantially influence the TAVE shelf circulation, driving a preferential northward circulation.

Another important feature in the GoM coastal circulation are the storm surges, the amplitude of which is largely influenced by the wind and atmospheric pressure in the region. The greatest storm surges are generally driven by Hurricanes. The storm surge is generated when a hurricane or tropical storm hits the coast and the low pressure generates a rise in the seal level. It has been observed that such storm surges can generate a coastally trapped wave, especially when the storm hits the northern shelf of the GoM (Bilskie et al., 2016). The Gulf of Mexico is also affected by cold fronts from October to May. These cold fronts are associated with strong and cold winds with mainly a southern direction. The fronts do not have the same duration, intensity or penetration in the GoM, most of them only reach the northern part of it (DiMego et al., 1976). These cold fronts in the GoM have been associated also with the generation of coastally trapped waves (Dubranna et al., 2011; Jouanno et al., 2016) and with some cross-shelf transports (Zavala-Hidalgo et al., 2014).

The Loop Current, as part of the current system flowing between the Yucatan Channel and Florida Strait, is important because it is the major feeder for the Gulf Stream which carries the upper limb of the North Atlantic Meridional Overturning Circulation (Cunningham et al., 2007). Several authors described a bimodal state of the Loop Current (LC): a retracted mode in which the LC penetrates through the Yucatan Channel and flows directly through the Florida Straits and an extended mode where the LC penetrates far into the GoM and irregularly sheds an anticyclonic eddy. The variability of the extension and eddy shedding period are not well understood, and there are several hypotheses about the origins of this variability. The shedding period that has been observed is not regular and challenging to predict. Several authors have tried to find a relationship between the period of LC eddy separation and some other remote variables that, to some extent, could provide us with information about a possible future eddy separation. We now present some of the possible variables that have been shown to have a relationship with the LC variability.

Chang and Oey (2010a) found with a numerical experiment that wind-stress is important for the eddy shedding process. Their model driven by a temporally and spatially constant westward wind-stress produced a westward flow over the northern continental shelf and an eastward flow in the central GoM. This eastward flow was found to delay the eddy separation. In a following study, Chang and Oey (2012) suggested that

the seasonality of the eddy separation process could be related to the seasonality of the Trade Winds. Using the statistics of the observed eddy shedding events and regional numerical models, Chang and Oey (2012) found that the greater intensity of the Trade Winds over the Caribbean Sea during summer and winter causes stronger transport through the Yucatan Channel. This substantial increase of the Yucatan Channel transport was also correlated with an extended LC, as found by Oey (2003) and therefore an eddy separation during summer and winter is more probable. In agreement with their previous works, Chang and Oey (2013) suggested that the Yucatan transport has a semi-annual cycle attributed to variations in the wind stress and the meridional SST gradient, and so the LC extension that has a positive correlation with the Yucatan transport.

Bunge et al. (2002) used 7 month of mooring data to test the hypothesis formulated by Maul (1977) and Maul and Vukovich (1993), which states that the growth of the LC should be related to a deep Yucatan transport into the Caribbean Sea. Under the hypothesis that restricts the deep exchanges in the Gulf of Mexico to the Yucatan Channel (no deep flow can exits through the shallower Florida Strait), they found that the cumulative (20 days smoothing) deep transport of the Yucatan Channel was well related to the surface extension of the Loop Current, the LC leading. This was later seen in several decades long model simulations by Nedbor-Gross et al. (2014).

Lin et al. (2009) suggested that the fluctuations in the Yucatan Channel barotropic transport are affected by the interaction between density anomalies associated with the LC intrusion and the topography between Cuba and Florida. At inter-annual time scales, Mildner et al. (2013) associated the internal ocean variability with the Florida Current transport variability rather than wind forcing, and suggest that low transport conditions are associated with the position of the LC and a ring located just north of the Yucatan channel blocking the inflow from the Caribbean Sea.

Candela et al. (2002) suggested a relation between the flux of vorticity through the Yucatan Channel and the LC extension and the eddy detachment events. They observed that the flux of positive vorticity into the GoM preceded an eddy detachment event, while the accumulation of negative vorticity enhanced the Loop Current extension into the Gulf of Mexico.

Chérubin et al. (2006) observed cyclonic eddies in the vicinity of the Loop Current. They suggested that the cyclonic vorticity present causes instability, which leads to an LC eddy separation event. These cyclonic eddies, called Loop Current Frontal Eddies (LCFEs), have been studied in more detail in later studies (Le Hénaff et al., 2012; Jouanno et al., 2016). Nevertheless, these structures have a size approximately of 100 km, and so, a high-resolution model is necessary for their accurate simulation.

The studies cited above clearly demonstrated that the LC extension and the associated LCEs shedding are the dominant features of the GoM variability and that understanding their driving mechanisms is a key to comprehend their role in the ocean dynamics in the Gulf of Mexico. If these studies suggested several possible generating mechanisms of variability, they did not yet permit to build a consensus on their relevance, their relative importance or dominance, and in which way they are related to an external forcing or arise from the ocean dynamics only.

The rationale of the work presented in this thesis has been determined by this lack of consensus. Our study was principally defined by the need to discriminate between the mechanisms of variability that are forced by the atmosphere and those that are intrinsic to the ocean dynamics, and to quantify their respective importance. Such a quantification would help attribute to atmospheric causes the part of the GoM variability that is potentially predictable and not fundamentally random in phase, and to objectively evaluate the (potentially partial, potentially time- and space-dependent) constraint exerted by the atmosphere on the ocean state. This is a complex issue since the intrinsic variability, related to the turbulent nature of ocean flows, is likely chaotic, but could also be partly paced by the fluctuating atmospheric forcing in this region.

The forced oceanic variability can be understood as the response of the ocean to a perturbation initiated by a process external to the ocean, like the ocean response to the atmospheric variability. Various studies demonstrated that in model simulations of the ocean circulation driven even with constant or seasonal atmospheric forcing, another variability (qualified as intrinsic) emerged at periods that are different from those of the atmospheric forcing, through non-linear processes in the ocean. There are idealized and more realistic model studies describing this intrinsic variability (Dijkstra and Ghil, 2005; Drijfhout et al., 2008; Penduff et al., 2011) for different variables and for different temporal scales. These works suggest that the variability in the ocean is the result of a complex combination of atmospherically forced and intrinsic fluctuations. The chaotic variability depends on the initial conditions, and model simulations can also give us an idea of the contributing fraction of the intrinsic variability to the total ocean variability. The interplay between intrinsic and forced variabilities and their contribution to ocean variability is still an open question.

In this work, we describe and investigate the oceanic variability in the GoM and surrounding basins, and its possible origin (forced and/or chaotic). Our objectives are to

disentangle and study the forced and chaotic variabilities within and around the Gulf of Mexico, and to study the impact of the atmospheric forcing on the oceanic chaos. We also have the objective to implement a new methodology to study and describe in a better way the regions where the ocean variability cannot be characterized by Gaussian statistics, and to apply it to study the origin of the variability of the Loop Current.

The thesis is organized as follows. Following this introduction, Chapter 2 describes the data used to addressed our objectives and the methods used and developed in our study. Chapter 3 describes the comparison between the model outputs and different sources of observations. Chapter 4 explains the main results of this work. We describe the ocean surface variability using different methods to investigate the interplay of the intrinsic variability and the atmospheric forcing of the Subtropical North Atlantic. Chapter 5 presents the conclusions and perspectives of this study.

Chapter 2

Data and Methods

This chapter presents the simulated and observational data used in this study. We then present the pre-processing that is applied to both types of data. The methods we use to disentangle the intrinsic ocean variability and the impact of the atmospheric variability from the ensemble simulation is then presented in more detail: a classical approach based on simple Gaussian metrics is first introduced; we then propose a more complex but more statistically rigorous method designed to characterize the constraint exerted by the fluctuating atmospheric forcing on the chaotic ocean variability in the case of variables with non-Gaussian statistics.

2.1 The North Atlantic ocean ensemble simulation

The OCCIPUT project has the objective to simulate, identify and quantify the contribution of the intrinsic and forced variability to the ocean variability at different time and space scales. Among other simulations performed within the project, a 50-member regional ensemble simulation at eddy-permitting resolution (1/4°) has been performed, all the members of the ensemble being driven by the same atmospheric forcing. The intrinsic and the atmospherically- forced parts of the ocean variability are thus simulated simultaneously under a fully-varying realistic atmosphere (Bessières et al., 2017). We describe here the characteristics of the ensemble simulation used in this study and how it differs from other ensemble simulations produced during the same project.

The main data used for this study are the outputs of a 20-years long ocean/sea-ice 50-member ensemble simulation (referred to as the ENSx50-GSL simulation hereafter) performed with the North Atlantic NATL025 model configuration of NEMO (version 3.5). The NATL025 configuration is described in detail in Le Sommer et al. (2009) and in Lucas et al. (2008) and we only summarized here its major characteristics. The horizontal model resolution is 1/4°, i.e. about 27 km at the equator, 9.5 km at 70°N, and allows a partial representation of mesoscale processes and structures in our region of interest. In the vertical 46 geopotential levels are used. The southern and northern

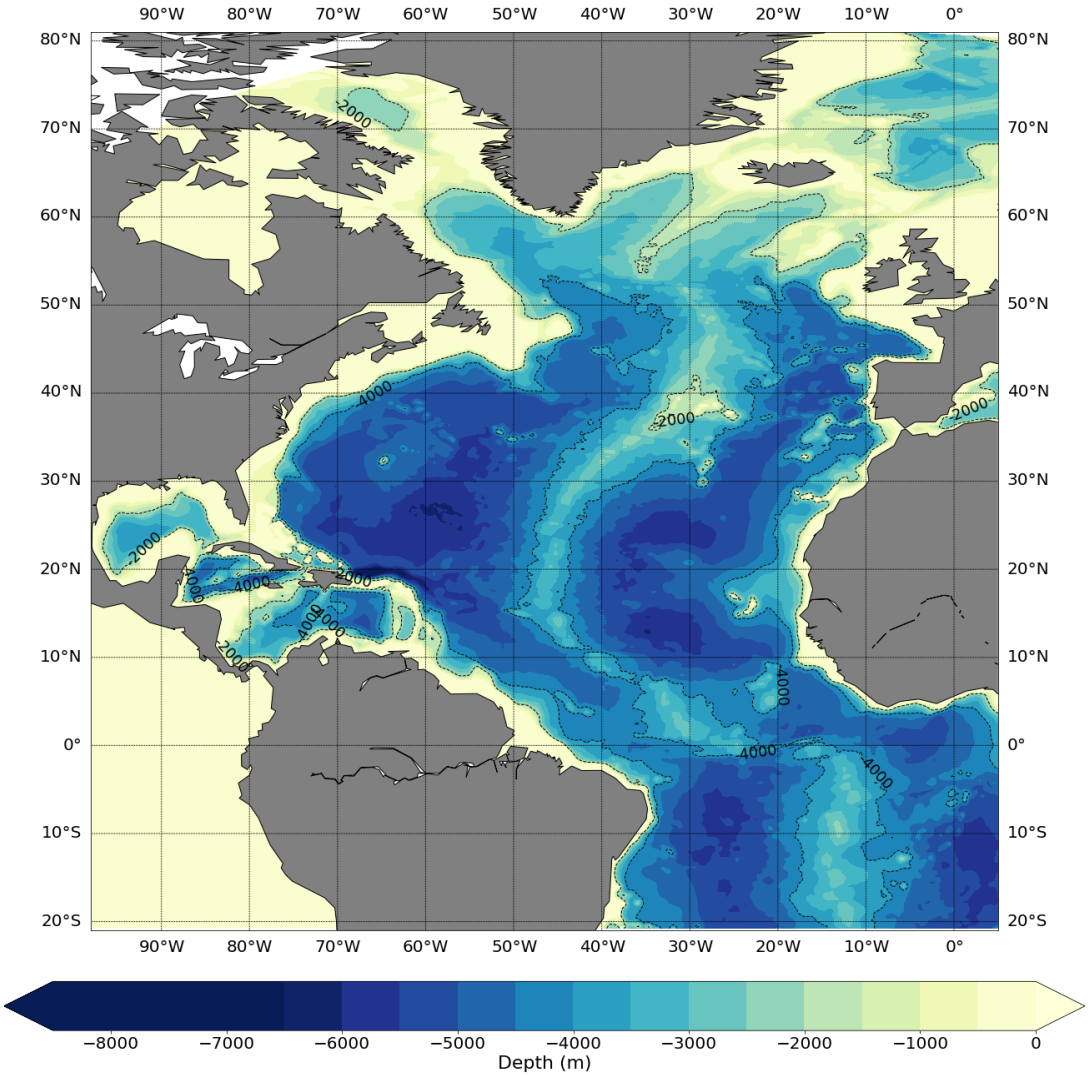

FIGURE 2.1: Map of the NATL025 domain and bottom topography.

boundaries of the domain are set at 20°S and 81°N (2.1), and are treated as solid walls with a 28-gridpoint buffer zone where the ocean state is restored to monthly Levitus climatological conditions (Levitus et al. 1998). In this regional setup, the variability simulated within the domain is isolated from any influence coming from the surrounding ocean. In particular, the intrinsic variability simulated by the model develops within the domain and is not influenced by that which emerges outside of it; this excludes in particular the intrinsic variability that is produced in the Agulhas region and that reaches the northern subtropics in the global OCCIPUT ensemble simulation (see Leroux et al., 2018). The main characteristics of the ensemble simulation are described in table 2.1,

and are similar to those of the global OCCIPUT ensemble simulation described and analyzed in previous related studies (e.g. Sérazin et al., 2017; Leroux et al., 2018).

A one-member spinup is initialized from a temperature and salinity climatology (Levitus et al, 1998) and run for 15 years. The 50 members are initialized from the final state of this spinup (December 31st, 1992). The inter-member dispersion is seeded at the beginning of this ensemble simulation by activating a stochastic perturbation in the equation of state (Brankart et al., 2015) within each member during 1993; this perturbation is then shut off during the remaining 19 years of the ensemble run (until the end of 2012).

The members are integrated in parallel with the same atmospheric forcing based on the Drakkar Forcing Set (DFS) version 5.2 (Dussin et al., 2016). Unlike the OCCIPUT ensemble runs presented in Bessières et al. (2017) and Leroux et al. (2018), this particular regional ensemble simulation was forced at every timestep by the ensemble-averaged air-sea fluxes computed online, in order to remove any artificial damping of the SST spread due to the use of bulk formula. The same exact air-sea (momentum, heat and freshwater) fluxes are thus applied over all members, so that only the ensemble-mean SST is implicitly relaxed toward the prescribed atmosphere: the intrinsic and chaotic component of the SST variability is no longer damped and remains free to develop within each member (Penduff et al., 2020, CMEMS 2020 report). More information about the simulations is given in Bessières et al., 2017.

TABLE 2.1: Main features of the model configuration.

Simulation:	**ENSx50-GSL**
Domain:	North Atlantic ($21^\circ S - 81^\circ N$)
Type:	Ensemble hindcast
Time period:	1993-2012
Spatial resolutio:	$1/4^\circ$
Vertical levels:	46
Output frequency 2D:	1 day
output frequency 3D:	5 days
Atmospheric forcing set:	DFS 5.2 (all time scales)

The 2D variables used in this study are Sea Surface Height (SSH) and Sea Surface Temperature (SST). The 3D variables we used are Horizontal velocity (U and V), Temperature, and Salinity. These 2D and 3D variables are available for each member as successive 5-day averages for 3D variables and daily averages for 2D variables.

2.2 Observations

2.2.1 AVISO-CMEMS Sea Level Anomalies

We use the daily, 1/4° spatial resolution, Sea Level Anomaly (SLA) of the Ssalto/Duacs altimetry product made available by the Copernicus Marine and Environment Service (CMEMS). The product reference in the CMEMS web catalog is "GLOBAL OCEAN GRIDDED L4 SEA SURFACE HEIGHTS AND DERIVED VARIABLES REPROCESSED (1993-ONGOING)". We use the same period as for the simulation: 1993-2012.

Altimetry gives the Sea surface height (SSH) above a reference ellipsoid. The SSH temporal mean is named the Mean Sea Surface (MSS). The difference between SSH and MSS gives the Sea Level Anomaly (SLA), the dynamical part of the signal. Since the model provides a dynamical ocean surface calculated from primitive equations, the reference for the SSH in the model and observations can differ considerably. So, we use the SLA in both cases to compare model results and observations. We interpolated the data from the original observed grid to the model grid for easy data comparison.

2.2.2 Florida transport

The Atlantic Oceanographic and Meteorological Laboratory from the National Oceanic and Atmospheric Administration (NOAA) continuously monitors the western boundary current of the Subtropical North Atlantic. Measurements of the Florida current are of interest here since this current connects the Gulf of Mexico and the Gulf Stream.

The Florida Current daily mean transport, between northern Florida and the Bahamas (27° N), has been measured continuously since 1982 by submerged submarine telephone cables (Baringer and Larsen, 2001). In addition, seasonal research cruises are held each year. The cruises' data provides information for calibration of cable measurements, and temperature and salinity sections in the region that are used to study the evolution of water properties within the Florida Current. In this study we use the cable measurements from 1993 to 2012, and we compare qualitatively the velocity and temperature sections from the annual cruise reports.

"The Florida Current cable and section data are made freely available on the Atlantic Oceanographic and Meteorological Laboratory web page and are funded by the DOC-NOAA Climate Program Office - Ocean Observing and Monitoring Division.": www.aoml.noaa.gov/phod/floridacurrent/

2.3 Data pre-processing

2.3.1 Non-linear detrending

As a first step, our observational and model data are detrended non linearly with a LOWESS high-pass filter with a cutoff frequency of $T = 20$ years. LOWESS (locally weighted scatterplot smoothing) is a regression method for smoothing a scatterplot with a polynomial fit of the data using weighted least squares (Cleveland, 1979). In this work, we use a span of 0.6, which means that the data subset used for the weighted least squares is 0.6 times the time series's length. We use a 5th-degree polynomial fit to capture the large trend curve or the very low-frequency curve. We remove this curve from the total time series, which retains the frequency higher than our frequency cutoff. This operation removes geophysical and numerical trends and signals whose periods are longer than our 20-year simulation length. This non-linear detrending method ensures that all subsequent statistics are computed on a precise range of time scales (2 days to 20 years) without any contamination by unresolved time scales.

We observe (see fig. 2.2) that the members may have significantly different trends, so we detrended each member separately. Detrending each member separately also removes the intrinsic variability at low frequencies that are not fully resolved in our 20-year long simulation. Figure 2.2 shows an example of the 50 time series before and after the detrending process. During the process of detrending, we also subtract the average value of the time series, so from here on we will work with anomalies of the variable in question, unless otherwise indicated.

2.3.2 Time scale splitting

After detrending the time series, we obtain what we call the 'detrended' (or "all time scales") variability. We then split the time series into three different ranges of time scales to analyze them separately.

- **Mean seasonal cycle (MSC).** The mean seasonal cycle is calculated for each of the 50 members by averaging each day of the 20 years; the 29 of February of the leap-years is ignored. So the MSC is represented by a one year (365 days) time series.

- **Low-frequency (LF).** After the MSC is removed from the total, we low pass filter the time series by applying a Lanczos filter with a cutoff frequency of 1.8 years. The cutoff frequency is chosen to select the interannual variability.

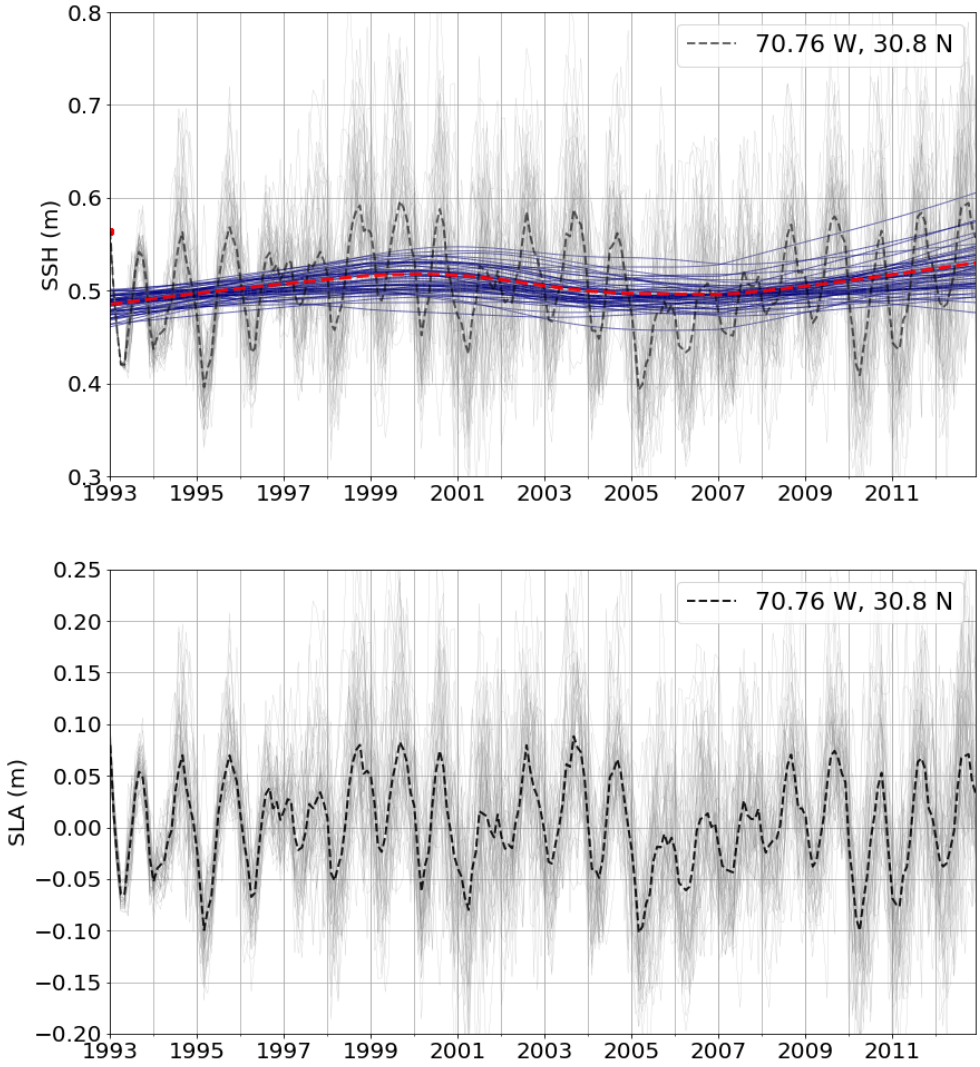

FIGURE 2.2: Time series of the 50 members (gray lines) before (upper panel) and after (lower panel) the detrending process. The blue lines represent the trend of different members, and the red line represents the trend of the ensemble-mean.

- **High-frequency (HF).** After filtering and removing the Low-frequency, the remaining time series contains the High-frequency data.

The methodology described above is applied to all variables used in this study (SSH, SST, velocity, temperature). Derived variables (such as transports) are computed first from raw model data, then they are detrended and split in the same ranges of time scales. Due to the side effects of the Lanczos filter, the LF and HF time series are only 18 years long (1994-2011).

After detrending the SSH time series, we obtain sea level anomalies (SLA) the variable we mostly work with in this study. We add the temporal mean SSH back to the SLA time series to reconstruct the daily SSH field, a variable that is needed to compute additional metrics that we present in the next section.

2.3.3 Loop Current length

The SSH evolution in the Loop Current area allows to characterize the extension of the Loop Current at the surface and detect LC eddy shedding events. However, the SSH evolution at just one location may not be adequate to follow the complete process of a detachment of an eddy from the Loop Current. Instead, we use the length of the LC as a metric to describe some kinematic characteristics of the Loop Current and detect eddy shedding events.

For the computation of the LC length, we use the SSH instead of the SLA. In this case, we use the SSH from the model, and for the observations, we add the ensemble and temporal mean of the model SSH to the altimetry observed SLA. We compute the length of the LC as follows, similarly to other studies.

- We subtract from daily SSH time series at each grid point the daily spatial average of SSH over the Gulf of Mexico. This removes in particular the large-scale SSH changes over the basin , in particular the steric signal associated with the seasonal heating of the mixed layer, and that can affect the estimation of the LC length. The steric signal appears to have an annual cycle with an amplitude that varies between 8 to 10 cm depending on the member.

- We follow the methodology proposed by Leben (2005), adapted to our model results, to identify the Loop Current length with a MATLAB code:

  1. Search the 15 cm SSH contour, which we identified as a proxy for the velocity core of the LC, in the area [21.75° − 28.5°N and 80.25° − 89.75°W].
  2. Save the coordinates of the 15 cm SSH contour.
  3. Compute the length of the LC by summing the distances between the coordinates of the 15 cm contour.

- We find the westernmost longitude and northernmost latitude coordinates of this 15 cm contour, to determine the penetration of the LC into the Gulf.

We applied this method to all SSH time series, providing time series of the LC length, the westernmost longitude, and the northernmost latitude. This is applied to all members separately. Figure 2.3 shows an example of the region (black box) where the LC

length is calculated. Letters A and B represent the beginning and the end of the 15 cm SSH contour considered to calculate the LC length. The letters C and D represent, what would be in this example, the location of the northernmost latitude and westernmost longitude, respectively.

2.4 Data processing

2.4.1 Loop Current derived metrics

We compute some kinematic parameters of the LC with the purpose to assess the model realism and describe some characteristics of the simulated LC.

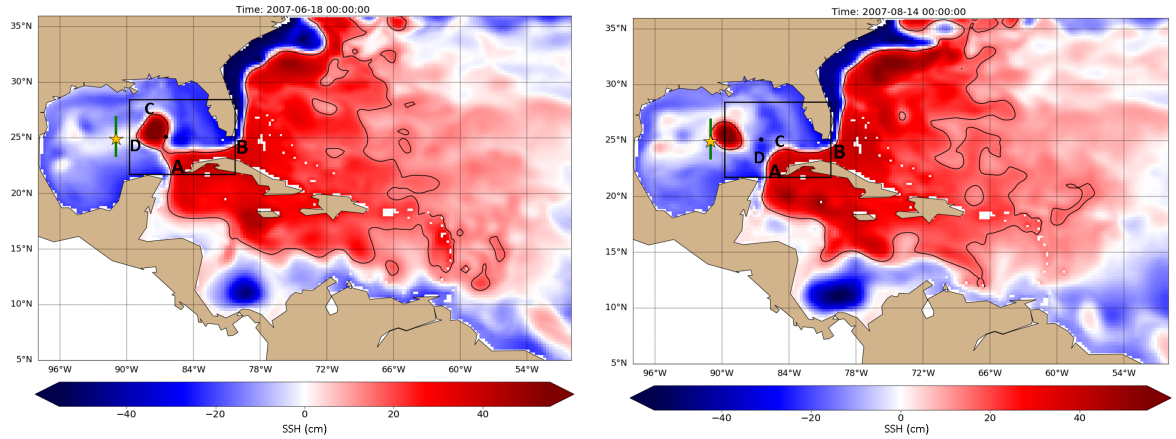

FIGURE 2.3: SSH maps during and after an eddy shedding. The green line is where the average times series of SSH at 91° W is observed. Orange dot represents the location where the SSH time series is observed for the arrival of an eddy(91° W ,25° N). The black box represents the region where the 15 cm SSH contour (black contour) is searched. Letters A and B represent the beginning and ending of the 15 cm SSH contour considered for LC length computation. Letter C represents the location of the northernmost latitude. Letter D represents the westernmost longitude.

We calculate the **dates of eddy detachments or separation events**: We save the date when sharp drops occur in the LC length, which corresponds to eddy separation events. The eddy separation process is noisy, meaning that there can be several detachments and reattachments of the eddy and the LC during the process. These features indeed have been observed, probably influenced by the interaction with other eddies that surround the LC (e.g. Lugo-Fernández et al., 2016). These repeated reattachments may also be due to artifacts in the method since the algorithm uses only one SSH contour that does not always capture the LC core. Other methods have been proposed; for example,

Dukhovskoy et al. (2015), who proposed a method based on a spatial Kalman filter applied to SSH gradients, which helped improve the identification of the LC core, but the method did not bring clear improvement in the eddy detachment identification. This last point is important when discussing eddy separation dates, which may differ from one study to another due to the different definitions.

We calculate the **eddy separation period**, which we defined as the time lap between consecutive eddy separation events. Any detachment that lasts less than 45 days is considered as a re-attachment and not as a separation. We use a complementary criterion to identify "true" eddy separation events from attachments and re-attachments. The time series of the SSH in the western part of the Gulf is looked up and used to confirm that an eddy has indeed separated and propagated. We use the time series of the SSH at two specific locations west of 90°W. The first one is the pointwise SSH at 91°W - 25°N. The second is the meridionally averaged SSH from 24.5°N to 27°N at 91°W. The criterion is as follows: when the SSH of any of these two time series gets above 15 cm, we consider that a detached LC eddy is arriving to the area, and therefore the eddy has detached from the LC. When this criterion is not fulfilled, we do not consider the LC length drop event as a true shedding event.

Figure 2.4 shows an example of the time series of the LC and SSH length at 91°W, which is described above to define the eddy separation events properly. As we can observe in the time series of the LC length, there are events (e.g., 2009/12) where there seems to be a detachment and reattachment of an eddy since the length of the LC presents a sharp drop and a sudden increase during only a few days or weeks. We also observe that the SSH at 91°W, reaches maxima a few weeks or months after sharp drops in the LC length, that it is not precisely at the same time after each event, indicating that the LC eddies have different translation velocities.

Comparing the date of arrival at 91° W with the date estimated from the sharp drops seen in the LC length, allows us to keep only the dates of complete sheddings. Figure 2.5 shows the histogram of eddy separation periods computed with the data obtained from the 91° W SSH method (upper panel), and the data from the drops in LC length method (lower panel). We observe that the number of events obtained with each method is very similar (SSH: 1125, Length:1138) as well as the distribution of periods. We will discuss in section 3.1 how the periods of eddy separation of the LC obtained with our methods, compared to the ones observed in other studies.

We also kept the month of the date of the eddy separation to further analyze the

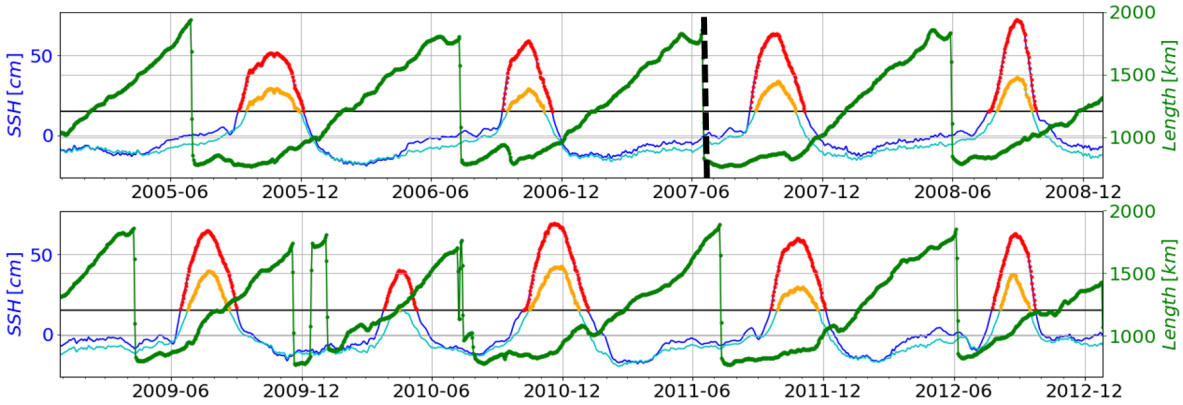

FIGURE 2.4: Loop Current length time series (green line). Time series of SSH at 91° W and 25° N (blue) and the meridional average SSH at 91° W (cyan). The red and orange dots, represent when the SSH time series is above 15 cm. The black dotted line represents the eddy shedding event observed in figure 2.3.

possible seasonality of the process. After the eddy separation occurs, the LC retreats to the south. The latitude of intrusion of the LC at this moment is called Latitude of retraction. Before an eddy separation occurs, the Loop Current is at its maximum extension, the northernmost latitude at this date is what we call maximum Latitude of the LC. The features of the retraction and maximum latitudes are further analyzed in the following.

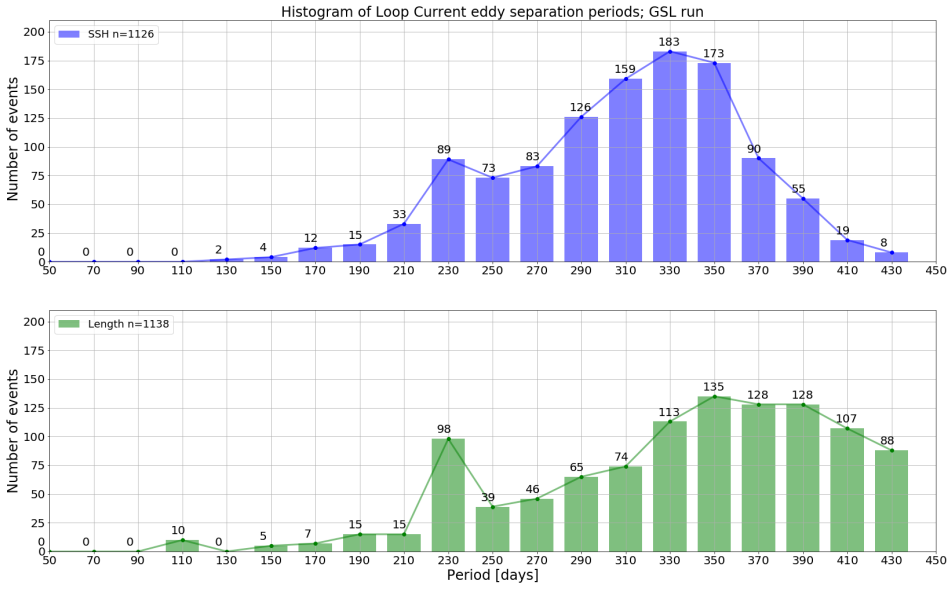

FIGURE 2.5: Eddy separation period histogram computed from all days and all ensemble members. Computed with the SSH at 91° W (upper panel) and with the length of the LC (lower panel).

2.4.2 Sections and transports through the Yucatan Channel and Florida Straits

The main entry of water into the Gulf of Mexico occurs through the Yucatan Channel (YC), and the main exit of water between Florida and Cuba (FC). After leaving the GoM, the flow heads north through the Florida-Bahamas(FB) Strait, which is constantly monitored given its importance in the passage of the main feeder of the Gulf Stream; these data provide a good source of observations to asses the model. To better understand the Loop Current system, its relationship with the Caribbean Sea and the Gulf Stream, we calculate the volume transport across the Yucatan Channel and Florida Straits. The position of the sections is shown in figure 2.6.

The channels at the GoM boundaries (Yucatan Channel and Florida-Cuba strait) have a different maximum depth (YC:$\sim$ 2100 m; FC: $\sim$ 800 m). This means that only part of the water that enters in the YC can exits through the FC channel. Assuming mass conservation, waters denser than the densest water in FC can only enter and exit through the YC. Therefore, it is useful to split the water volume that can exit by the FC section and that which exits to the Caribbean Sea by the YC deep part of the section. To split correctly the water volume, we compute the temperature-salinity (T-S) diagrams in the FC section. We observed in the T-S diagram (e.g., fig. 2.7) that the density of the densest water at the FC, depends mainly on temperature: then splitting the water volume transport by isotherms is adequate. The coldest water observed in FC within all members and all time steps, was 5.2$^{\circ}C$, so we split the Yucatan Channel in two layers: above and below the 5.2$^{\circ}C$ isotherm, within each member and every 5 days (the time sampling of the model simulation output).

We calculated the time series of the volume water transport at each section (Upper Yucatan, Deep Yucatan, Florida-Cuba, and Florida-Bahamas). As mentioned before, each of these time series is detrended and split into its mean seasonal, low-frequency and high-frequency components.

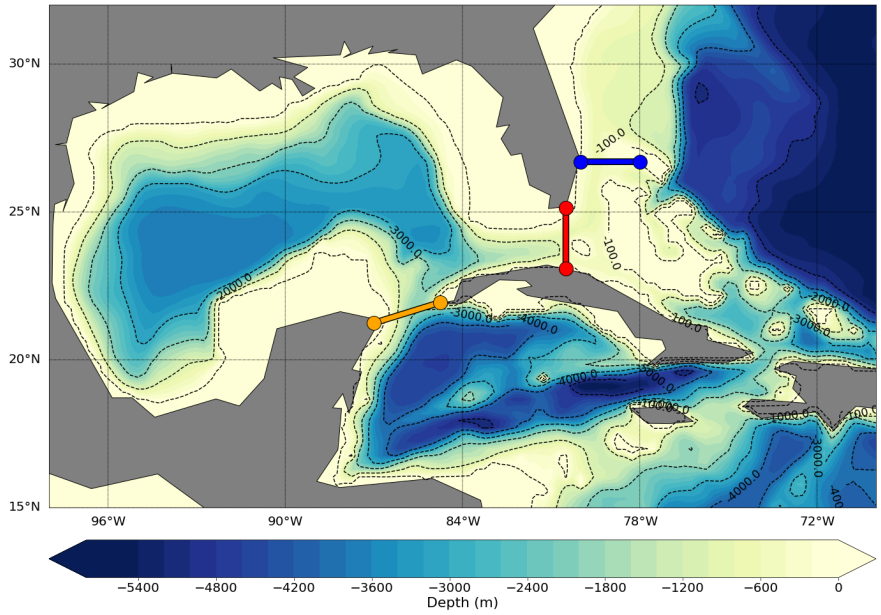

FIGURE 2.6: Map of the region of study. The bathymetry of the region is shown in color. The sections are represented by lines and the beginning and the end is indicated by color dots. Orange for Yucatan section, red for Florida-Cuba and blue for Florida-Bahamas section.

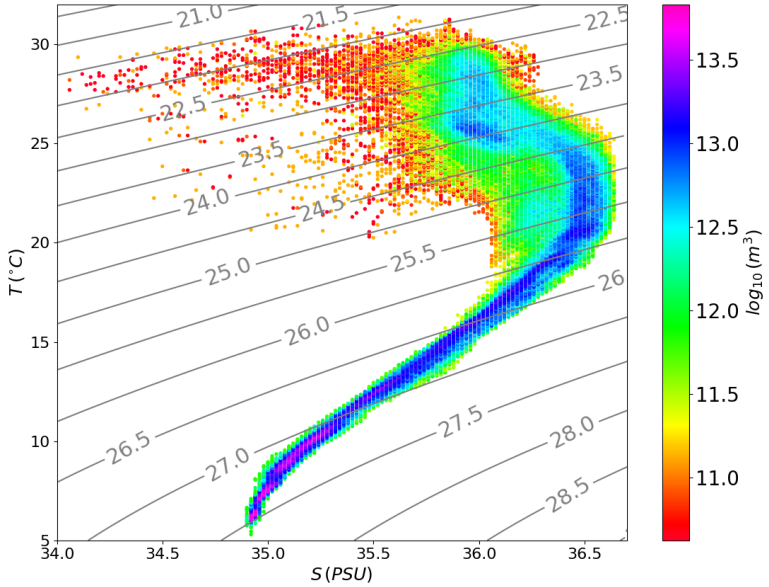

FIGURE 2.7: T-S census (water volume) diagram at Florida-Cuba strait for member 21 in the period 1993-2012.

2.5 Methods

2.5.1 Gaussian metrics: Intrinsic and Forced variability definition

In the first works where the OCCIPUT global ensemble-simulation data were analized, the intrinsic and forced variability of the ocean heat content and the Atlantic Meridional Overturning Circulation were separated and quantified in terms of mean and standard deviation (Sérazin et al., 2017; Grégorio et al., 2015; Leroux et al., 2018). In this work we disentangle the intrinsic and forced variability as proposed by Leroux et al. (2018). Let us consider a variable $f_n(t, \overrightarrow{x})$ from the ensemble, where index $n(n = 1, 2..N)$ indicates the member ensemble, $t(t = 1, 2, ..T)$ indicate the time series, and $\overrightarrow{x} = (x, y, z)$ indicates the location in space. We define the ensemble mean bracket operator $\langle\rangle$ at a given time and location by:

$$\langle f(t, \overrightarrow{x})\rangle = \frac{1}{N}\sum_{n=1}^{N} f_n(t, \overrightarrow{x})$$

and the time mean (overbar operator) of a given member by:

$$\overline{f_n(t, \overrightarrow{x})} = \frac{1}{T}\sum_{t=1}^{T} f_n(t, \overrightarrow{x})$$

The variable $f_n(t, \overrightarrow{x})$, can be decomposed as:

$$f_n(t, \overrightarrow{x}) = \langle f(t, \overrightarrow{x})\rangle + f'_n(t, \overrightarrow{x}) \tag{2.1}$$

where $\langle f(t, \overrightarrow{x})\rangle$ is the ensemble mean at a given time and location, and $f'(t, \overrightarrow{x})$ are the $n = 1, N$ intrinsic components (or perturbations around the ensemble mean) at the same time and location. We define the temporal-variance σ^2, applied to the ensemble mean as:

$$\sigma^2(\overrightarrow{x}) = \frac{1}{T-1}\sum_{=1}^{T}[\langle f(t, \overrightarrow{x})\rangle - \overline{\langle f(t, \overrightarrow{x})\rangle}]^2 \tag{2.2}$$

where the overbar is the time average over the whole period of the simulation. This variance being shared by all members, the forced variability, $\sigma_F(\overrightarrow{x})$, is defined by:

$$\sigma_F(\overrightarrow{x}) = \sqrt{\sigma^2(\overrightarrow{x})} \tag{2.3}$$

We define $\varepsilon^2(t, \overrightarrow{x})$ as the time-varying unbiased ensemble-variance operator applied to the intrinsic components $f'_n(t, \overrightarrow{x})$. It gives:

$$\varepsilon^2(t, \overrightarrow{x}) = \frac{1}{N-1} \sum_{n=1}^{N} f'_n(t, \overrightarrow{x})^2 \tag{2.4}$$

This parameter quantifies the dispersion among ensemble members, and the intrinsic variability, $\sigma_I(\overrightarrow{x})$, is defined by:

$$\sigma_I(\overrightarrow{x}) = \sqrt{\overline{\varepsilon^2(t, \overrightarrow{x})}} \tag{2.5}$$

The total variability within member n is the temporal variance of $f_n(t, \overrightarrow{x})$

$$\sigma^2_{T_n}(\overrightarrow{x}) = \frac{1}{T-1} \sum_{t=1}^{T} [f_n(t, \overrightarrow{x}) - \overline{f_n(t, \overrightarrow{x})}]^2 \tag{2.6}$$

and it can be shown that the total variance, $\sigma^2_T(\overrightarrow{x})$, averaged over the ensemble is the sum of intrinsic and forced variances:

$$\sigma^2_T(\overrightarrow{x}) = \langle \sigma^2_{T_n}(\overrightarrow{x}) \rangle = \sigma^2_F(\overrightarrow{x}) + \sigma^2_I(\overrightarrow{x}) \tag{2.7}$$

In previous analyses of the OCCIPUT ensemble runs (e.g. Sérazin et al., 2017; Leroux et al., 2018) where this definition is used, the usual metrics give relevant and accurate information about the variability. As the atmospheric forcing is the same for all members, the ensemble mean represents the contribution from the forced variability to the total variability. The spread of the members represents the intrinsic variability contribution to the total variability. However, this is not the case for all the variables and regions considered in the outputs of the OCCIPUT ensemble simulation.

In general for most of the variables, and in most of the regions around the world, the time-varying ensemble PDFs remain close to Gaussian . Huot (2016) showed however, that there are regions in the north Atlantic where the ensemble PDFs of the SSH are not Gaussian, so that the use of mean and standard deviation will not provide a complete and accurate description of the ensemble behavior.

Figure 2.8 shows the daily SLA time series from the 50 members at two different locations in the Gulf of Mexico. In the first panel, we observe that all the members (grey lines) have a rich variability in time; despite their identical forcing, all the members simulate a different state at each time step, but share a common variability that is well

captured by the ensemble-mean (black line). If we construct the PDF using the SLA from all time steps and all members, we obtain a quasi Gaussian distribution (panel next to the time series); daily ensemble PDFs are also very close to Gaussian most of the time. In the second panel we observe that in the Loop Current the model produces members with high and low values of SLA at the same time. The variability in time shows that the SLA oscillates with high and low values, and it is clear that this behavior is not well represented by the ensemble-mean, that has a small variability in time. The PDF build at this location from all days and all members is clearly bimodal, corresponding to the two most frequent states. More important, the daily ensemble PDFs of SLA values at this location exhibit a similar bimodal distribution: representing the sea level variability at this location only with the ensemble mean and variance will be poorly accurate.

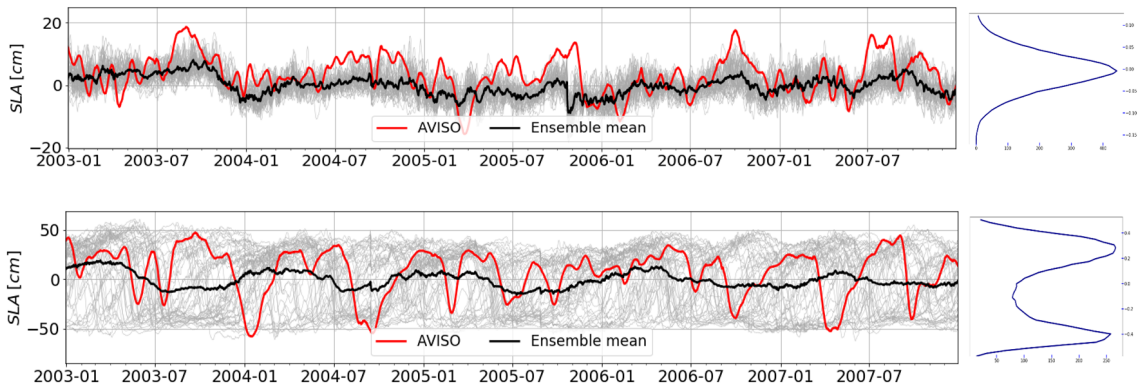

FIGURE 2.8: SLA in the Yucatan channel (upper) and Loop Current(lower) in the period 2008-2012. Grey thin lines represent SLA of each member. The black thick line represents the ensemble-mean SLA. For reference to the actual variability, observations from altimetry are represented in red. Right panels corresponds to the PDFs at each location.

We observed that several locations in the region exhibit non-Gaussian PDFs, and as a consequence, the ensemble-mean does not represent adequately the forced variability. For these reasons, we propose to use a different approach that does not assume that daily PDFs are Gaussian, in order to study this region and the interplay between the intrinsic and forced variability.

2.5.2 Non-Gaussian metrics: Entropy

We now propose new metrics and methods to describe the evolution of non-Gaussian ensemble distributions and characterize the intrinsic variability and the imprint of the atmospheric forcing on the oceanic variability in the general case (Gaussian or not).

Entropy definition

Information entropy is a concept introduced as part of the 'Information theory' by Shannon in 1948. His definition of entropy is analogous to the one used in the statistical mechanics to define thermodynamical entropy. In both cases, it is a measure of the uncertainty in the system. In this study, we use mainly two elements of the information theory (Cover and Thomas, 2006):

Entropy: is a measure of the uncertainty associated with a random variable; it is also a measure of the amount of information required on average to describe a random variable.

$$S(P) = -\sum_{i=1}^{M} P_i log_b P_i \tag{2.8}$$

where P_i is the probability to find the random variable (assumed to be discrete) in state i, among the M possible states; and b is the basis used to compute the logarithm. By definition, the unit of S depends on the choice of b (Cover and Thomas, 2006). If $b = e$ (as in this study), S is expressed in "nats".

Maximum entropy: it is a special case which results from a uniform probability, which yields maximum uncertainty. In the case of a uniform PDF (i.e. the probability to find a given state is the same for all states, which correspond to the distribution of a 'white noise" process), the uncertainty is maximum. In that case, the entropy given by Eq. 2.8 is maximum.

Let us consider only one variable of the simulation and for simplicity, also only one gridpoint. All the values obtained in time and from all members represent all the possible states of the system at this point.Meelting all these values in a single data set (i.e., without the metadata that allows to know which time and member they belong to) includes information on all possible values of the variable but minimum information on the way it varies. The PDF built with these values includes all possible information, and we consider it as a reference PDF noted Q. The entropy of this reference PDF is the maximum possible entropy value for the system described by the ensemble over that period.

We now build a daily ensemble PDF (P) and we observe its evolution in time, we have added information by including the variability over time. If we compare the instantaneous PDF P with the reference PDF Q using entropy based metrics, we measure the information provided by the forcing about the daily state of the system. In this

work, to simplify the comparisons between the reference PDF Q and a PDF that varies over time, we construct the reference PDF as a discrete distribution by considering discrete bins of the continuous random variable. For that, we use quantiles (quartiles or deciles) to define the bins of Q so that the reference PDF Q is a uniform probability. In this way, we obtain a reference PDF Q with maximum entropy that is easy to calculate ($S(Q) = S_{max} = -\sum_{i=1}^{M} Q_i log_b Q_i = log_b M$, M being the number of bins).
Similarly, to simplify, we normalize the entropy of the instantaneous PDF P by the entropy of Q, thus obtaining a value that varies between zero and one, and that evolves in time.

$$S_{ins}(P) = -\sum_{i=1}^{M} P_i log_b P_i / log_b M \tag{2.9}$$

By observing how this entropy varies in time, we can evaluate how much information is gained at each time step, that is, if the entropy (S_{ins}) is minimal, we have an event in which all the values of the ensemble represent the same state. On the contrary, if entropy (S_{ins}) is maximum, it means that no information is gained from the synoptic forcing and that the values can represent any state of the system.

In the ensemble simulation, the atmospheric forcing brings time-varying constraints and provides information to the system in the ocean. Time-varying values of $S_{ins}(P)$ thus measure the daily "intrinsic fraction of the oceanic variability, i.e. the instantaneous contribution of the intrinsic oceanic (chaotic) processes to the daily oceanic state. When this value is close to zero, it means that the information provided by the atmospheric forcing is maximum, while if the entropy value is close to one, the variability is mainly intrinsic with barely any constraint from the atmospheric forcing.

The use of entropy allows us to describe and study in a better mathematically-grounded way a variable that has or does not have a Gaussian distribution. Also, this metric does not assume that the forced and the intrinsic variabilities are independent: instead, the entropy provides us information about how the atmospheric forcing modulates the intrinsic variability. A third benefit is that this metric provides time-varying information, unlike σ_I and σ_F that do not.

Entropy computation

The following methodology is applied to compute the entropy from the ensemble simulation:

- We compute the PDF from the whole time series and all members, at every grid point and for every variable. This PDF is the reference PDF (noted Q).

- We calculate the deciles of the reference PDF: we divide the sorted data of the reference PDF into ten equal parts, so that each part represents 1/10 of the sample. Using bins with non-uniform widths makes the reference PDF equivalent to a uniform distribution, and as explained before, it yields maximum entropy.
- We compute the maximum entropy:

$$S_{max} = -\sum_{i=1}^{M} Q_i log_n Q_i = -\sum_{i=1}^{10} \frac{1}{10} log_n(\frac{1}{10}) \tag{2.10}$$

- We compute the instantaneous ensemble PDF (P) using the previous deciles as bins of the PDF. So we obtain a PDF at each time step and gridpoint.
- We compute the entropy of the instantaneous PDF:

$$S_{in}(x,y,t) = -\sum_{i=1}^{10} P_i(x,y,t) log_n P_i(x,y,t) \tag{2.11}$$

- We normalize the instantaneous entropy by the maximum entropy to obtain the intrinsic fraction. For simplicity, the resulting metric $S(x,y,t)$ will be called "entropy" hereafter.

$$S(x,y,t) = S_{in}(x,y,t)/S_{max} \tag{2.12}$$

The entropy $S(x,y,t)$ varies between 0 and 1, and as we explained before, measures the intrinsic fraction of the variability. A zero entropy characterizes an ensemble state where all the members fall in the same decile; in this case, the disorder is minimum, and the atmospheric constraint on the ocean is maximum. On the other hand, if $S = 1$, the instantaneous PDF equals the reference PDF, meaning that the oceanic disorder is maximum, and the atmospheric constraint is null.

Figure 2.9 shows a graphic representation of the meaning of different values of entropy: the reference PDF in blue represents all the possible values that a given variable can take. In red, green and black are shown three possible 'instantaneous' PDFs. The red and black ones have the same averages but different standard deviation; the black PDF occupies two deciles, so its entropy is lower than the red one (represented by four deciles); the difference between entropy values is just due to different spreads. In the other case, the red and green PDFs have the same shape and standard deviation, but different averages. The red instantaneous PDF has a mean close to the mean of the reference PDF, and it is represented by four deciles; meanwhile, the green PDF sits in an extreme regime and just occupies two deciles. This means that the red PDF has a value

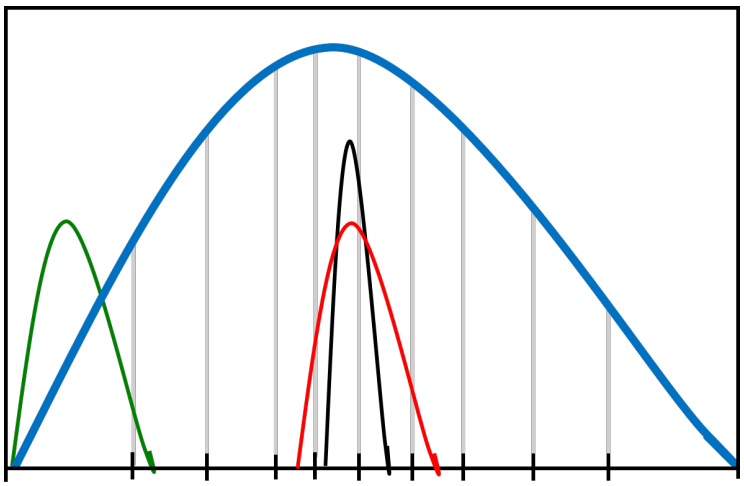

FIGURE 2.9: Graphic representation of different relative entropies. The blue PDF represent the reference PDF. The black lines at the bottom represents the edges of the r-deciles. The red and green instantaneous PDFs have the same distribution, but different mean. The black and red instantaneous PDFs have same average, but different standard deviation.

of entropy higher than the green PDF, even though their distributions are similar. Based on this description, the values of entropy can be interpreted as a measure of the 'information' brought by the atmospheric forcing at a given time about the oceanic state and not only as a measure of the spread.

Accuracy of the entropy metric

It is important now to assess whether time-varying entropy can be accurately computed at daily frequency from the available data (50 samples per day), or if we need to accumulate several consecutive days of data to decrease the sampling error and thus compute entropy at lower frequency. The examination of reference and instantaneous ensemble PDFs at various locations and days showed that most of these PDFs may be approximated as Gaussian, skewed, or bimodal (double Gaussians) distributions. So we first constructed 4 types of analytical PDFs:

- Two Gaussian PDFs with different standard deviation (σ)

  $G(x) = \frac{1}{\sqrt{2\pi}} e^{-\frac{(x-\mu)^2}{2\sigma^2}}$

- PDF with a skewness (α) different from zero

  $Gs(x) = \frac{2}{\omega\sqrt{2\pi}} e^{-\frac{(x-\xi)^2}{2\omega^2}} \int_{-\inf}^{\alpha} \frac{1}{\sqrt{2\pi}} e^{-\frac{t^2}{2}} dt$

- Bimodal constructed by two Gaussian PDFs

$$B(x) = G_1 + G_2$$

We generated random data extracted from 4 typical shapes for reference PDFs and 4 shapes of instantaneous PDFs. The reference PDFs in our actual ensemble analysis are built at each gridpoint from $N = 50\,members \times 365\,days \times 20\,years = 365000\,samples$; instantaneous PDFs may be computed every day from $Ni = 50$ samples, or over longer intervals ($Ni =$ multiples of 50).

From each of the different cases, we thus generated 365000 values picked randomly from each of the 4 reference PDFs, and Ni values picked randomly from each of the 4 instantaneous PDFs. The sample size took the following 8 values: $Ni = 20$, 50, 100, 250, 500, 50×30, 50×365 and $50 \times 365 \times 20$. We consider that the "true" instantaneous entropy (S_{true}) is that obtained for $Ni = N$, and we estimated the computational error from a Monte Carlo experiment, by calculating 100 estimates of instantaneous entropies (S_{inst}) with the 7 smaller $Ni's$. For each case and the 7 subsampling choices, this procedure thus provided us with 100 entropy error estimates ($dS = (S_{inst} - S_{true})$), from which we computed the random estimation bias $\sigma(dS)$ and the mean estimation bias ($< dS >$).

An example of the results is shown in figure 2.10 in the case when reference and instantaneous PDFs are both skewed. Panel 'a' shows the random estimation bias, which decreases almost exponentially as Ni increases. The random estimation bias is smaller when the entropy is greater (different colored lines): there is greater precision in the computation of large entropy values. In the different experiments performed, on average, the random estimation bias computed from 50 daily samples lies in the range $[0.015, 0.025]$ for low values of entropy ($S < 0.5$), and for high entropy values ($S > 0.8$) in the range $[0.006, 0.02]$. Although the error is small in general, at low entropy values($S < 0.25$) this error becomes more important (20%).

The opposite occurs for the mean estimation bias ($< S_{inst} >_{100} - S_{true}$): this bias is more significant when the values of entropy are high, and there is greater accuracy in the value calculated when the entropy is low. In average over the experiments performed, the mean estimation bias is 5% of any entropy value (low or high). Just like the random estimation bias, accuracy improves with more data available. In conclusion, we can say that 50 independent samples (50 members every day) are sufficient for a good estimation of the entropy and its possible temporal changes, taking into account the calculated error for future analysis and interpretations.

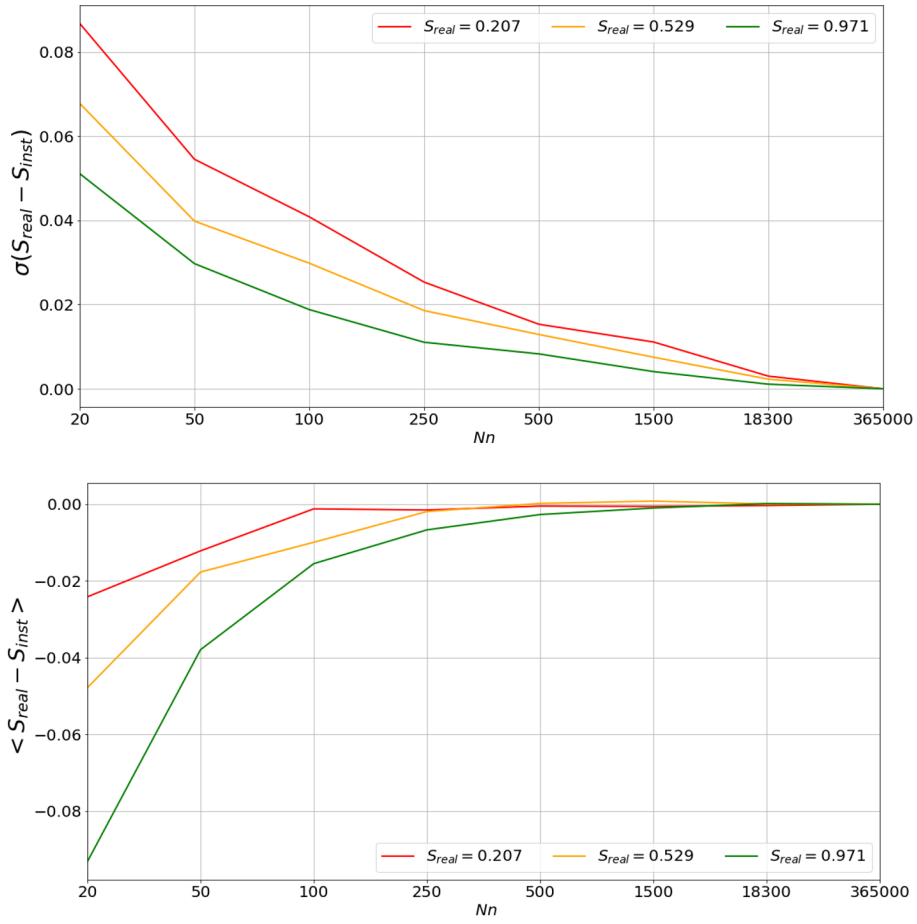

FIGURE 2.10: Accuracy and precision of entropy values in a Gaussian distribution with a skewness different from zero. a) Standard deviation of the difference between the real value and the values of entropy in the 100 experiments. b) Mean difference between the real entropy value and the value calculated with PDFs with different number of data. The legend in the graphics is the value of the "true" entropy from three different instantaneous PDFs.

Chapter 3

Model Assessment

This thesis is focused on studying the respective contributions of the oceanic and atmospheric drivers of the variability in the subtropical North Atlantic Ocean, so it is important to evaluate the ability of the model to simulate the observed variability. We now compare the simulation results with observations from different sources.

3.1 AVISO-CMEMS and model SLA comparisons

We first assess the temporal variability of SLA of the ensemble simulation by comparison with the AVISO observations. The following figures (Figs: 3.1,3.2) show the maps of total SLA variability at different time scales. The first row represents the temporal standard deviation of SLA from AVISO observations (σ_{AVISO}). The second row represents the ensemble mean of the temporal standard deviation of all individual members ($\langle\sigma_{GSL}\rangle$), and the third row shows the difference between these modeled and observed std.

We observe in figure 3.1 (left column) that the general spatial pattern of SLA variability is correctly simulated, with maximum variability in the region of the Loop Current and the Gulf Stream, and large variability in the Gulf of Mexico, the Colombian basin and the main path of the North Brazil Current (NBC) eddies. In the Caribbean Sea and the open ocean (mid-Atlantic), the model variability is weaker than in other regions, and is underestimated compared to the observations.

In the northern Florida Current and the beginning of the Gulf Stream, the variability is overestimated due to the presence of eddies that do not propagate there in the real ocean. The analysis of the entire region of simulation (North Atlantic 21°S−81°N), confirms the presence of large eddies south of their observed locations in the Gulf Stream region. We know that representing an adequate Gulf Stream is still challenging, even models with higher resolution than $1/4°$ have significant problems representing the GS

(e.g. Barnier et al., 2006; Chassignet and Xu, 2017). Despite this notable difference between the modeled and observed GS, we do not expect it to represent a problem for the processes studied in this thesis, as no significant upstream contribution from the GS into the Gulf of Mexico is expected.

In the Gulf of Mexico, in particular in the LC area and the LCE's pathway, the model underestimates the variability in the north and overestimates it in the south. This dipole indicates a southern shift of the extended LC in the model compared to the observations, thus a southward shift of the LC eddies pathway as we will show in section 3.2.

The High-Frequency SLA variability (fig.3.1, right column) has a similar spatial pattern as the full variability. We observe good agreement in the spatial variability, especially in the regions with high variance like the LC, GS, and the GoM. Similar to the full variability, we observe in the Gulf of Mexico a dipole of underestimation and overestimation of the variability due to the southwestern shift of the LC extension. In the Caribbean Sea, and the open ocean (mid-Atlantic), the model underestimates the variability compared to the observations. Unlike the full variability of SLA, the modeled HF variability is slightly overestimated in the coastal zone of the northern Gulf of Mexico and the US coast. It is also possible that the observed HF variability in the coast is underestimated due to optimal interpolation process of the along-track altimeter data.

We observe in figure 3.2 (left column) that the SLA variability of the mean seasonal cycle is underestimated in most of the region (panel C). The maximum of simulated seasonal variability in the LC region is in good agreement with the observations. However, the simulations overestimate the area around of the LC that has high variability; therefore, the mean seasonal variability in the central-north GoM is slightly overestimated. Other regions with slight overestimation of the SLA variability, are the Panama-Colombia gyre and the NBC eddies pathway.

Figure 3.2 (right column) shows the comparison of the observed and simulated SLA variability at Low-Frequency. We can observe that the simulated LF variability is quite similar to the observations. In general, the model only slightly differs from the observed magnitude of the LF SLA variability throughout the basin. We observe two main regions with more substantial differences: an overestimation of the modeled variability in the Gulf Stream, and an underestimation in the Loop Current region. This good agreement in the low-frequency variability is similar to what Penduff et al. (2010) mentioned: at $1/4^{\circ}$ resolution, NEMO is generally able to simulate realistic LF variability levels despite the lack of mesoscale activity.

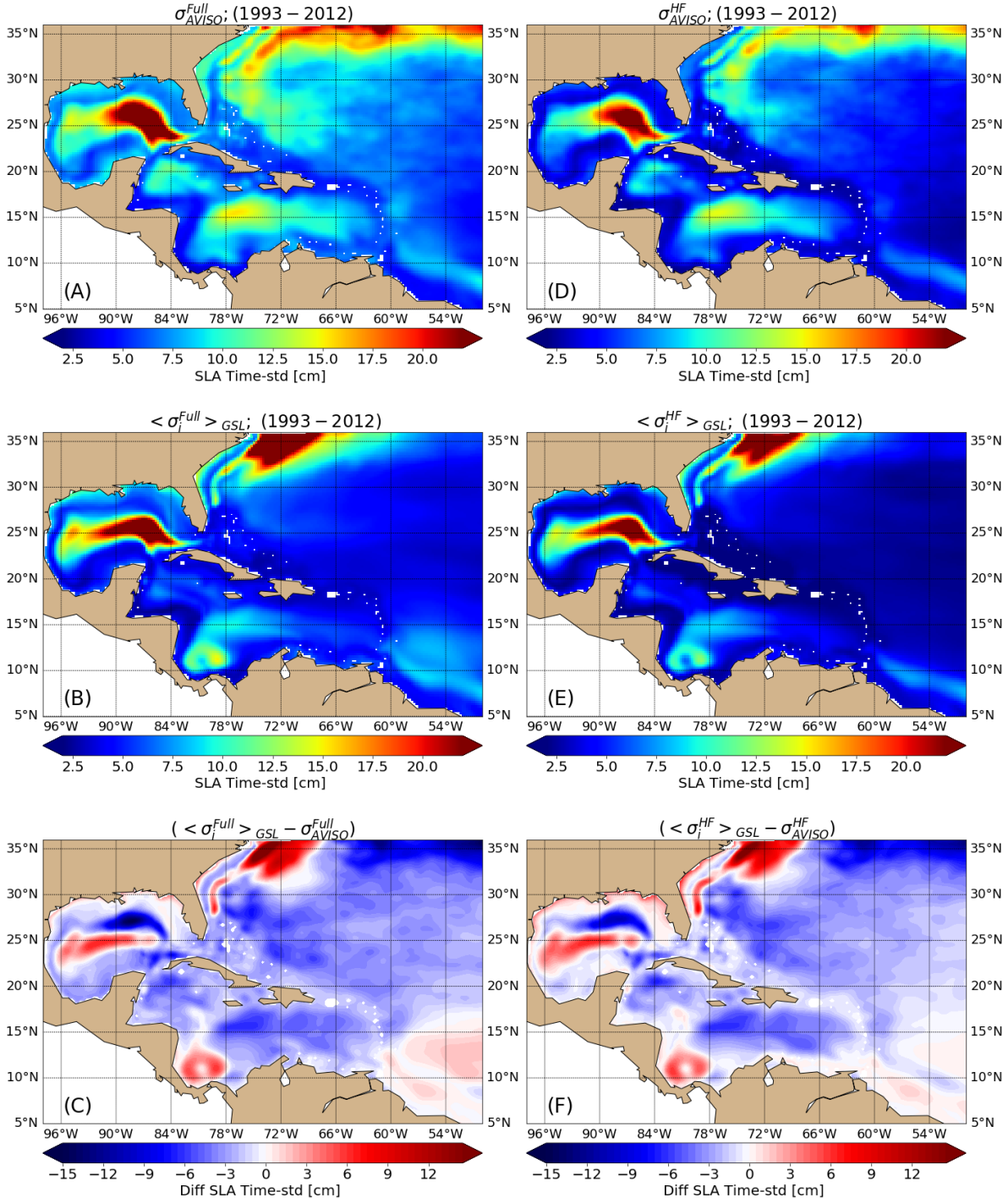

FIGURE 3.1: Map of SLA temporal standard deviation (σ_i) for: AVISO (σ_{AVISO}) in the first row; Ensemble-mean GSL ($\langle\sigma_{GSL}\rangle$) in the second row; and difference of stds: GSL-AVISO ($\langle\sigma_{GSL}\rangle - \sigma_{AVISO}$) in the third row. For the full variability (left column) and high-Frequency variability (right column).

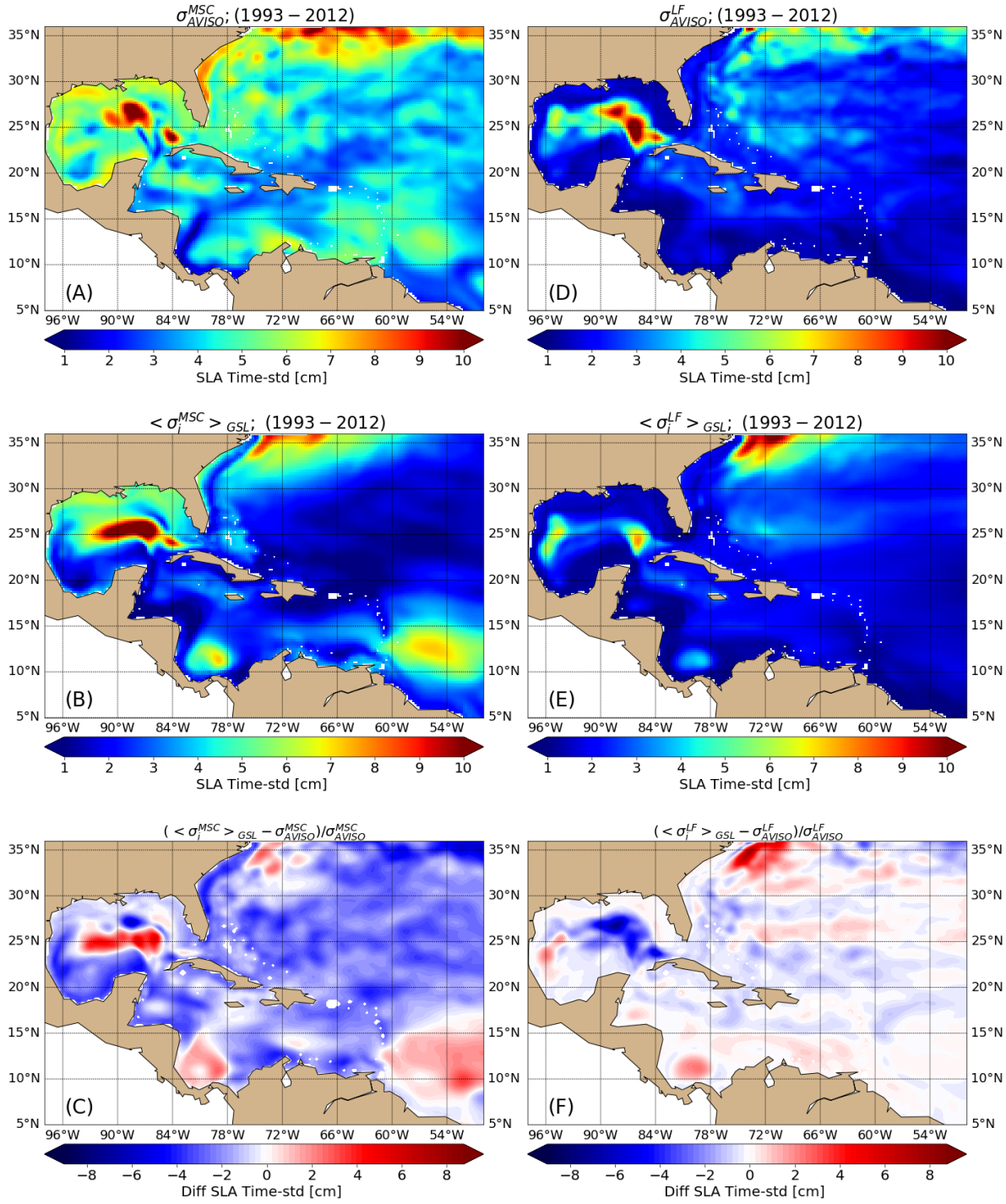

FIGURE 3.2: Map of SLA temporal standard deviation (σ_i) for: AVISO (σ_{AVISO}) in the first row; Ensemble-mean GSL ($\langle\sigma_{GSL}\rangle$) in the second row; and difference of stds: GSL-AVISO ($\langle\sigma_{GSL}\rangle - \sigma_{AVISO}$) in the third row. For the Mean Seasonal Cycle (left column) and Low-Frequency (right column) variability.

To summarize, we observe a correct agreement between the observations and the simulations. The spatial patterns of SLA variability are well represented in the simulations at different frequencies. There is an underestimation of the modeled variability in most of the region, mainly at high-frequency. We also observe a slight overestimation of the simulated SLA variability in the regions with the greatest variability, i.e., Gulf stream, Loop Current, and the Panama-Colombia gyre. The simulated SLA variability generally agrees in space and amplitude with the observed variability of the main features of the Gulf of Mexico, like the Loop Current and associated mesoscale eddies. We can say that our model appropriately represents the region's main features on the surface and its corresponding variability.

3.2 Loop Current kinematic metrics

We mentioned in chapter 1 that the Loop Current variability and its actual drivers are not well known. Our present objective is to study the characteristics of the simulated Loop Current from a large collection of simulated evolutions, and compare it with the real ocean (observations) in a robust way.

We estimate several Loop Current kinematic characteristics from the AVISO observations and the simulations. Using LC length time series from every member, we compute the northernmost latitude and the westernmost longitude of the LC at every time step, the date of eddy shedding events, and the period (T) between eddy shedding events (this specific methodology is presented in section 2.4.1). As in other studies, we analyze the northernmost latitude that the LC reaches before and after an eddy separation. To evaluate if the model represents the LC kinematics adequately, we compare the maximum and retreat latitudes (defined in 2.4.1) with the observed ones.

Lugo-Fernández et al. (2016) and Hall and Leben (2016) used the CCAR (Colorado Center for Astrodynamics Research) altimeter data reanalysis product (more details of the product in Leben (2005)) to define some kinematic LC characteristics and we compare our simulated results with theirs. The retreat latitude in the model appears to lie south of the observations: the observed average LC retreat latitude is 25.9°N±0.8°; while the average retreat latitude of the simulations is 23.9°N±0.5°. The maximum latitude of the LC also appears to lie slightly south of the observations. The average maximum latitude observed is 27.5°N±0.4°, and the average maximum latitude of the simulated LC is 27.1°N±0.15°. The average maximum latitude of the LC in the model

is similar to what (Lugo-Fernández et al., 2016) observed; nevertheless, the maximum latitude of the LC in all members never exceeds 27.4°N, while in the real ocean it can exceed 28°N, and interact with the northern GoM shelf. We also observed that there is a large dispersion in the retreat latitude of the simulated LC, while the maximum latitude is more similar in all members and events. As a consequence, most of the LCEs separate in a similar location leading to an underestimated dispersion in the LCE's pathway to the west. In general, we observe that the location and the core of the two main states (extended and retracted) are adequately represented, although the model favors a rather similar region for the LCE shedding.

We use the tables reported by Lugo-Fernández et al. (2016) to characterize the observed eddy shedding events and their characteristics (separation period, separation date, maximum and retreat latitudes). Lugo-Fernández et al. (2016) reported 30 eddy separation events observed from AVISO over the period 1993-2012 and we use the information of the observed 28 events whose separation periods are longer than 50 days. In our simulations, using the same criteria, we observe between 22 to 24 eddy shedding events per member, with a total of 1125 events for the whole ensemble. The number of eddy shedding events does not vary much between members (between 22-24). A possible interpretation is that the instability processes responsible for the eddy shedding events reproduce themselves with little difference from an event to another, and from member to member. This suggests that these dominant processes are well simulated, but that other dynamical processes that influence or modulate the shedding process (e.g., LC frontal eddies) are not well represented.

The period between LC eddy separation events is one of the most studied LC features. Figure 3.3 shows the separation time histograms for the observations (blue), the 50 members (gray), and the ensemble statistics of the 50 histograms (min, max, 25%, 50%, and 75%). We observe that there is a significant dispersion between members regarding the period between eddy separation events, some members having more similar distributions to the observed one, than others. In the simulation we observe a preference of the separation period of $\sim$ 325 days, while the observations have a preference for $\sim$ 175 days. Nevertheless, most of the observed separation periods are simulated, except for large periods (i.e. $>$ 450days). Comparing our results with other numerical results, can be complicated given the large differences in experiment configurations, especially the differences in spatial resolution and simulation duration. However, numerical experiments report a wide range of average periods observed: 5.5 months (Lin et al., 2009), $7-8$ months(e.g., Chang and Oey, 2013), $\sim$ 9 months (e.g., Dukhovskoy

et al., 2015), or experiments with large variability on the eddy shedding period $\sim 3-15$ months (e.g., Le Hénaff et al., 2012).

Figure 3.4, shows the histogram of eddy separation events by month for the observations and the model. As in the separation period histogram, we observe a significant dispersion between members, but in general, the eddy separation events observed each month are simulated. The distributions of the simulated eddy separation events per month can differ significantly between them, but certain members have similar distributions to the ones obtained with observations. An important point to highlight is that the number of shedding events, per member over this 20- year period, is actually small ($22-24$ events), so the statistics may not be robust. The observations have 28 events in a 20 years period, which means that the observed statistics may not be robust either, and can differ from one source to another. Figure 3.5 shows the histogram of the eddy separation by month of the simulations and the observations from the Woods Hole Group Eddy watching program (https://www.horizonmarine.com/). Their observations include 33 events from 1993 to 2012, and we can observe that the histogram of observations is different from the one Lugo-Fernández et al. (2016) reported, which further suggests that the statistics are not very robust with the available data and also a lack of consensus of eddy separation event definition.

Lugo-Fernández and Leben (2010) suggested that the latitude of retreat influences the time of shedding of the next event: if the latitude of retraction is small, the subsequent eddy separation will take more time. This suggests that an eddy shedding event may not be independent of the one that preceded. Therefore, treating eddy shedding events separately may not be adequate.
In figure 3.6, we can observe that this is mostly true in our simulations. The relationship between the period and latitude of retraction in our simulations has a correlation coefficient of -0.62, but this relationship lies in a range between $0.1-0.9$ when computed in each member individually. For the observations reported in Lugo-Fernández et al. (2016), we found a correlation coefficient of -0.82. The correlation coefficient obtained in the simulations and observations suggest that there is a hint of a linear relationship between these two characteristics of the LC that may be a source of predictability for eddy shedding events.

The large inter-member dispersion mentioned above suggests again that 20 year time series are too short to get robust statistics from individual members (and from observations), and/or that such statistics are very sensitive to the actual succession of

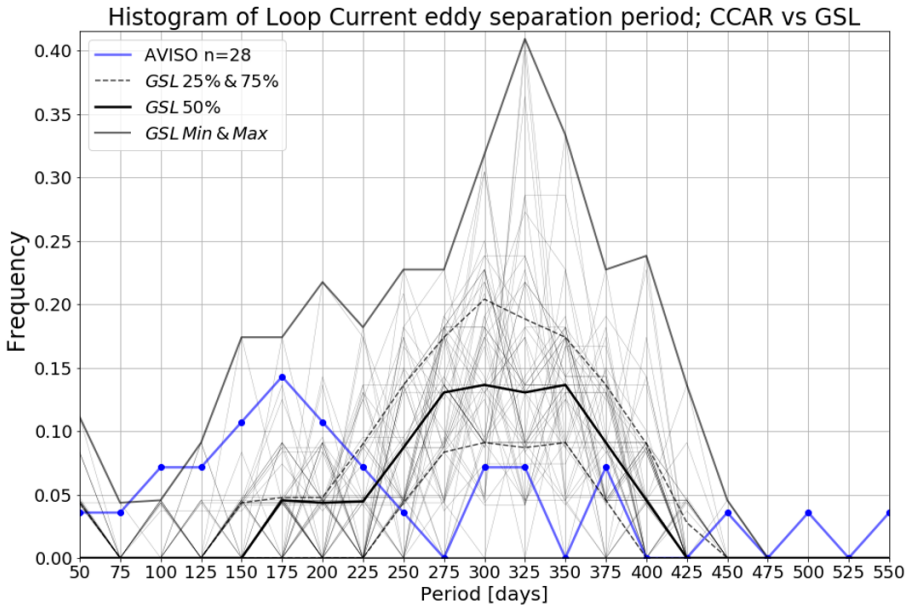

FIGURE 3.3: Histograms of the period between eddy separation events from: Observations (blue), 50-members (thin gray), the minimum and maximum values in the 50 members histograms (solid gray), the median (black), and the 25% and 75% (dashed gray) values of the ensemble histograms.

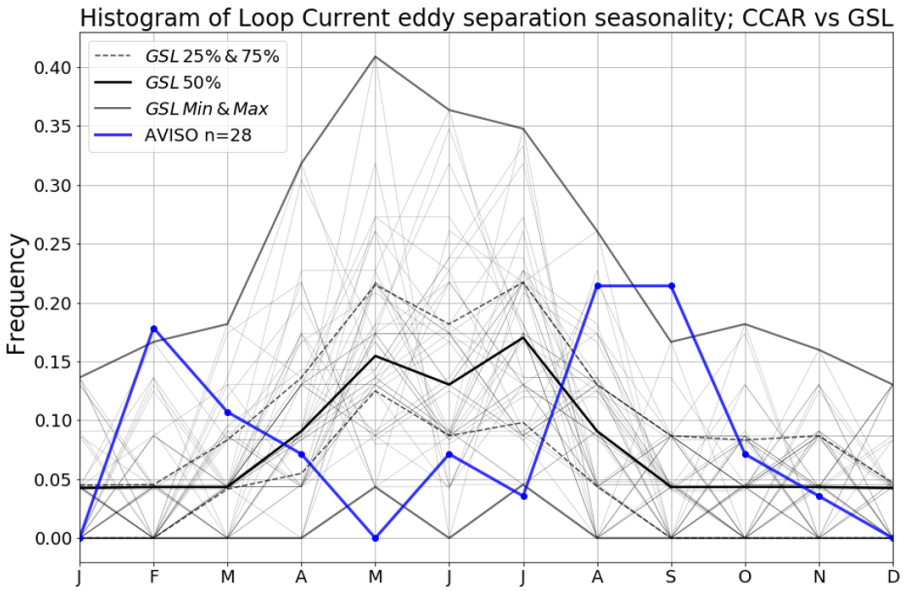

FIGURE 3.4: Histograms of the eddy separation events by month from: Observations (blue), 50-members (thin gray), the minimum and maximum values in the 50 members histograms (solid gray), the median (black), and the 25% and 75% (dashed gray) values of the ensemble histograms.

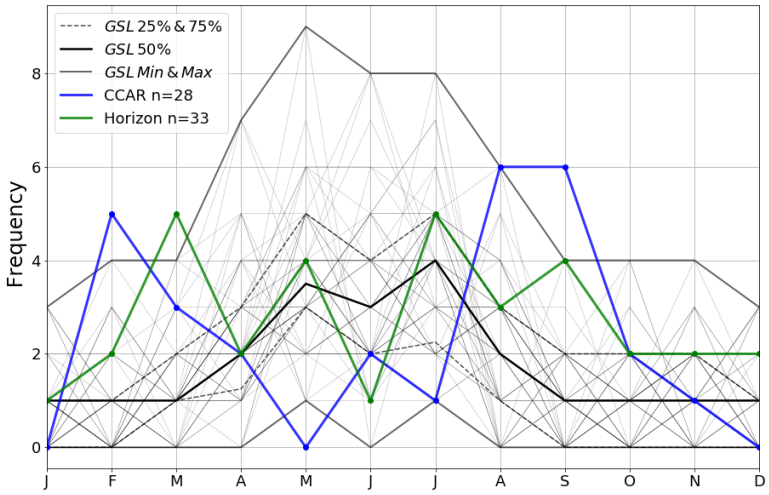

FIGURE 3.5: Histograms of the eddy separation by month from: Observations (Lugo-Fernández et al., 2016) (blue), the Woods Hole group Observations (green)(1993-2012), 50-members (thin gray), the minimum and maximum values in the 50 members histograms (solid gray), the median (black), and the 25% and 75% (dashed gray) values of the ensemble histograms.

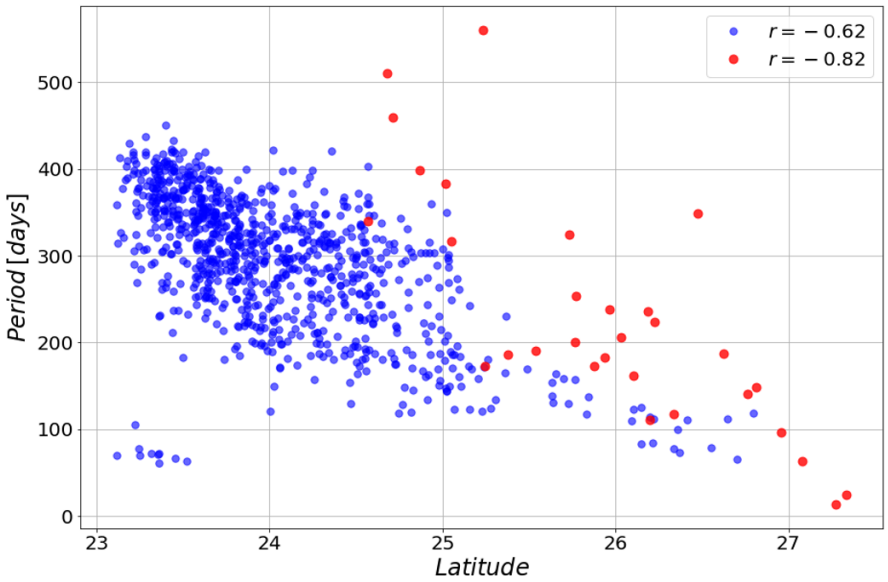

FIGURE 3.6: Eddy separation period against LC retreat latitude for simulations (blue) and observations (red). Respective correlation given on the top right.

events in this chaotic system. This may also be the case for observations: it is plausible that slight differences in the real ocean's past may have led to the substantial differences in the observational statistics over the last two decades. These observational statistics

may thus not characterize the Loop Current dynamical system itself, but the specific time series that this chaotic system actually produced over this relatively short period. Observational statistics are thus probably not robust enough to describe the dynamics of the Loop Current system from the short altimeter time series available today.

The propagation of the LCEs to the west, their pathway, velocity of translation, and interaction with other eddies, are other important characteristics of the LC and the GoM. Vukovich (2007) found that the LCEs tend to propagate to the western GoM, between 24°N and 26°N, where they found 64% of the observed eddies; the northern and southern pathways are less preferred with 24% and 14% respectively. In our simulations, we observed (just by quick visual supervision) that the preferred pathway of the LCEs is also the central one, with a few eddies expending some time north of 26°N or south of 24°N, but favoring the central pathway. The lack of eddies propagating in the northern pathway is likely due to a simulated LC that does not extend enough to the north as the observed LC does.

3.3 Boundaries of the Gulf of Mexico

We now evaluate the model realism regarding the water exchanges at both boundaries of the Gulf of Mexico, and between Florida and Bahamas. Let us first consider the ensemble and time mean sections along these three channels (Yucatan, Florida-Cuba and Florida-Bahamas), shown in figure 2.6. Table 3.1 have the values of maximum velocity and range of temperature observed and simulated for each section.

The magnitude and general structure of the velocity field is well represented in the Yucatan Channel, compared to the observations (Sheinbaum et al., 2002) and other simulations (Ezer et al., 2003; Oey et al., 2005; Rousset and Beal, 2011; Nedbor-Gross et al., 2014). The velocity is mainly into the Gulf of Mexico (GoM), with the maximum ($\sim 1.6\, ms^{-1}$) in the surface near the Yucatan shelf. In the deep part ($800\, m$) the current is mainly out of the GOM and concentrated in the eastern deep part of the channel. The observed Cuba Counter-current in the shallow part described in Sheinbaum et al. (2002) and Candela et al. (2019) is not well represented in our simulations and has no signature in the ensemble mean. However the current in this region has a large variability, which indicates that this counter current may be present at some moments. The mean maximum and minimum temperature are slightly colder than observations, nevertheless, the structure of the mean temperature is adequately represented and is similar to the

observations (Sheinbaum et al., 2002), with a strong thermocline in the western part.

The Florida-Cuba time and ensemble mean velocity section, has the strongest velocity to the east ($\sim 1.5\, ms^{-1}$), in the northern part near Florida in the first $200\, m$. The velocity decreases to the south and becomes almost zero at the surface and mainly to the west in the deep part ($> 250\, m$).The results are similar to the observations by Rousset and Beal, 2014 with a maximum of $1.5\, ms^{-1}$ near the Florida bank, nevertheless this particular section is not reported in many studies; usually descriptions are shifted to the east (Rousset and Beal, 2014, e.g.) or to the west (Candela et al., 2019). For this reason, it is difficult to compare with observations in detail.

The temporal and ensemble mean section in the Florida-Cuba Strait (see Fig. 3.7) shows that the temperature gradients are maximum in the northern part, near Florida. In accordance with geostrophy, the maximum eastward velocity is in the same region. Nevertheless, the mean velocity in the southern and deep part, which is to the west, disagrees with the temperature gradients and so, with geostrophy. In the model results, we observed that a little to the east of this section we chose ($\sim$ 25 km or one model grid point), a bank modifies the local circulation. The Cay Sol bank rises at 50 m depth, significantly changing the water column's depth in only a few kilometers. This significant topographic obstacle and associated bottom boundary layer are likely to promote ageostrophic flows around it.

In figure 3.8d, we can observe an example (one member) of the mean zonal velocity at $\sim$ 450 m depth in the region. We observe at this depth that the velocity in the Florida-Cuba channel is mainly to the east, while near the Cay Sol bank at the south part of it, the velocity is mainly to the west (pointed by the black arrow). This pattern is observed at different depths (figure 3.8 a,b,d) down to the depth of the channel ($\sim$ 600 m). This westward flow, which is not in geostrophic balance, may be due to a current coming from the east between the Bahamas bank and Cuba, mentioned in other studies (Hamilton et al., 2005; Candela et al., 2019). The current between the Bahamas bank and Cuba is represented in our simulations (as we can observe in panel a); nevertheless, the temporal and ensemble-mean vertical sections (Fig. 3.7) show that the model may overestimate the westward flow in the Cay Sol bank region.

The ensemble and time mean velocity of the Florida-Bahamas section is similar in magnitude and structure to the observations (Rousset and Beal, 2011; Rousset and Beal, 2010; Meinen and Luther, 2016) and simulations (Rousset and Beal, 2011). The maximum velocity is located at the surface near Florida, with a magnitude of $\sim 1.7\, ms^{-1}$ for

observations (Rousset and Beal, 2011; Rousset and Beal, 2010), and 1.5 ms^{-1} in the simulations, both to the north. The ensemble and time mean section of temperature looks similar to the temperature sections observed by cruises and reported by Meinen and Luther, 2016, with the maximum temperature in the east and a strong vertical gradient in the west.

In all three sections, the mean bottom and surface temperatures are colder than those observed in other studies. However, gradients and structure are well represented, so we do not expect adverse impacts in the geostrophic circulation.

TABLE 3.1: Characteristics of the circulation across the sections from observations and our ensemble simulation.

	Yucatan Ch		**Florida-Cuba**		**Florida-Bah**	
	max $\overline{V}^t$ (cm/s)	**range** $\overline{T}^t$ (C°)	**max** $\overline{V}^t$ (cm/s)	**range** $\overline{T}^t$ (C°)	**max** $\overline{V}^t$ (cm/s)	**range** $\overline{T}^t$ (C°)
Candela et al., 2019 (4y, filt 7d)	120		110			
Athié et al., 2015 (5y, filt 48h)	120					
Rousset and Beal, 2010; Rousset and Beal, 2011; Rousset and Beal, 2014 (5y, composites)			150		170	6.5-30
Candela et al., 2003 (2y, hourly)	110	5.5-30				
This Study (20y, 5d mean)	**170**	**3.9-27.8**	**150**	**6.3- 27.5**	**150**	**7.2-27.0**

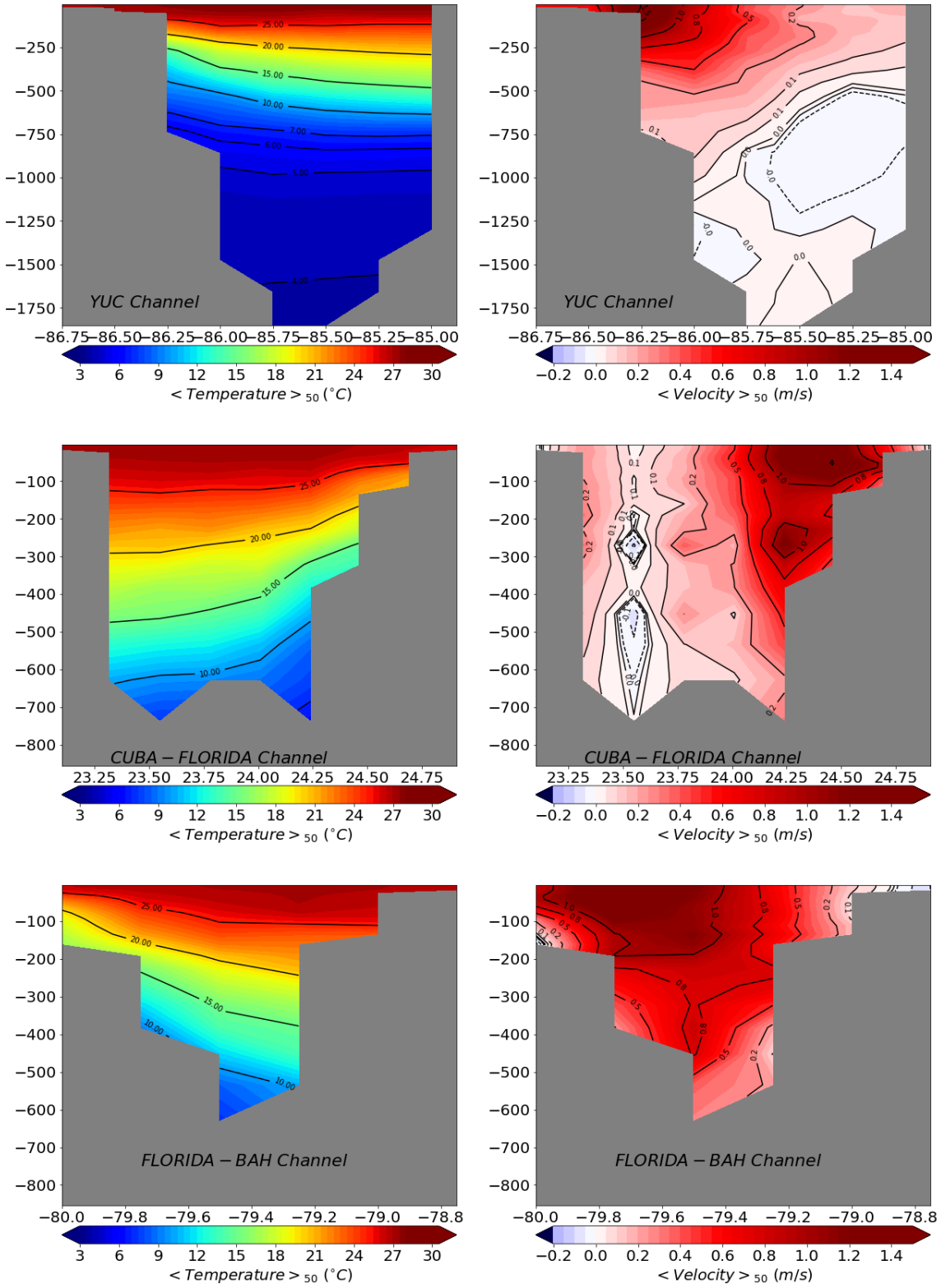

FIGURE 3.7: Ensemble and time mean sections of temperature (left column) and velocity (right column). Positive (negative) values in velocity indicate currents to the north (south) for the Yucatan and Florida-Bahamas sections, and to the east (west) in the Florida-Cuba section.

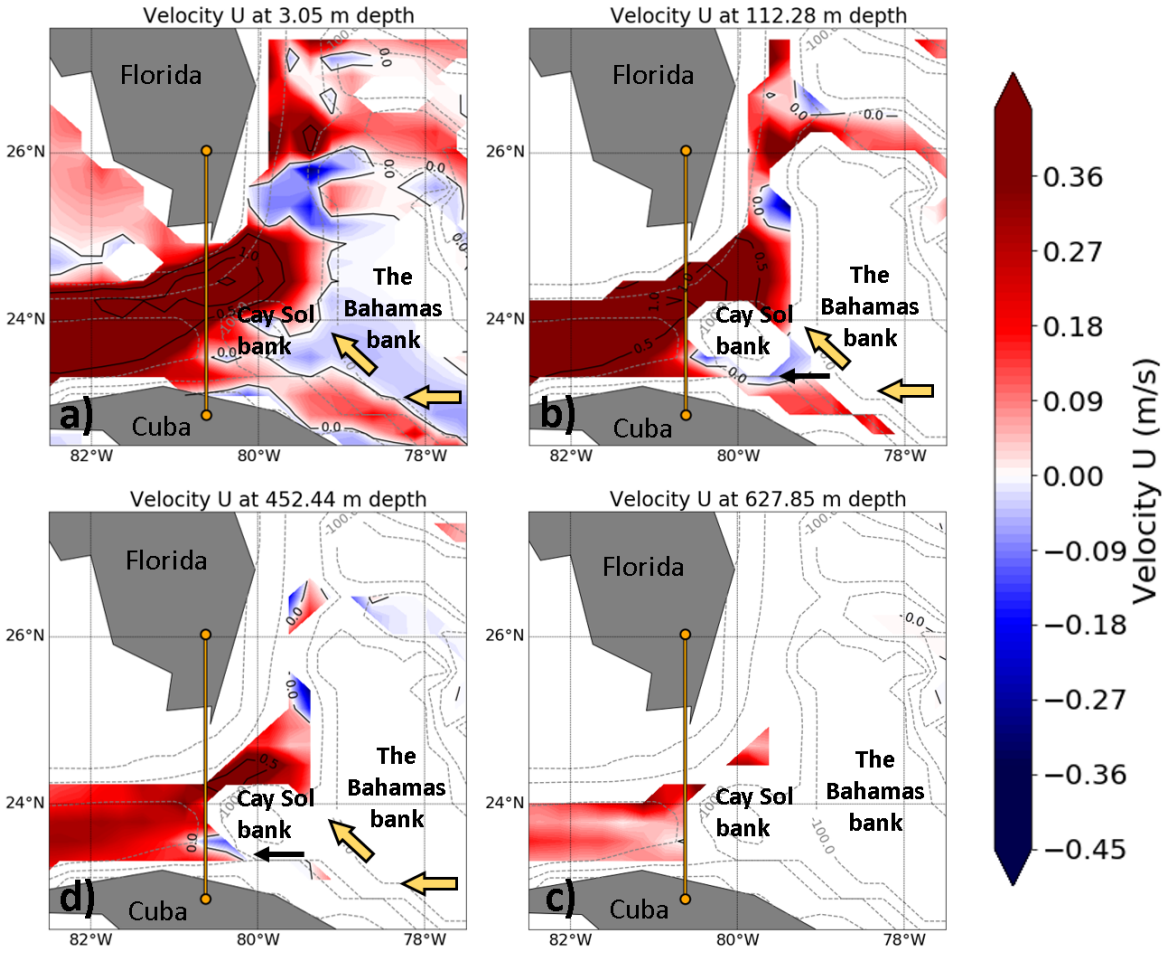

FIGURE 3.8: 20-years temporal mean zonal velocity of member 001 at different depths around the Florida Straits. The yellow section corresponds to the section in figure 3.7 Cuba-Florida. The yellow arrows in panels **a,b,** and **d**, point the westward and then northward flow observed by Hamilton et al., 2005. The black arrow in panel **b and d** points the westward current we may overestimate in the model.

Volume water transports

The water volume transport across the sections are now compared to observations. As mentioned in section 2.4.2, we split the Yucatan Channel in upper and deep layers, but to compare with observations, we compute only the barotropic volume water transport across the three sections (for observations and each member). First, we compare these transports with those reported in other observational studies. In the next section, we compare the volume transport across the Florida-Bahamas section with *in situ* observations.

Table 3.2 summarizes the mean transports reported in different studies and the temporal and ensemble mean transports computed from our simulations. The period over which the mean transport was calculated (along with other quantities) are in the first column. When studies report the amplitude of the annual cycle it is indicated in the Table.

TABLE 3.2: Mean and variance (and range) of the observed transports through the sections from observations and the ensemble simulation. All values are in Sverdrups (Sv).

	Yucatan Ch	**Florida-Cuba**	**Florida-Bahamas**
Candela et al., 2019 (4y,*hourly)	27.6±11.4*	27.6±5.7*	-
Annual cycle	3.14±0.73	3.09±0.62	-
Athié et al., 2015 (5y,filt 48h)	27.0±3.6 (SE:0.5)	-	-
Rousset and Beal, 2010; Rousset and Beal, 2011; Rousset and Beal, 2014 (5y,composites)	30.3±8.8 (SE:1.1)	29.3±6 (SE:2.7)	30.8±3.2 (SE:0.3)
Annual cycle	2.7	-	2.9
Hamilton et al., 2005 (11m,*infered)		∼ 25.2* ±5.16	31.1± 3.49
Candela et al., 2003 (2y, hourly)	23.06 ±3.1		
This study: (20y, 5d mean)	**33.44± 2.22**	**33.46± 2.24**	**30.77±2.07**
Annual cycle	**3.73±0.96**	**3.81± 0.98**	**3.20± 0.81**

We observe in general a slight overestimation of the mean transport in all sections, but in the range of the variance observed by other studies. We observe that the transport has larger variance in the observations than in the simulations, probably since the observations include a very high frequency (hourly) which induces a more significant

variability of the transport. The amplitude of the annual cycle is similar in the observations and simulations.

3.4 Florida- Bahamas transport

We now compare the volume transport at the Florida-Bahamas section in the cable-based observations and in the 50 OCCIPUT members, over the period 2002-2012. Figure 3.9 shows the individual member transports anomalies (gray), the ensemble-mean (black), and the observed transport anomaly (blue). We observe that in general the phase of the transport variability in the observations resembles their forced counterpart (ensemble mean) in the model. We observe some extreme events (e.g., 07/2009) that are underestimated by the model; nevertheless, in general, the phase is adequate, and some members are capable of representing such extreme events.

We compute a Taylor diagram (Fig.3.10) to analyze the correlation between the observed and simulated transport time series and compare their standard deviations. Depending on the member, the range of correlations lies between $0.3 - 0.5$ (95% significance level) and the standard deviations are in the range of $0.6 - 0.8$ compared to the observed standard deviation. As intrinsic variability behaves as a random "noise" in each member's time series, the correlations can be relatively low, although the standard deviations are in correct agreement with the observations. The red triangle represents the correlation and standard deviation of the ensemble mean (forced) transport compared to the observations. We observe that it has a larger correlation (0.6) than the individual members, but less relative standard deviation (0.5). This is an expected and previously mentioned outcome in other studies e.g., Leroux et al., 2018. The ensemble mean represents the forced variability of the transport; i.e., is what all members have in common. As the intrinsic "noise" has been averaged out, the correlation coefficient is larger, and the standard deviation is smaller compared to their counterparts in individual members.

Conclusions

To summarize this section, our assessment has shown that the ensemble simulation has a good skill in representing many observed oceanic features like: The Loop Current two main states and the eddy shedding events, the abundance and strength of mesoscale eddies in some regions (Caribbean Sea, Gulf of Mexico, Gulf Stream), and the water volume transports in the boundaries of the Gulf of Mexico.

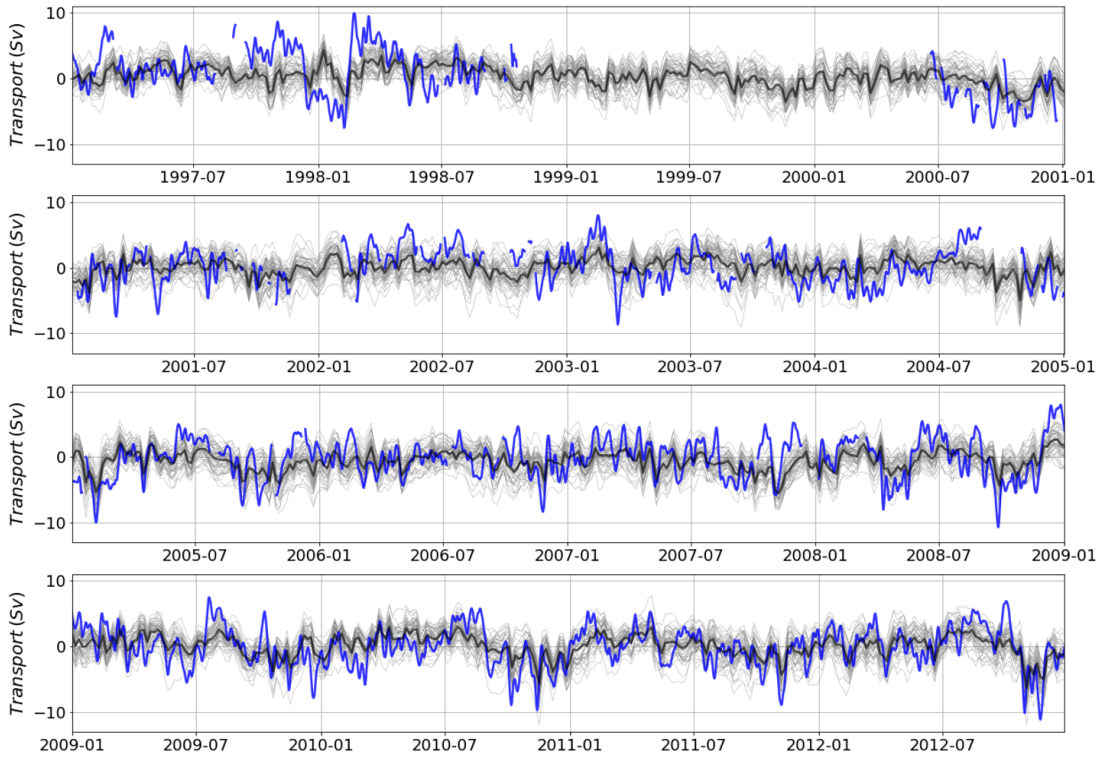

FIGURE 3.9: Transport anomaly of the Florida-Bahamas submarine cable (blue) and the transport anomalies of each ensemble member (gray) and ensemble mean(black).

Some specific observed features are however less realistic in the model in particular: the magnitude of the Gulf Stream variability, the extension of the Loop Current, the variability in the Loop Current Eddies pathway, the magnitude of the variability in the Caribbean Sea, and the extreme events observed in the water volume transports. These limitations may partly be due to missing physics in the model,whose resolution remains modest. Also extreme events have been always difficult to predict at the right time with the right magnitude, since they are highly chaotic features.

Our results also show that various observational time series, like the AVISO altimeter dataset, are still too short to yield robust statistics, on eddy shedding events in particular. Most of these observational statistics actually lie in the range of modeled signals so that they are not inconsistent with the model, which can therefore be considered as quite realistic for the processes we are interested in.

This chapter also illustrates how assessing a model in the ensemble rather than in a

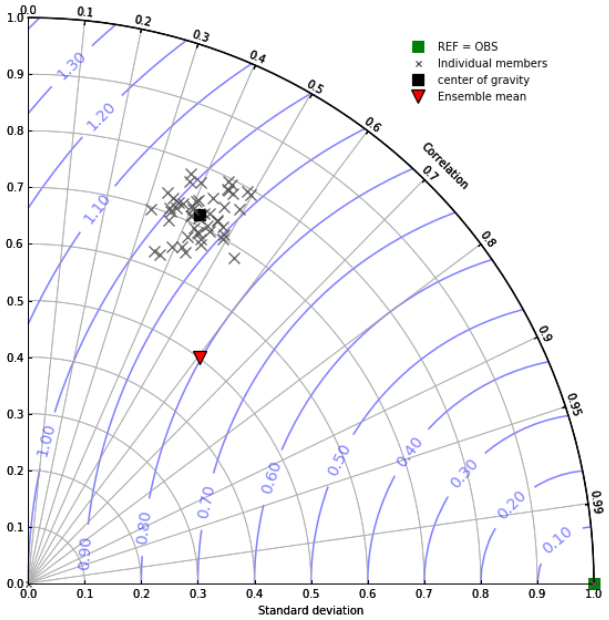

FIGURE 3.10: Taylor diagram, using the Florida submarine cable transport as reference for the period 2002-2012. Observations are averaged every 5-days. The standard deviations are normalized by the standard deviation of the observations. Blue contours represent the RMSE.

single run framework is more complicated, but also has specific benefits. The complexity comes from the fact that observational time series represent only one (the actual) realization of the oceanic variability that was picked by nature out of the range of possible evolutions, while the model ensemble was designed to give access to this range of possibilities. Specific statistics and metrics like Taylor diagrams are helpful to condense all the information in this ensemble context and provide a synthetic and robust view of the model skill. Comparing a model ensemble with observations also provides unique information about other important questions, such as the inherent randomness of certain variables (see next chapter), or the robustness of available observations considering the simulated spread. Such comparisons also highlight the limits of assessing a single turbulent model run with regard to observations, given e.g., the wide range of correlation coefficients among members: a given model can thus follow more or less realistic trajectories in phase space depending on slight uncertainties in its initial state and ensembles are certainly valuable (albeit expensive) approaches to provide robust assessments of models themselves.

In the following, we take advantage of the ensemble dimension (and the associated large number of simulated signals) to assess the respective roles of the atmospheric variability and of the ocean's intrinsic variability in driving the oceanic variability in the region.

Chapter 4

Forced and Intrinsic SLA variability

In this chapter, we aim to disentangle the intrinsic part of the ocean surface variability from the influence of the atmospheric forcing in the Subtropical North Atlantic. We first make the classical assumption that the intrinsic and forced variabilities are indeed separable; we use usual methods based on simple ensemble statistics that are considered acceptable in cases when ensemble PDFs remain close to Gaussian most of the time over most regions. Then, we propose a more rigorous method to disentangle the oceanic and atmospheric drivers in the ocean variability; this method is more rigorous mathematically, is valid in both Gaussian and non-Gaussian cases, and aims to estimate the SLA variability intrinsic fraction and its temporal modulation by the atmospheric forcing.

4.1 Gaussian metrics

Figure 4.1 shows the model SLA variability in the subtropical North Atlantic, decomposed in frequency and origin (intrinsic or forced) using the methodoly described in section 2.5.1. As we discussed before (section 3.1) the SLA variability and the main features in the region are adequately represented by the simulations

First we analyze the SLA variability of the detrended time series (named "All time scales" in this section). The regions with the largest total SLA variability ($\sigma_T^{All} > 25$ cm) are the Gulf Stream and the Loop Current, and it is mainly due to the High Frequency variability as we can observe by comparing panels A and D. Secondary maxima of variability ($\sigma_T^{All} > 13$ cm) are observed in the the Colombian-Panama gyre, and the central GoM. A substantial variability ($\sigma_T^{All} > 10$ cm) is simulated in the Caribbean Sea and the pathway of the North Brazil Current (NBC) eddies.

Panels E and I show the partition of the variability according to its origin (E: Forced; I: Intrinsic), using the previous definitions with a Gaussian assumption. Panel M shows

the variability ratio $\sigma_I^{All}/\sigma_F^{All}$. We observe regions with relatively large forced variability ($\sigma_F^{All} > 8$ cm), like the central GoM, the Gulf Stream, and in the NBC eddies pathway. The maximum SLA forced variability ($\sigma_F^{All} \geq 10$ cm) is observed in the northern coast of the GoM, the east coast of US, the Loop Current, and the Colombian basin.
The intrinsic variability is substantial ($\sigma_I^{All} > 15$ cm) in two regions, the central GoM, and the Gulf Stream. Other regions with relatively large intrinsic variability ($\sigma_I^{All} \geq 9$ cm) are the NBC eddies pathway and the Colombian basin. All these regions are known for their high mesoscale eddy activity.

The variability ratio $\sigma_I^{All}/\sigma_F^{All}$ (panel M) shows that the regions near the coast, and the region eastern the Lesser Antilles are dominated by the forced variability ($\sigma_I^{All}/\sigma_F^{All} < 1$). In most of the region the intrinsic variability dominates ($\sigma_I^{All}/\sigma_F^{All} > 1$). In the central GoM, the Gulf stream, the Caribbean Sea and the NBC eddies pathway, the intrinsic variability has a high contribution to the total variability ($\sigma_I^{All}/\sigma_F^{All} > 2$). This is expected, since the mesoscale activity dominates in the region as mentioned above.

Comparing panel A and M,we observe that more variability the model produces, the larger the variability ratio ($\sigma_I^{LF}/\sigma_F^{LF}$), meaning that the regions with more total variability are less predictable. That is the case especially in the GoM, the GS, in the Colombian basin and the pathway of the NBC eddies.

4.1.1 High-Frequency variability (T<1.8 years)

As we mentioned before, the high frequency SLA variability (Fig.4.1, panel D) has a similar pattern as the total variability; this is mainly due to the mesoscale processes that dominate the variability spectrum over most of the region. So we observe a maximum variability ($\sigma_T^{HF} > 25$ cm) in the LC and GS regions; and high variability ($\sigma_T^{HF} > 12$ cm) in the west GoM and the Caribbean Sea.

The high-frequency SLA variability is mainly chaotic since it is dominated by mesoscale features, like eddies, and meandering currents. We expect then, a variability ratio $\sigma_I^{HF}/\sigma_F^{HF}$ higher than 1 indicating that the intrinsic variability dominates. We observe in panel P that this is true for most of the region except in shallow waters ($z < 200$ m) near the coast, where the $\sigma_I^{HF}/\sigma_F^{HF}$ ratio is smaller than one. We will come back to this feature in the following.

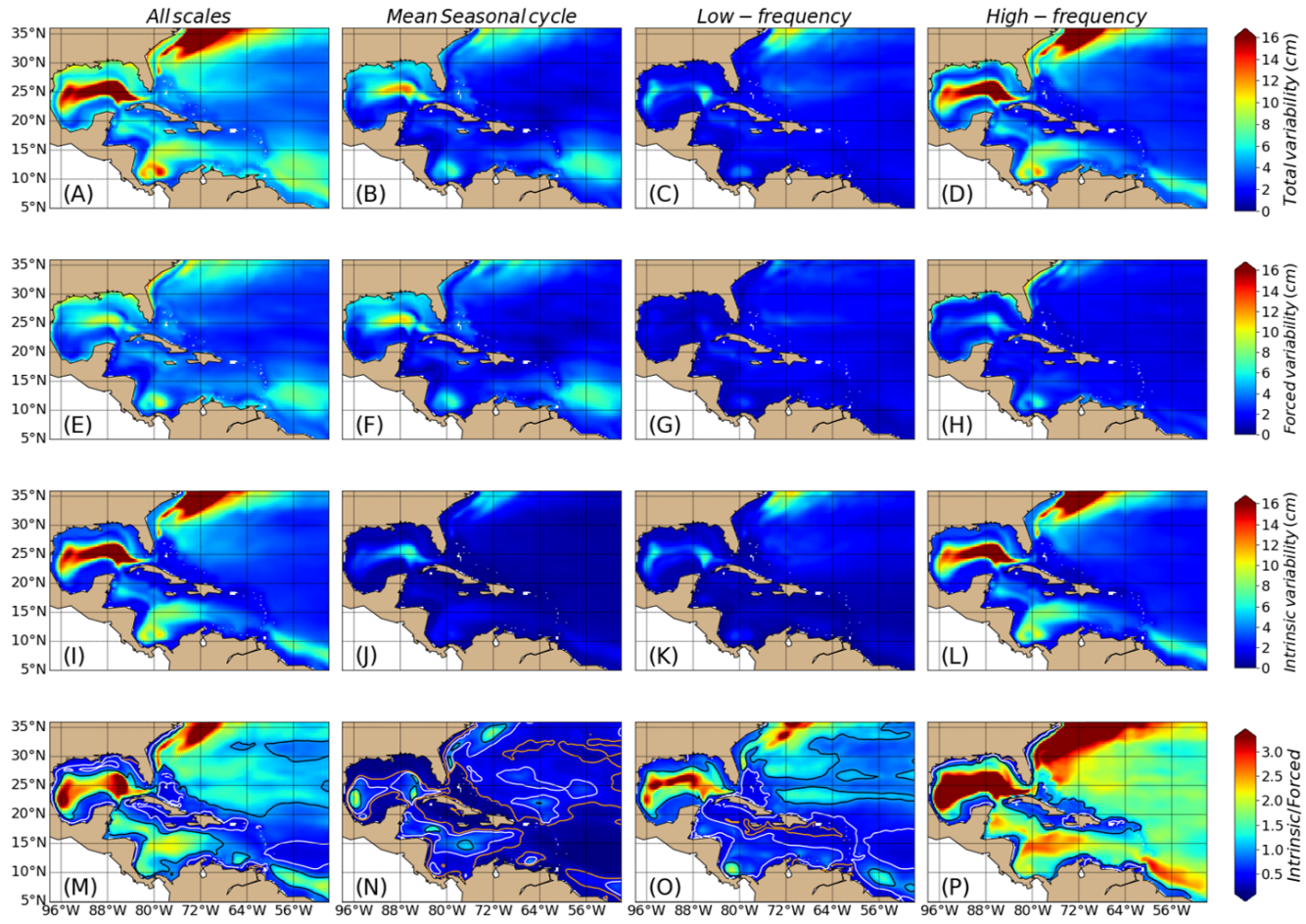

FIGURE 4.1: Maps of SLA standard deviation. Decomposition in frequency (columns) and by origin of the variability: Total (σ_T; first row), Forced (σ_F; second row) and Intrinsic (σ_I; third row). The last row represents the variability ratio σ_I/σ_F ; the contours represent ratio equal to 1 (black), 0.5 (white) and 0.3 (orange).

The regions with a maximum ratio, higher than 3, are the Loop Current, central GoM and the Gulf Stream (Fig.4.1, panel P). These are the areas where the intrinsic variability highly dominates due to different mesoscale features, we will describe each region separately.

Intrinsic variability

The region of the Loop Current has a maximum in the high frequency intrinsic variability ($\sigma_I^{HF} > 20$ cm). This high intrinsic variability ($\sigma_I^{HF} > 12$ cm) extends to the rest of the GoM. The Loop Current eddy shedding is a chaotic process, and we observe in our simulations that it has a period varying between 60 to 400 days (see Fig. 3.3); this indicates that the intrinsic variability dominates in a broad range of frequencies and especially in

the HF band ($T < 1.8$ years). The Loop Current eddies indeed have irregular pathways and random phases among the ensemble and keep their random character through their lives across the GoM, spreading intrinsic variability into the rest of the gulf.

The Gulf Stream region has significant high intrinsic variability representing another regional maximum ($\sigma_I^{HF} > 20$ cm). Mesoscale eddies are essential structures of the Gulf Stream circulation, making this a highly chaotic region ($\sigma_I^{HF}/\sigma_F^{HF} > 3$). Using the evolution of relative vorticity, we observe in the simulations a mix of anticyclonic and cyclonic eddies propagating and interacting. We observed two main different dynamic patterns: mesoscale eddies generated where the Gulf Stream follows the Eastern US coast (downstream of the Florida Current) and eddies propagating from the northeast.

The eddies generated in the Florida Current are constrained to the main Gulf Stream pathway and travel northward. The eddies observed there are mainly cyclonic structures, with a probable anticyclonic counterpart but smaller in size; these eddies interact between them while they propagate and then dissipate. More to the north, approximately at Cape Hatteras, we observe some cyclonic eddies that are bigger than the eddies generated along the coast; some of those eddies propagate from the north or northeast, with a possible origin in the Gulf Stream separation. These cyclonic eddies propagate to the southwest and interact with other mesoscale structures until their dissipation. An example of the structures observed in the Gulf stream is shown in figure 4.2 The high mesoscale activity and the interaction between structures make the Gulf Stream a highly chaotic region.

The North of Brazil is another region with a high variability ratio ($\sigma_I^{HF}/\sigma_F^{HF} \sim 2$). The relatively high intrinsic variability($\sigma_I^{HF} > 8$cm) of this region is mainly due to the mesoscale eddies that emerged in the North Brazil Current (NBC) retroflection, and that dominate the circulation of the area. We observe in the simulations that these eddies travel to the northwest, entering the Caribbean Sea through the Antilles passage and so, carrying intrinsic variability into the Caribbean Sea region. The NBC eddies are originated in the North Brazil Current retroflection with a marked seasonal cycle (Johns et al., 1990), and continually propagate northwestward along the coast (Barnier et al., 2001). The NBC eddies arrive at the Lesser Antilles, and some of the potential vorticity is advected into the Caribbean Sea (Murphy et al., 1999), which carries the intrinsic variability from the NBC into the Caribbean Sea.

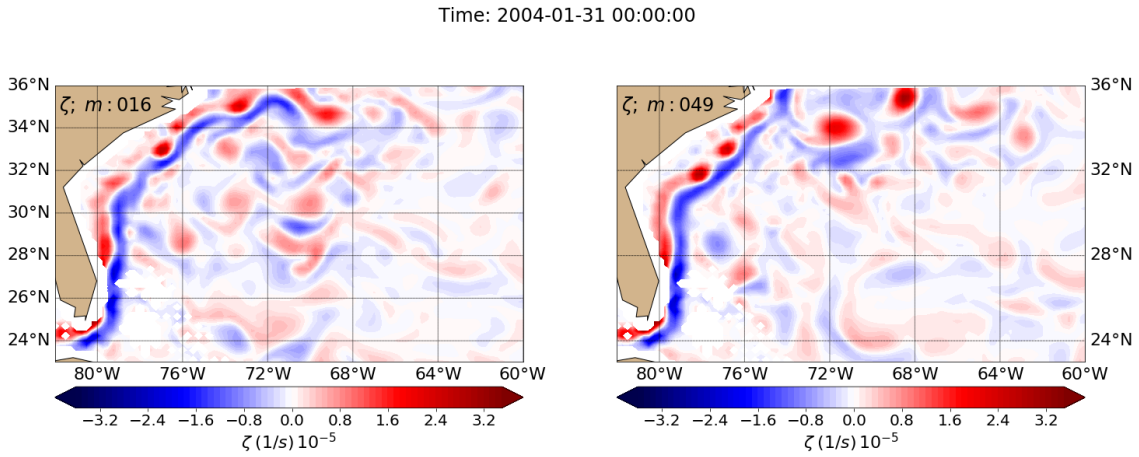

FIGURE 4.2: Snapshots of surface relative vorticity (ζ) in the Gulf Stream region. Two different members in the same day, indicating different structures of the Gulf Stream and the mesoscale activity in the region.

The NBC anticyclonic eddies arrive into the Caribbean sea, and they continue their northwest propagation to the Yucatan Channel. After crossing the Lesser Antilles passage the anticyclonic eddies interact with the Nicaraguan shelf, and are deflected to the north (Jouanno et al., 2008). During their passage through the Caribbean sea, the NBC eddies interact with the local mesoscale eddies and the topography of the region, generating smaller structures and intensifying some other eddies in the basin (Jouanno et al., 2009); the superposition of locally-formed and remotely-formed mesoscale structures explains the significant intrinsic variability ($\sigma_I^{HF} > 8$cm) in the region.

In figure 4.1 panel P, we observe that the $\sigma_I^{HF}/\sigma_F^{HF}$ in the whole Caribbean sea is higher than 1.5, which confirms that it is mainly a chaotic region. Inside the Caribbean Sea, the Gulf of Colombia is a region with a variability ratio that indicates that the area is mainly chaotic ($\sigma_I^{HF}/\sigma_F^{HF} > 1$), but it is a particular region (apart from the Loop Current) with large forced variability as well.

In the Gulf of Colombia, a cyclonic eddy dominates the circulation, which remains permanently in the basin but continually changes in size, intensity, and central position (e.g. figure 4.3). This so-called Panama-Colombia gyre has a local maximum in total variability (panel D) and in the intrinsic variability (panel L), both with variability higher than 10 cm. As we can observe in the four panels of figure 4.3 the PC gyre is a permanent cyclonic structure in the region; there is a similarity in the general cyclonic

structure between members during the same time step, nevertheless there are also differences on the intensity, the main core and in some moments in the extension of the structure. These latter differences in the structure evolution within different members makes the region highly intrinsic. Jouanno et al. (2009) obtained similar results: they observed that the Panama-Colombia gyre is a region with a local maximum of eddy variability and, they attributed the increase of variability in the area to the instability of the gyre that contributes to the formation and growth of local eddies. On the other hand, the high frequency intrinsic variability near the coast is weak ($\sigma_I^{HF} < 4$ cm); we observe this especially in areas shallower than 200 m.

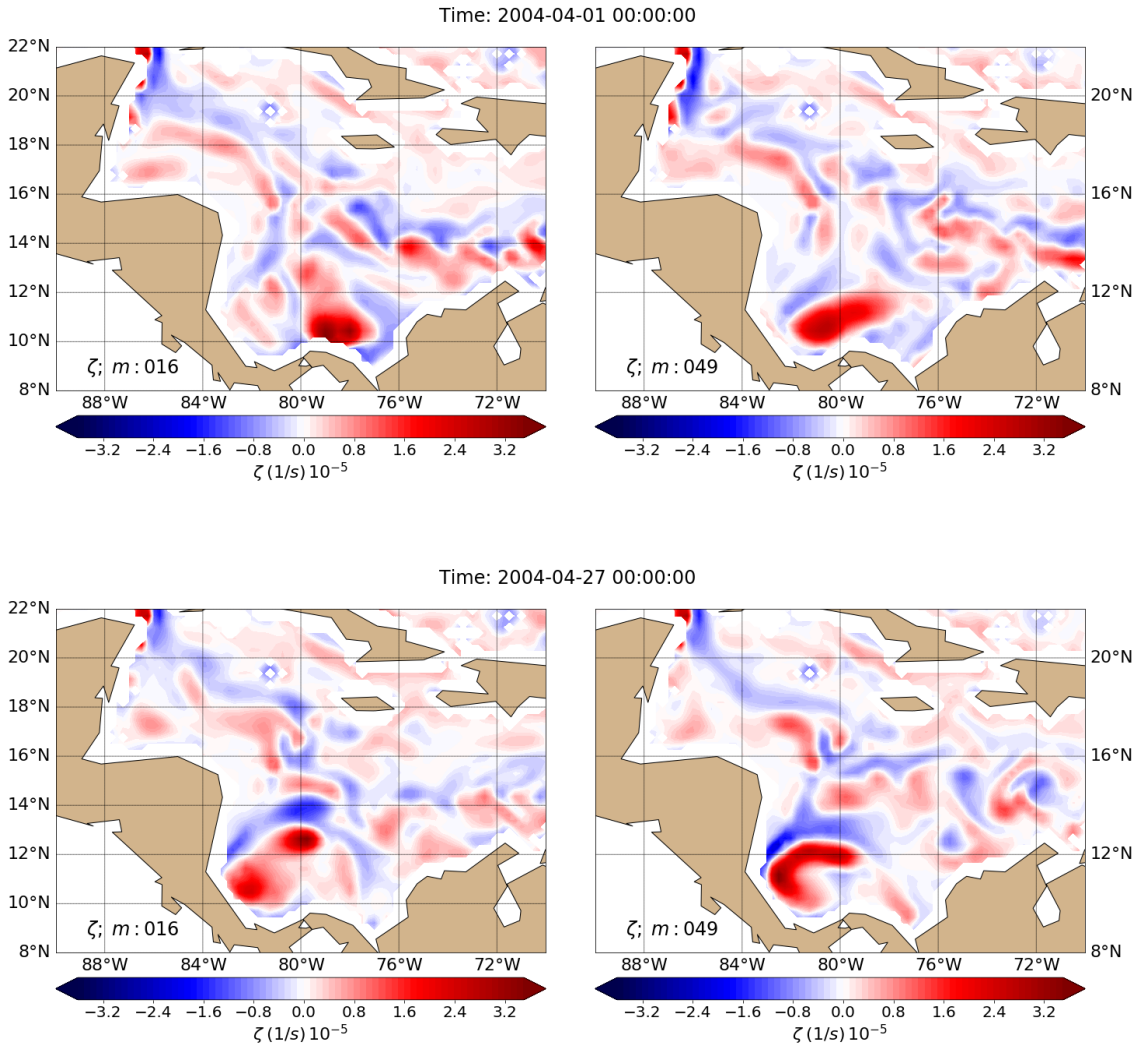

FIGURE 4.3: Surface relative vorticity (ζ) in the Caribbean sea. Two different members are shown on two different days indicating different states of the Panama-Colombia Gyre.

Forced HF variability

The high-frequency variability near the coast is mostly forced ($\sigma_I^{HF}/\sigma_F^{HF} < 1$). The coast, and specially the north GoM shelf and US coast, have a maximum in the high-frequency forced variability ($\sigma_F^{HF} \geq 9$ cm); this may be associated with a barotropic response to the atmospheric forcing of the ocean shallow waters. For example, we observed in our simulations that the high-frequency and highly energetic atmospheric phenomena, like hurricanes, cold fronts, and storms; generate surges and SSH slopes that trigger the propagation of coastally trapped waves. These coastally trapped waves are very coherent structures among all members and propagate along the shelf of the GoM in a counterclockwise direction. The coastally trapped waves have been observed in other studies and can be generated by hurricanes (Bilskie et al., 2016) or cold fronts (Jouanno et al., 2016). We describe in more detail this effect in section 4.2.5.

Other regions with relatively high forced variability are the Panama Colombia gyre ($\sigma_F^{HF} > 8$ cm) and the Gulf stream ($\sigma_F^{HF} > 6$ cm). In the region of the Loop Current, we also observe a relatively large contribution of variability ($\sigma_F^{HF} > 9$ cm) from the high frequency forced component.

4.1.2 Mean Seasonal Cycle

The mean seasonal cycle is mainly forced ($\sigma_I^{MSC}/\sigma_F^{MSC} < 1$) in the whole region, as expected (Fig.4.1, panel N). The maximum forced variability ($\sigma_F^{MSC} > 10$cm) of the mean seasonal cycle, is simulated in the Loop Current eddy shedding region. Other regions with considerable forced variability ($\sigma_F^{MSC} > 7$cm) are the northern GoM, the Gulf stream, the Colombian basin, and the pathway of the NBC eddies. The Mean seasonal cycle of the SLA variability is due to the seasonal cycle of two forcing components: the radiative forcing, which leads mainly to a thermosteric response of the ocean, and the seasonal cycle of the winds in the basin (Velasco and Winant, 1996).

The easterly winds in the Caribbean Sea and the GoM have an important seasonal cycle in the region, and there is a significant phase shift of 180° of the periods of maximum winds in the two regions. The easterly winds in the Caribbean sea are strong (weak) in summer and winter (spring and fall), while in the GoM, the easterly winds are strong (weak) in spring and fall (summer and winter) (Chang and Oey, 2012). This pattern in the winds can affect mesoscale processes in the region, Chang and Oey (2012) observed that this seasonality in the winds influenced the Yucatan transport and in consequence, the Loop Current extension.

The seasonality of the winds in the GoM is also influenced by he occurrence of storms in the basin. The hurricanes season occurs from May to November, with intense winds caused by tropical storms that cross the basin in different trajectories and directions. From September to May, the strong winds are mostly caused by cold fronts, having a strong southward component (Zavala-Hidalgo et al., 2014). These "winter" intense winds, could also explain the large forced variability observed in the northern GoM, where the cold front events are more intense and more frequent than the rest of the basin (DiMego et al., 1976), and which can cause coastally trapped waves.

The intrinsic variability of the mean seasonal cycle (Fig.4.1, panel J) is low in most of the region ($\sigma_I^{MSC} < 4$cm), even though there is a maximum in the Loop Current ($\sigma_I^{MSC} > 7$cm) and north of the Gulf Stream ($\sigma_I^{MSC} > 5$cm). In general, the variability ratio $\sigma_I^{MSC}/\sigma_F^{MSC}$ (Fig.4.1, panel N) is lower than 1 in most of the area, as expected for this frequency. Nevertheless, the intrinsic variability has a substantial contribution to the total variability in some regions ($\sigma_I^{MSC}/\sigma_F^{MSC} > 0.5$), which is surprisingly value for a phenomenon that is mostly attributed to the forcing in general; and it may be explained by the temporal inverse cascade of (chaotic) mesoscale kinetic energy towards interannual and longer time scales, which crosses the annual frequency (Sérazin et al., 2018).

4.1.3 Low-Frequency Variability (T >1.8 years)

The total SLA variability at low frequency (Fig.4.1, panel C) has the weakest standard deviation compared to other time scales. The maximum total low-frequency variability is observed in the Gulf stream ($\sigma_T^{LF} \geq 10$cm), the western GoM and the Loop Current ($\sigma_T^{LF} > 8$cm) regions. The low frequency forced variability (Fig.4.1, panel G) in general is weak ($\sigma_F^{LF} \leq 4$cm) in most of the basin but reaches a local maxima ($\sigma_F^{LF} > 4$cm) in the Loop Current, the western GoM, the Gulf stream, and the PC gyre.

Similar to the LF forced variability, the low-frequency intrinsic variability (Fig.4.1, panel K) reaches local maxima ($\sigma_I^{LF} > 8$cm) in the Gulf Stream, the Loop Current, and the western GoM; and in the rest of the region the intrinsic variability is moderate ($\sigma_I^{LF} \leq 4$cm). Even though the low frequency intrinsic variability is weaker than at higher frequencies, it dominates in a considerable part of the region as the variability ratio $\sigma_I^{LF}/\sigma_F^{LF} > 1$ indicates (Fig.4.1, panel O). The regions where the low-frequency intrinsic variability exceeds the forced variability ($\sigma_I^{LF}/\sigma_F^{LF} > 1$) are the Gulf Stream, the GoM, the PC gyre, and the NBC eddies pathway. Nevertheless, most of the rest of the region also has a substantial contribution of intrinsic variability ($\sigma_I^{LF}/\sigma_F^{LF} > 0.5$). Such

a proportion indicates that intrinsic variability cannot be neglected when interpreting observed or simulated variability throughout most of the region.

Panel O shows that our $1/4^\circ$ model produces a significant amount of low frequency intrinsic variability, where the high frequency intrinsic variability itself is largest. A similar behaviour has been observed in other studies of the SLA variability: Sérazin et al. (2018) in particular suggested that this effect may be related to local temporal inverse cascade of kinetic energy which non-linearly feeds LF chaotic variability in regions where mesoscale activity is large.

4.2 Non-Gaussian metrics: Entropy.

We must recall that the instantaneous ensemble PDFs in some regions of the basin are not Gaussian, and this is the first reason why we decided to look for another method that does not assume Gaussianity. This new method allows us to quantify not only the magnitude of the intrinsic variability in a region but also how it evolves and how the atmospheric forcing modulates it. In this section, we describe the results obtained using entropy (defined in section 2.5.2) as a metric of the constraint exerted by the atmosphere on the oceanic intrinsic variability, which to some extent, complements the analysis of the intrinsic variability that we talked about in the previous section. As we explained in definition of the entropy, the metric does not consider the intrinsic and the forced variability as independent variabilities.

4.2.1 Initial growth of intrinsic variability

Intrinsic variability is seeded by the stochastic perturbations activated during 1993 in the equation of state. This yield a quasi -exponential growth of the ensemble spread, with different time scales. The growth rate of intrinsic variability may be deduced from a simple analysis of the ensemble spread itself, but this moment of daily PDFs is not adequate to characterize the dynamics in regions where non-Gaussianity prevails. We therefore investigate the growth of intrinsic variability from the evolution of entropy, which more accurately quantifies how the atmospheric constraint on the intrinsic variability decreases in time as non-linearities feed the ensemble dispersion.

To illustrate the types of regions and the growth of intrinsic variability based on the growth of entropy, we show in figure 4.4 some snapshots of instantaneous entropy and in figure 4.5 the evolution of entropy in different locations.

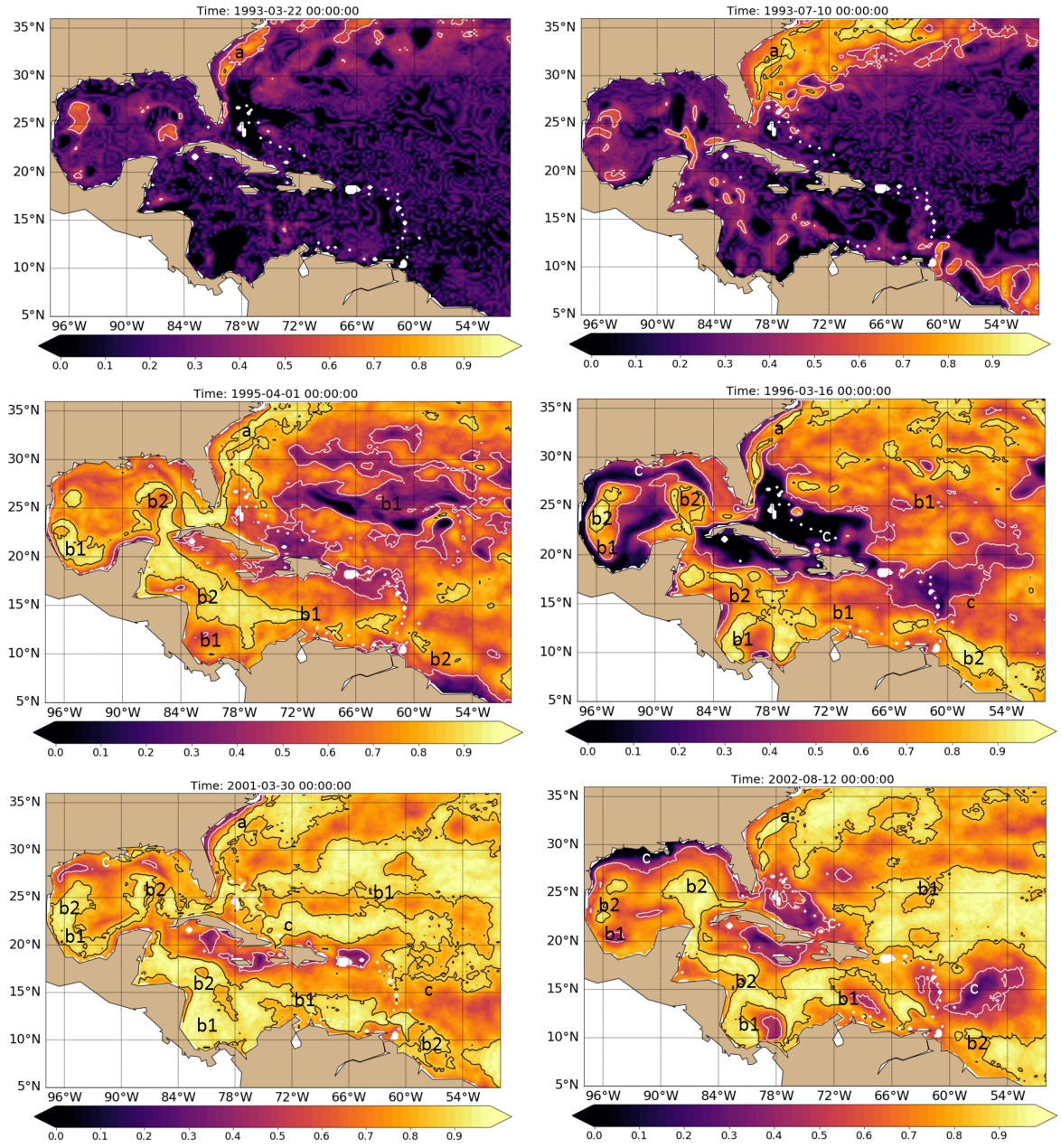

FIGURE 4.4: Snapshots of entropy (S) at different time steps to illustrate the evolution of the entropy in the region. The letters in maps, refer to the different types of regions according to the growth of intrinsic variability (refer to the text for explanation). White and black lines represents the 0.5 and 0.85 entropy contours.

The first type of region is one that has a rapid growth of intrinsic variability and reaches a maximum entropy level close to one, a value that remains almost constant, with a small range of fluctuations ($S_a[0.8, 0.95]$); In this type of region the intrinsic variability emerges and grows rapidly in the first 12 months of simulation, and an example would be the Gulf Stream (marked in the maps with the letter *a*).

The second type of region refers to those regions where intrinsic variability emerges rapidly, fluctuating largely ($S_b[0, 0.95]$) in the first 24-36 months and reaching its maximum entropy level approximately after 48 months of simulation. In general, these regions have a high and quasi-steady value of entropy ($S_b > 0.85$), and may or may not have a broad range of fluctuation ($S_{b1}[0.1, 0.99]$, $S_{b2}[0.8, 0.95]$); An example of this type of region would be the Loop Current, the PC gyre, the western GoM, and the NBC pathway (shown in the figure 4.4 represented by b regions).

The third type of region (c regions in figure 4.4) that we observe, are those areas where the intrinsic variability emerges gradually (24-48 months), until reaching a semi-stable level of moderate entropy ($S_c[0.6, 0.8]$) but with a considerable fluctuation in time ($S_c[0, 0.95]$); An example would be the northern coast of the GoM, the coast around the Greater Antilles and at the East of the Lesser Antilles. The figure 4.5 shows an example of the different types of region according to their growth of intrinsic fraction.

Due to this significant difference in the growth rate of intrinsic variability in the region, we decided to use the entropy time series since a semi-stable value was observed over most of the basin; therefore, the period considered for future analyses is 1997 to 2011. In the next subsections we will describe the entropy evolution and its modulation by the atmosphere.

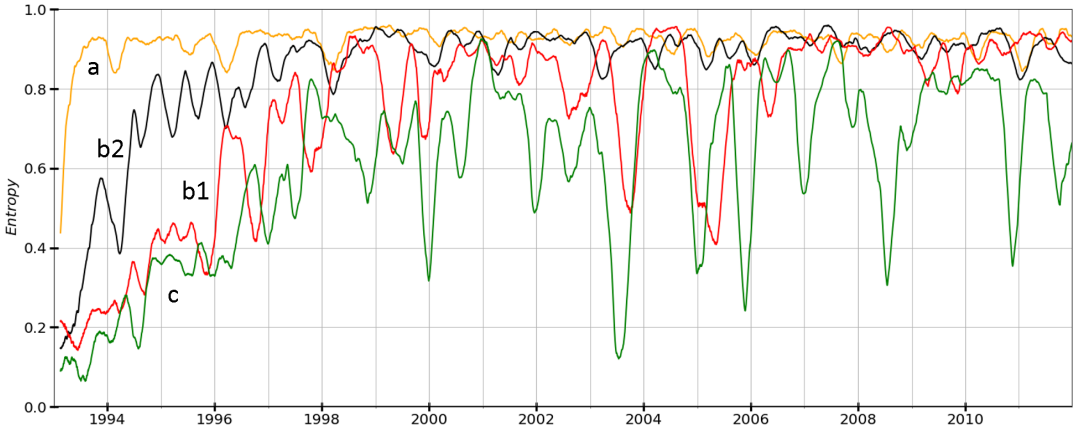

FIGURE 4.5: Examples of the evolution of the entropy of the different types of regions according to the growth rate of entropy. For better visualization of the entropy evolution, the time series were smoothed with a runmean window of 30 days.

4.2.2 Mean entropy and its modulation in time

We study the evolution of entropy using the same frequency separation as in the previous sections, in order to associate the modulation of the intrinsic variability to physical processes both in the ocean and in the atmosphere. In the following sections, we describe and discuss the entropy of the filtered SLA fields, meaning that we first filtered the time series, and then we applied the entropy methodology to each frequency band.

Let us recall that our ensemble is designed with 50 members that have an initial condition slightly perturbed, but have the same atmospheric forcing. So, the changes in the temporal evolution of the entropy are due to the presence or absence of atmospheric constraint in the ocean variability. To summarize the information on the evolution of the entropy at each location, we calculate the time-mean entropy and the standard deviation of the entropy in time. The average of the entropy indicates the mean constraint exerted by the atmosphere on the oceanic intrinsic variability, while the standard deviation of the entropy quantifies the fluctuations of this constraint.

First, we analyze the entropy of the "all-frequencies" SLA to describe in a general way, the behavior of the North Subtropical Atlantic. In figure 4.6 panel A and B, we present the temporal mean entropy and its temporal standard deviation, respectively. We found that, in general, the time mean entropy is greater than 0.5 in the whole basin. The values observed in the average and standard deviation of entropy indicates that the regions where the variability is chaotic are the Gulf Stream, the Loop Current, the western GoM, the central Caribbean Sea, and the NBC eddies pathway; these regions have an average entropy value higher than 0.9 quasi-steady over time ($S_{std} < 0.05$).

On the contrary, in areas near the coast, especially around Cuba and the shelf around the GoM, we observed a moderate average entropy ($S_{mean} \sim 0.5$) and a considerable variation of entropy ($S_{std} > 0.2$), with a wide fluctuation range ($S[0, 0.9]$); these entropy values indicate that the intrinsic variability is highly modulated by the atmosphere. What is happening in the region is that the mesoscale eddies usually dominate the circulation of these regions, making it a chaotic area, but given the shallow depth of the area, the atmosphere can intermittently have a more significant and more homogeneous impact in the response of the ocean. We observed this large modulation of the intrinsic variability in the time series of entropy, where events like storms can modulate the large intrinsic variability in the ocean, pushing the 50 members into a similar extreme state; we are going to discuss this in more detail in section 4.2.4. There is a third type of region, those areas where entropy is large ($S_{mean} > 0.8$) but also its variation in time

($S_{std} > 0.15$), which is interpreted as those regions where the intrinsic variability dominates but can be highly modulated by the atmosphere; these areas are the eastern part of the region of study and the eastern Caribbean Sea.

In summary, we observe regions where the atmospheric modulation of the entropy is important, like near the coasts, and regions that are mainly chaotic with almost not significant decreases due to the atmospheric forcing like the Gulf Stream and the Loop Current. Nevertheless, this atmospheric modulation of the intrinsic variability can differ from one frequency to another. We are thus going to analyze separately the modulation of the entropy of the mean seasonal cycle, and of the high and low frequencies.

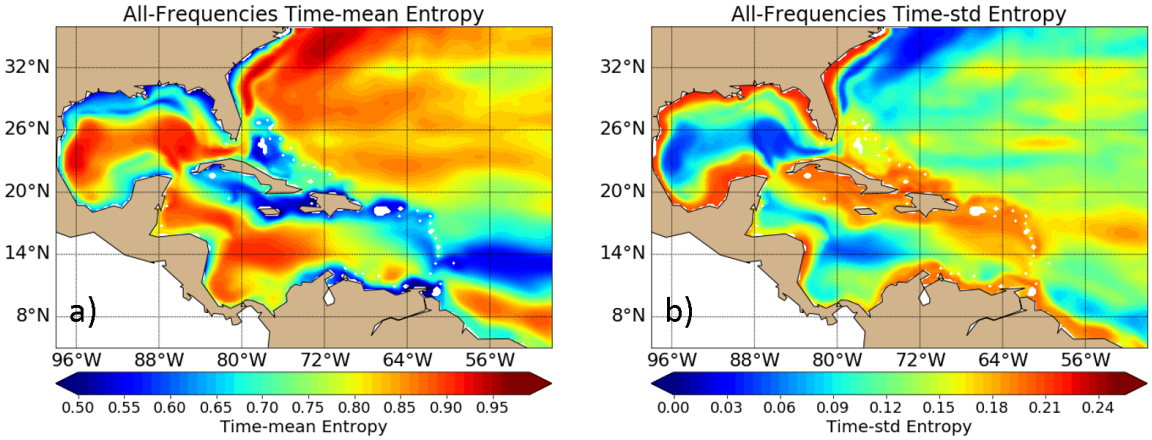

FIGURE 4.6: Maps of the time mean and standard deviation of the entropy of the SLA at all frequencies for the period 1997-2011.

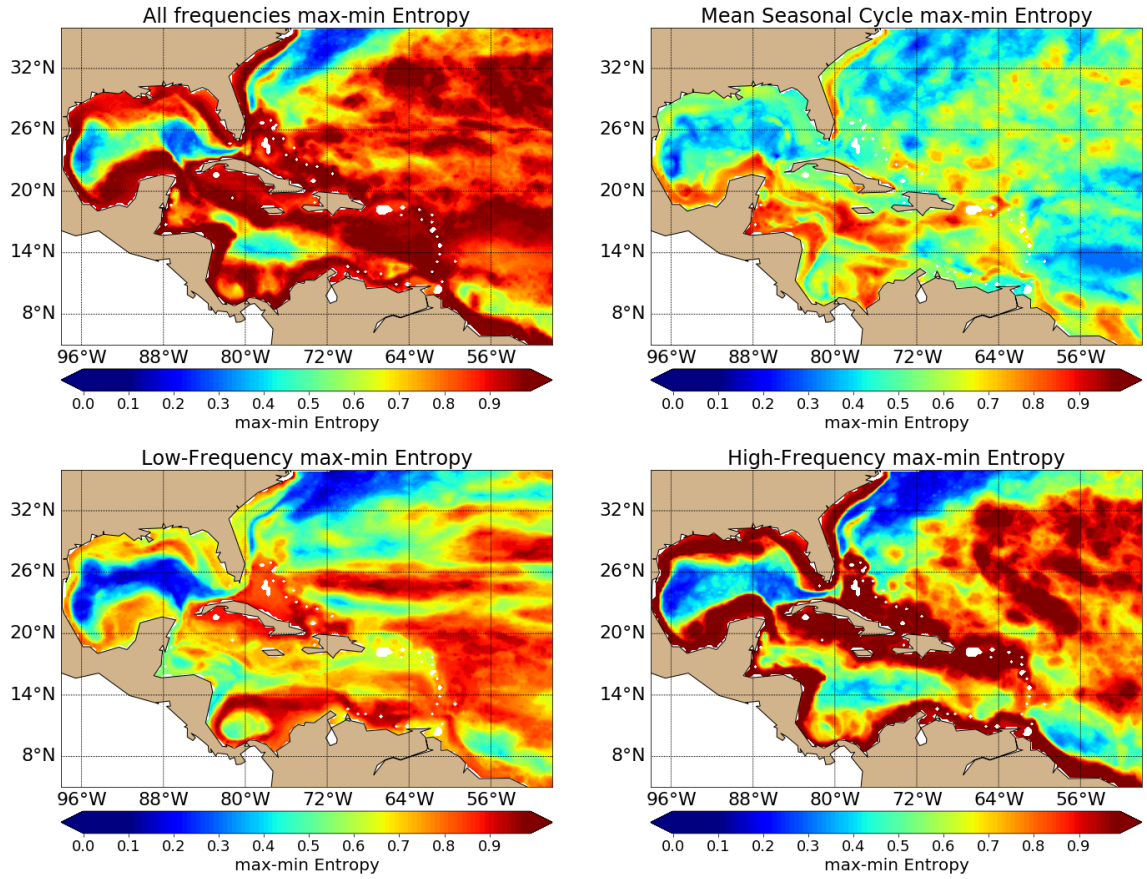

FIGURE 4.7: Maps of the maximum minus minimum entropy of SLA for the period 1997-2011.

4.2.3 Relationship between Gaussian and non-Gaussian metrics

We now look for a possible relationship between the results obtained with the Gaussian assumption methods and the non-Gaussian assumption methods (entropy). The values of the intrinsic to total variability ratio (σ_I/σ_T) at each location are compared to the mean value of entropy. Figure 4.8 shows a scatterplot of the square time-mean entropy (Y-axis), and the σ_I/σ_T variability ratio (X-axis). Figure 4.8 shows an almost linear relationship between these two variables, where high (low) mean entropy values correspond to high (low) σ_I/σ_T ratios. This results shows that the Gaussian and non-Gaussian methods provide very consistent results: high intrinsic variability (σ_I/σ_T large) means large mean entropy and weak constraint of the atmospheric variability on the ocean.

Colos in figure 4.8 indicate the temporal standard deviation of entropy. As shown in the previous section, results confirm that regions with large time mean entropy have

small entropy variability, but the regions with small or medium time-mean entropy $(0.2 - 0.6)$ may be associated with either small or large entropy fluctuations.

Our entropy metric is not only consistent with the σ_I/σ_T ratio; it has three advantages over it. [1] It is line with the dynamical Systems Theory since no questionable splitting between forced and intrinsic variability is made (the entropy characterizes the atmospheric influence on the ocean chaotic variability).[2] It is more general since it is valid in both Gaussian and non-Gaussian cases; [3] It naturally provides the time dependence of the atmospheric constraint exerted on the oceanic chaotic variability. Identifying the origin of this tight relationship would require analytical developments, which are left for the future.

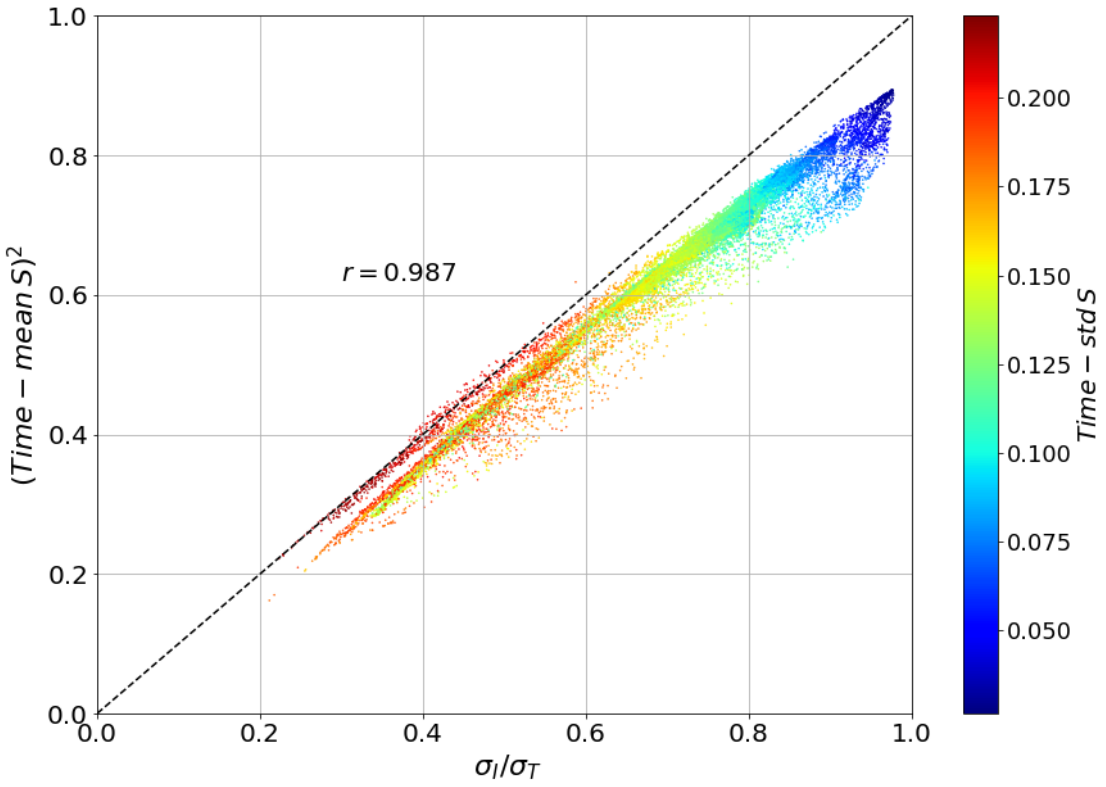

FIGURE 4.8: Intrinsic to total variability ratio σ_I/σ_T versus square time mean entropy for the full variability. In colors is represented the time standard deviation of the entropy.

4.2.4 High-Frequency Entropy.

In figure 4.9a, we observe that the average entropy of High-Frequency SLA is higher than 0.8 over most of the basin, except near the coasts where it occasionally drops below 0.08. The standard deviation of HF entropy is maximum ($S^{HF}_{std} \sim 0.2$) near the coasts, while in deep waters the standard deviation of entropy is minimal ($0.03 - 0.10$. An exception is found in the eastern part of the basin ($50° - 72°$W,$14° - 32°$N) or south to the Sargasso Sea where we observe a significant variability of HF entropy ($S^{HF}_{std} > 0.15$) in deep waters.

We observe that the Gulf Stream, the Loop Current, and the Western GoM are regions with a low range of HF entropy variability ($S^{HF}_{max} - S^{HF}_{min} < 0.2$, see Fig. 4.7) and a low $S^{HF}_{std} < 0.05$. The constraint exerted by the atmosphere on the HF oceanic intrinsic SLA variability is persistently weak in such eddy active regions. We have other chaotic regions ($S^{HF}_{mean} > 0.9$), like the NBC eddies pathway or the Caribbean Sea, that have a moderate $S^{HF}_{std} \sim 0.1$ but with a wide range of entropy variability ($S^{HF}_{max} - S^{HF}_{min} > 0.6$). These are regions where we observed a significant atmospherically-driven reductions of the HF intrinsic fraction at some specific times.

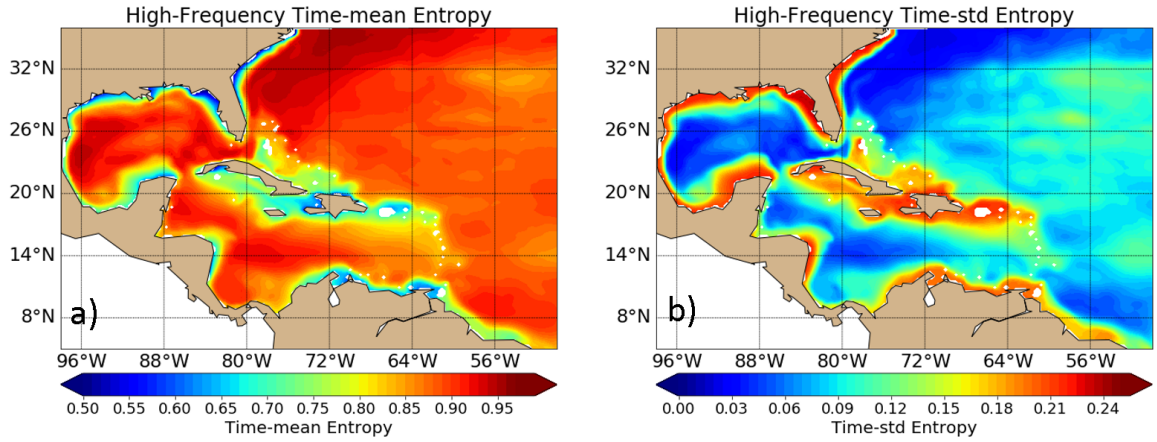

FIGURE 4.9: Maps of the time mean and standard deviation of the entropy of High-Frequency SLA for the period 1997-2011.

Near the coasts, we observe that the HF entropy can vary a lot and that the high-frequency has a wider range of entropy variability than other frequency bands: the S can reach its maximum ($S^{HF} = 1$) and minimum ($S^{HF} = 0$) values, indicating a considerable modulation of the intrinsic variability by the atmosphere. A possible physical explanation of this high modulation of the intrinsic variability near the coasts is the presence of high-frequency phenomena in the atmosphere that can modulate the chaos in

areas where shallow waters are much more responsive to high-frequency wind anomalies. This phenomena is investigated in more detail in the following.

4.2.5 Modulation of the entropy by storms

Hurricanes and entropy

Hurricanes are very energetic phenomena in the atmosphere that can modulate the HF entropy in the ocean. We present an example of such modulation in figure 4.10. The top panels show two snapshots of instantaneous entropy before and during the passage of hurricane Katrina (wind shown as arrows). The time series shows the evolution of the ensemble-mean SLA, its ensemble standard deviation in shadow, and the evolution of entropy in 6 coastal locations around the GoM.

As we can observe in the first snapshot and in the time series, the entropy is large over most of the basin($S > 0.7$), and between 0.6 and 0.8 along the coast before the strike of the hurricane. A couple of days later when hurricane Katrina hits the coast of Florida, the entropy decreases considerably, reaching almost zero. The ensemble-mean SLA shows that right after the strike of the hurricane, a storm surge occurs along the coast. The minimum entropy propagates as a coastally trapped wave all over the GoM anti-clockwise. The wave of minimal entropy originates in the Florida peninsula over the GoM shelf ($\sim$ 200m deep), and it propagates along the GoM. This wave takes approximately ten days to cross the gulf and reach the Yucatan peninsula, but it does not reach the Peninsula with the same intensity as it started, presenting entropy values greater than 0.2 at the end. This minimum of entropy propagating as a coastally trapped wave is mainly observed when a hurricane or storm hits the coast of Florida, and when a major hurricane strikes any part of the northern GoM. This wave is a particular effect in the gulf, distinct from the effect of hurricanes on the entropy in deep waters.

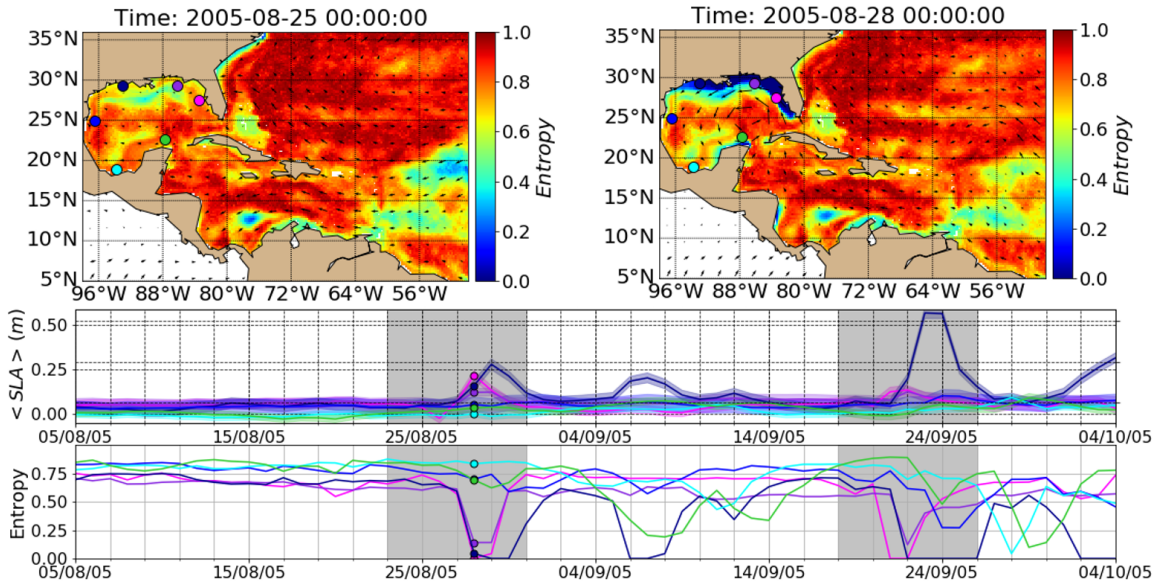

FIGURE 4.10: Maps of instantaneous HF entropy before (left) and during (right) the strike of hurricane Katrina. Evolution of the ensemble-mean SLA (upper) and entropy (lower) time series along the coast of the GoM. The gray shadows represent the period when a major hurricane strikes the GoM. The colors of the lines corresponds to the locations in the map. The colored dots in the time series corresponds to the date in the second map.

We observe another impact of the tropical storms on the ocean entropy that it is similar in open waters (mainly east of the Greater Antilles) and in the Caribbean Sea. This second effect of hurricanes is especially noticeable in HF entropy but can also be observed in the total entropy. We observe a sudden decrease of entropy in a considerable ocean region, with an extension similar to the size of the storm. This area of minimal entropy propagates in a trajectory similar to that of the tropical storm. An example of this drop of entropy in deep waters, is the hurricane Igor in September of 2010. Figure 4.11 shows some snapshots of the passage of the hurricane in the eastern region. Before the passage of the hurricane (panel a), the entropy in most of the region is large ($S > 0.85$). When the hurricane, category 4, arrives into the region, we observe a zone of minimum entropy ($S \sim 0.2$) around the eye of the hurricane. This zone of minimum entropy moves with the storm, reaching values of entropy near zero. A certain point, the area of minimal entropy, not only moves with the storm, but it spreads along the hurricane trajectory (panel d). The area of low entropy remains for a couple of days after the passage of the hurricane (panel f), and then it vanishes, meaning that the ocean entropy returns to its natural state. In other words, before the hurricane arrival the ensemble members exhibit a diversity of the HF sea-level fields (mostly due to mesoscale activity) that the

current atmospheric state only slightly manages to reduce ($S > 0.8$) with respect to the reference PDF. A hurricane yields considerable amount of information that pull all the members into a few SLA deciles over a short period, hence reducing the entropy.

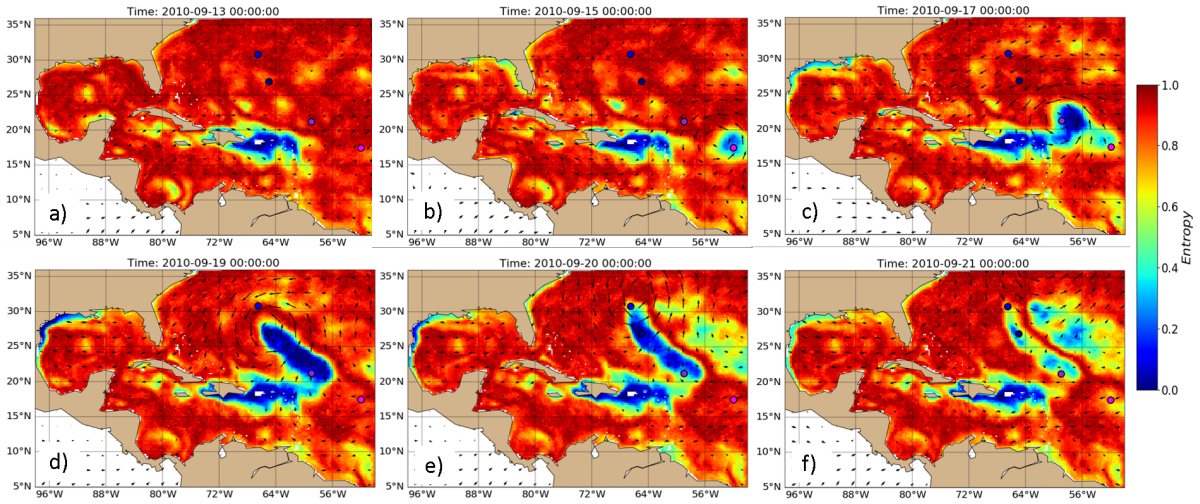

FIGURE 4.11: Maps of instantaneous entropy during the passage of hurricane Igor 2010. The entropy minimum bulk appears with the hurricane and travels with it.

In the Caribbean Sea, given the small size of the basin compared to the high speed at which the storms usually translate, the zone of minimum entropy is smaller and propagates within the basin depending on the trajectory of the storm. The area of minimum entropy disappears when the storm (and the minimum entropy bulk) touches one of the coasts (the Greater Antilles or Yucatan). In general, we observe that within the Caribbean Sea, the effect of hurricanes (even major hurricanes) have little effect in modulating the entropy of the region.

Cold fronts and entropy

We explained in section 1 that the Gulf of Mexico is affected by cold fronts from October to May. These cold fronts generate intense winds with a preferential meridional component (DiMego et al., 1976). We observe that these cold fronts generate a minimum of entropy ($S < 0.2$) in the north shelves (LATEX, MAFLA, and WFM, see Fig. 1.1 for reference) of the Gulf of Mexico. Figure 4.12 shows an example of the effect of a cold front on the entropy in the GoM. Similar to the effect of the hurricanes, the minimum of entropy propagates along the coast as a trapped wave, reaching the Yucatan Peninsula after 6-11 days. Depending on the direction of the front, the minimum of entropy can be

generated in the northwest GoM (i.e., LATEX shelf) or on the Florida coast (WFM shelf). We observe that the intensity of the winds, and the extension of the cold front, influence the minimum of entropy propagation. In some cases, the minimum of entropy only reaches the central GoM (TAVE shelf), and on some other occasions,it reaches the Yucatan Peninsula (like the example in figure 4.12). In a few extreme events, the minimum of entropy was generated and propagated along the GoM, the Caribbean Sea coast, and sometimes reached the Brazilian coast.

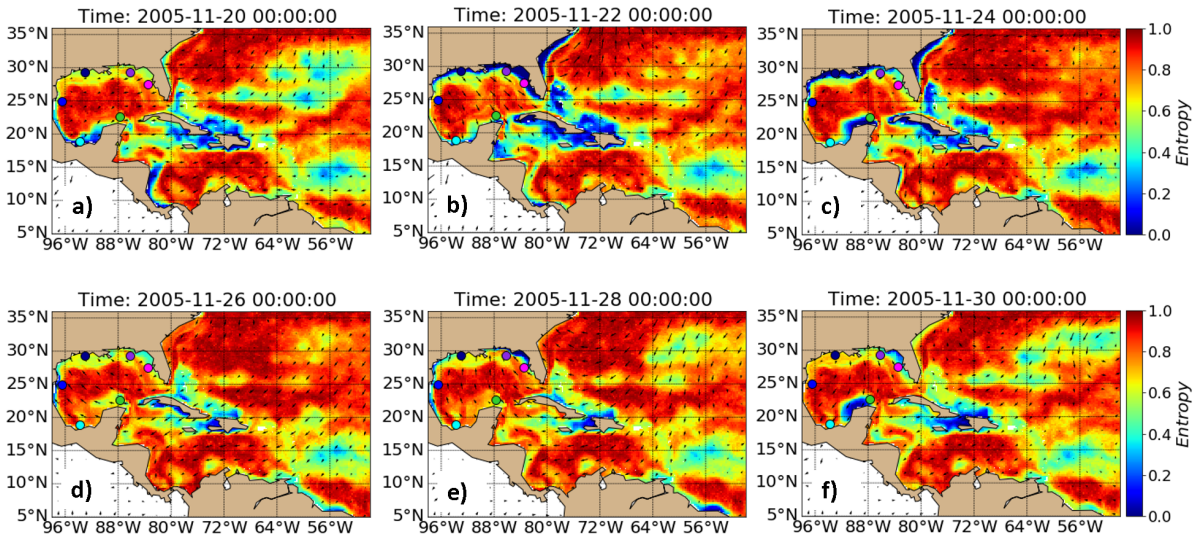

FIGURE 4.12: Maps of instantaneous entropy during cold front event. The entropy minimum bulk appears in the northern GoM, when the event starts on the 22/11/2005. Then the minimum of entropy travels along the GoM coasts as a coastally trapped wave, reaching the Yucatan peninsula approximately 8 days after.

These coastally trapped waves in the Gulf of Mexico have been reported before by several studies with observational data (e.g. Dubranna et al., 2011; Rivas, 2017) and simulations (e.g. Jouanno et al., 2016). These authors suggested that intense storms like hurricanes in summer and the cold fronts in winter, generate the coastally trapped waves. This is what happens here in all ensemble members, where the "usual" dispersion of SLA fields due to non-linearities is sharply replaced by much more extreme (hence "informative") high SLA values, which then propagate around the Gulf.

We observe in this study that the storms in the region like hurricanes and cold fronts are extreme events in the atmosphere capable of modulating the intrinsic oceanic variability. These storms modulate the local intrinsic variability, but the ocean's response to the storm can propagate so that we can observe events forced remotely. After the

passage of the storm, the chaotic nature of the variability is restored, these regions have a large variability of the entropy, i.e. large modulation of the intrinsic variability.

4.2.6 Low-Frequency entropy modulation

We observe that over most of the open ocean and the Caribbean Sea the entropy of the Low-Frequency SLA has large variability ($S^{LF}_{std} > 0.15$) and moderate average ($S^{LF}_{mean} < 0.8$) over time, except in the GS and the GoM regions. The Gulf Stream and the Gulf of Mexico remain with high mean entropy ($S^{LF}_{mean} > 0.9$) and lower variability ($S^{LF}_{std} < 0.05$) over time, indicating that the intrinsic variability dominates over a wide range of time scales and that the atmospheric forcing has no effect in the LF oceanic intrinsic variability in these regions. In other words, the atmospheric evolution can barely reduce the uncertainty on the evolution of SLA up to interannual time scales there.

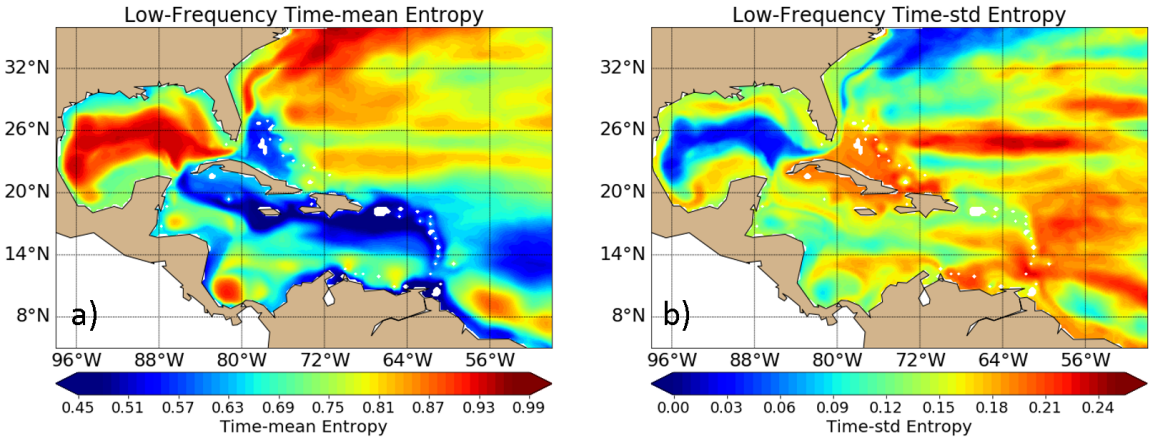

FIGURE 4.13: Maps of the time mean and standard deviation of the entropy of the Low-Frequency SLA for the period 1997-2011.

In open waters (eastern region), we observe a more significant average ($S^{LF}_{mean} > 0.75$) and variability ($S^{LF}_{std} > 0.18$) of the LF entropy than in other timescales. We observed that events with low entropy occupy large areas of the region, especially in the Caribbean Sea and in the open waters. These events of low LF entropy can last several months, remaining in the same area or propagating through regions. Figure 4.14 shows an example of an event with low entropy that occupied a large area and lasted more than one year. The low entropy region started in the eastern part (near to Brazil) in September 2002, it arrived and occupied the Caribbean Sea and around the Antilles at the beginning of 2003. The event lasted for several months around the Antilles and vanished by October 2003. Like this event, we observed several events that occupied a large region

of the Subtropical North Atlantic and that slowly propagated through regions.

We observed other events with minimum LF entropy, that propagates slower and spanning in a bigger area than in other frequencies; this suggests that the modulation of the low frequency entropy is more coherent in space. We will discuss this propagation of entropy in more detail in section 4.2.8.

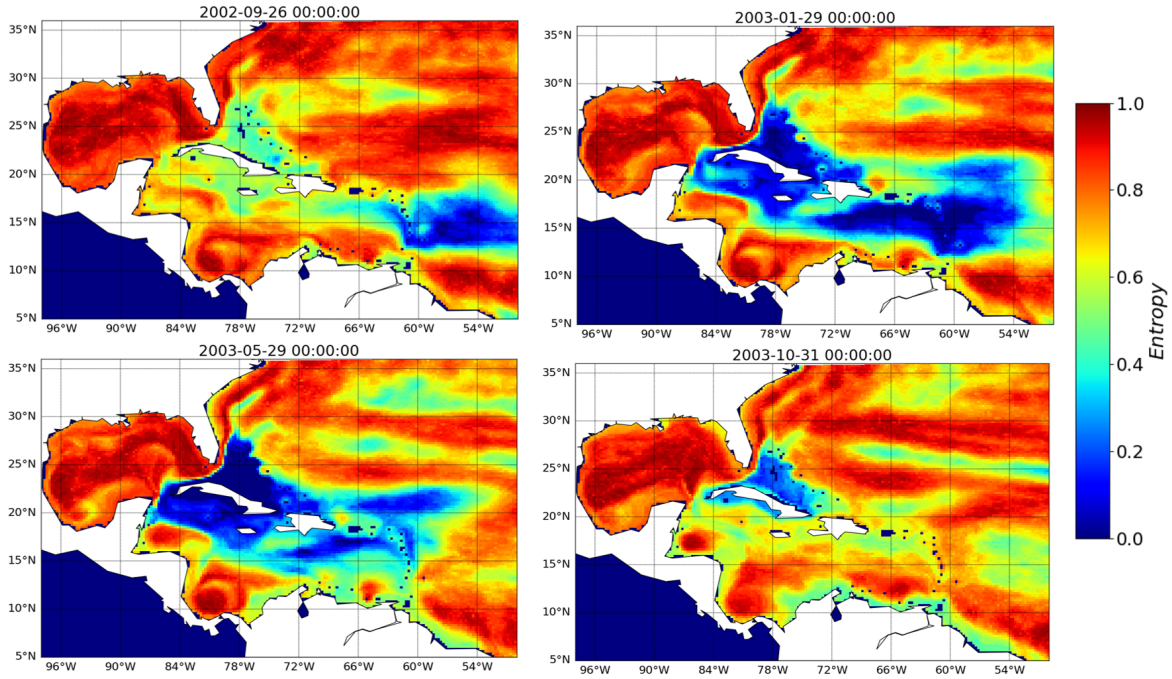

FIGURE 4.14: Instantaneous Low-Frequency entropy during a low entropy event over the Caribbean Sea.

4.2.7 Mean seasonal cycle entropy modulation

The Mean Seasonal cycle entropy, contrary to what would be expected, has an important intrinsic fraction in several regions of the subtropical North Atlantic. We observe in figure 4.15 that the Gulf Stream, the Loop Current, the western Gulf of Mexico, and the Caribbean Sea are regions with large ($S^{MSC}_{mean} > 0.85$) time average MSC entropy. Therefore, in these regions the mean seasonal cycle differs substantially among the members due to their individual realizations of the intrinsic variability at annual time scales. This questions the statement that seasons deterministically determine the ocean's mean seasonal cycle in the turbulent regime, at least in terms of SLA. On the contrary, the northern GoM, around Cuba, and the region east of the Antilles have a low ($S^{MSC}_{mean} < 0.2$)

average MSC entropy. There, the mean seasonal cycle is largely determined by the atmospheric driver.

The spatial pattern of variability in time of the MSC entropy (S_{std}^{MSC}) is different from the one at other time scales. In most of the region, the S_{std}^{MSC} is moderate with values around $0.08 - 0.12$, we do not observe a particular region with low variability of the MSC entropy. We observe that the southern GoM and the Caribbean Sea are particular regions with a large standard deviation ($S_{std}^{MSC} > 0.2$) of the MSC entropy.

Something important to notice about the entropy at this time scale is that it does not seem to be a linear relationship between the mean and the standard deviation of entropy, that is, regions with high (low) mean entropy do not have low (high) variability of entropy, as it happens at other frequencies. With our results, we can say that the intrinsic fraction of the Mean Seasonal Cycle is much more complicated than it seems and not completely determined by the atmospheric forcing, unlike usually thought.

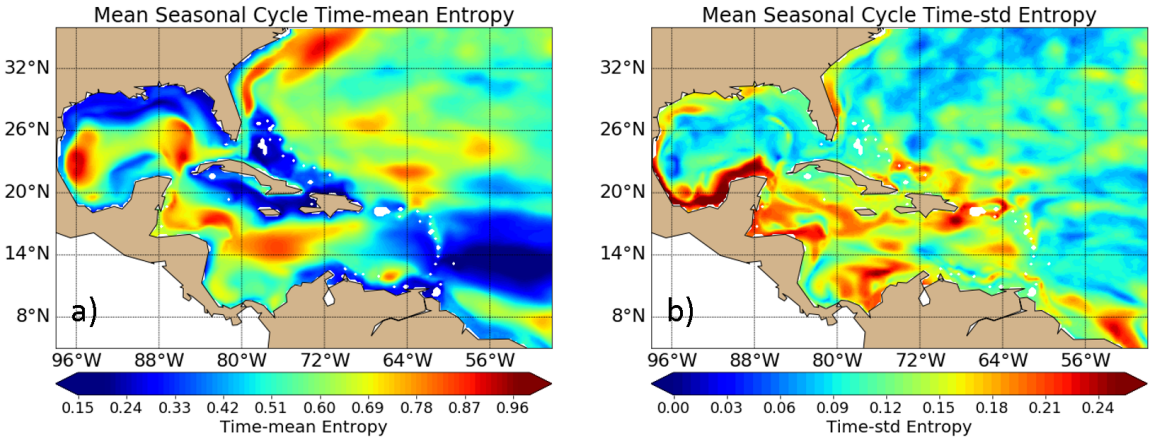

FIGURE 4.15: Maps of the time mean and standard deviation of the entropy of the mean seasonal cycle of SLA for the period 1997-2011.

4.2.8 Propagation of information

As mentioned above, we observed that sometimes a minimum or maximum of entropy can propagate and spread over the region. We especially observed HF minimum entropy events generated by storms that could propagate and were directly related to the oceanic physical process like coastally trapped waves. We also observed events of minimum LF entropy that spread over a large area and lasted for a long time, but these events are more difficult to relate directly to any phenomena in the atmosphere and

require more research. However, these types of events are important and could be an indicator of the potential predictability of the SLA variability.

We present an example of the propagation of entropy in figure 4.17, which shows the Hovmuller of entropy at different frequencies. The positions used to plot the route (Fig 4.16) are based on the typical flow of the region, i.e., we start in the eastern region of the Antilles, continue into the Caribbean Sea, and enter the GoM through the Yucatan Channel. We follow the flow to a characteristic position on the Loop Current, exiting the gulf through the Florida Strait, and finally head north as the average flow does, ending in the Florida Current.

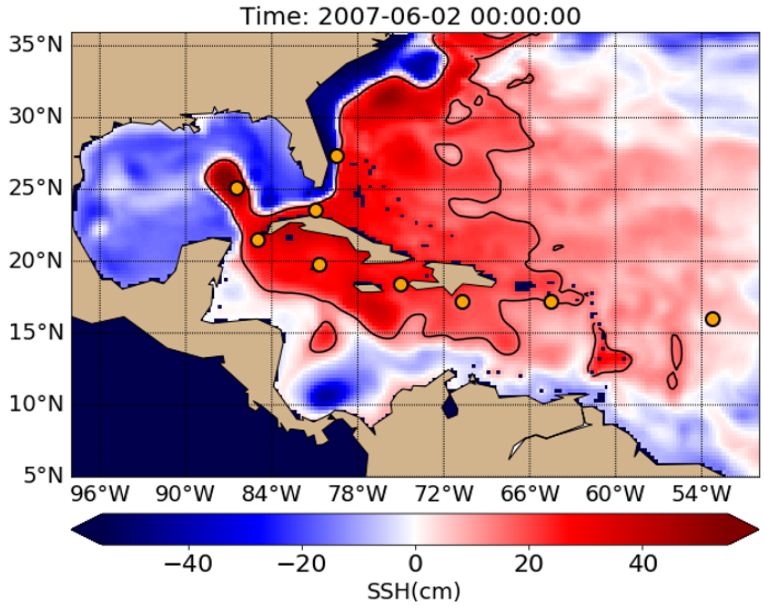

FIGURE 4.16: Locations of the route for the Hovmollers of entropy; the route follow the mean flow of the region. The orange dots show the route represented in figure 4.17.

In the first panel that includes all the frequencies, we observe several minima of entropy propagation along the period of study. We observe that large minimum entropy propagation events usually start east of the Antilles and spread through the Caribbean Sea. Some events only reach the Yucatan Channel (e.g., 2005, 2009), and others affect the Florida Strait (e.g., 1998, 2000, 2010), all without visibly affecting the LC entropy. These types of far-reaching propagation events of minimal entropy can also be observed in the Hovmoller of LF, some of which appear to have a component in HF, and no effect on MSC entropy.

We observe a large amount of maximum and minimum entropy propagation at various time scales, regions, and different durations of time. These events of propagation of minimum entropy, are important because they can be an indicator of information propagation between regions, that is, events that were forced by the atmosphere and that take the information to another region. Further research is needed to relate this propagation of minimal entropy to physical processes in both the ocean and the atmosphere, and to evaluate the potential predictability in the region.

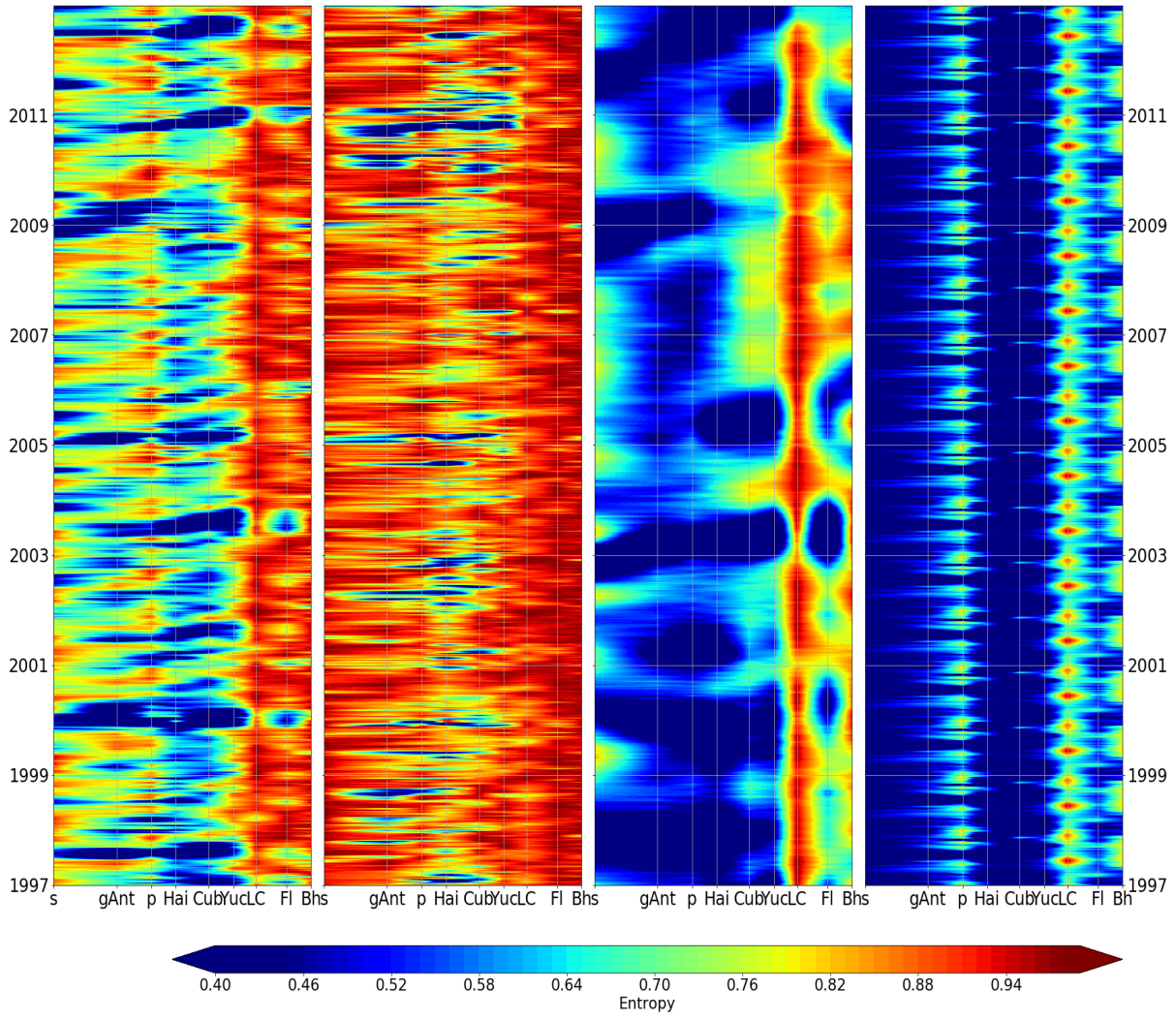

FIGURE 4.17: Hovmuller at different frequencies of entropy following the route orange in figure 4.16. From left to right: All-frequencies Entropy, HF entropy, LF entropy and MSC entropy.

Chapter 5

Conclusions

The goal of this study was to disentangle the influences of intrinsic/chaotic ocean processes and of the atmospheric variability on the variability in the Gulf of Mexico and surrounding regions. The scales of interest range from daily to interannual time scales, and from mesoscale to about a thousand kilometers. The variability of this oceanic basin, and of the Gulf of Mexico (GoM) in particular, is indeed driven by atmospheric processes (winds, heat and freshwater fluxes), but also by dynamical nonlinearities that spontaneously generate an intrinsic variability with a chaotic character within the ocean over this range of scales. We have separated both variability sources and quantified them separately as a first step. We re-addressed this question more rigorously as a second step, taking into account the specific features of the region's variability (non-Gaussianity) and avoiding the questionable separation between forced and intrinsic variability.

We addressed these questions via the analysis of a large (50-member) ensemble of 20-year eddy-permitting ($1/4^\circ$ resolution) primitive equation model simulations, where all ensemble members were subject to slight initial perturbations, and then driven by the same realistic atmospheric forcing. As discussed below, however, the $1/4^\circ$ resolution is too coarse to explicitly represent structures smaller than about 180 km, and their contribution to the regional dynamics. A careful assessment of the ensemble simulation was performed, revealing a rather good agreement between the model results with altimeter and other observations, over a large range of scales. More importantly, the model's ensemble dimension brought many benefits for the analysis of the forced, intrinsic, or sometimes mixed nature of the oceanic variability features in the region.

Our main results can be summarized as follows:

- We showed that the simulated variability approximately matches observations in magnitude and spatial distribution. By comparing the AVISO altimeter observations with the ensemble simulation, we also found that observed time series of Sea Level Anomaly (SLA) are probably not long enough presently to yield a robust description of the dynamics of the Loop Current (LC), in particular the

timing of eddy sheddings. This is supported by two findings: the first is that different altimetric products (on similar periods) do not provide similar statistics about the timing of eddy sheddings, which suggests that these statistics rely on too few observed events. The second finding is that besides the fact that the set of 50 simulated eddy shedding statistics is consistent with the observed statistics, these statistics differ a lot among the members despite their identical dynamics and forcing. This suggests that these 50 statistical descriptions of the LC dynamics over about 20 years are too dependent on the actual trajectory followed by each member, itself sensitive to slight initial perturbations. In other words, the simulation suggests that the currently available altimeter dataset may not be long enough to ensure that statistics of LC eddy sheddings robustly characterize the dynamics of the LC. They seem to be overly sensitive to the particular realization that the real or simulated ocean has picked among the range of possible evolutions (simulated by the ensemble simulation) over this period.

- We first used simple Gaussian metrics as in previous studies (e.g., Leroux et al., 2018) to separate and quantify the intensity of both variability components, considering that the ensemble mean represents the forced variability shared by all members, and that the dispersion among ensemble members represents the intrinsic variability of the ocean. By comparing the intensity of the forced and intrinsic variabilities, we identified locations such as the Gulf Stream (GS), the Loop Current (LC), and the GoM, where the intrinsic variability largely dominates, without any substantial contribution of the atmospheric variability to the variability of the ocean. These regions are indeed mostly characterized by a strong mesoscale activity, which generates intrinsic variability at high frequency and relatively small scales, and which then cascades towards larger scales, feeding a strong intrinsic variability at scales up to decadal and O(1000 km).

Our results also highlight regions where the oceanic variability is dominantly forced over most time scales. In shallow regions and over the shelves of the GoM in particular, the atmospheric variability exerts a strong constraint on the subannual oceanic variability, and dominates the intrinsic component. Although the latter component does exist there, it is likely that the shallow depth of these regions makes the coastal ocean more responsive to the atmospheric forcing, and in particular extreme winds during storms and hurricanes. We noted that intrinsic variability is likely to be underestimated there, since the modest resolution prevents the model from accurately resolving the main source of chaotic variability (mesoscale turbulence) in areas where shallow depths reduces the Rossby radius

and thus the size of actual eddies.

Our results further confirm that at interannual time scales as well, intrinsic variability cannot be neglected in most parts of the region with respect to the forced variability. Low frequency intrinsic variability even dominates its forced counterpart in the GS, the LC, and the western GoM. Regions of large LF intrinsic variability have been highlighted previously (e.g., Penduff et al., 2011). Moreover, such regions are mostly localized where intrinsic variability is strong at HF as well; Sérazin et al. (2018) indeed showed that oceanic nonlinearities (momentum advection) in eddy active regions can induce a temporal inverse cascade of kinetic energy which feeds the LF intrinsic variability from mesoscale activity. Our results thus support this dynamical scenario.

The fact that the Mean Seasonal Cycle (MSC) can substantially differ among the ensemble members is surprising at first sight. Indeed, the MSC is a priori fully controlled by a non-oceanic driver: it is driven by the atmospheric forcing, and is strong in all members. The difference in MSCs among the members may be explained again by the temporal inverse cascade, which tranfers chaotic kinetic energy from subannual mesoscale variability to interannual time scales across the 1-year period. This could explain why the MSC is affected by chaotic variability as well, but relatively less than at HF and LF since its forced component is large.

- We found that in the Subtropical North Atlantic there are several areas where the daily ensemble PDFs of the Sea Level Anomaly (SLA) do not have a Gaussian distribution, so that the simple use of ensemble means and standard deviations does not provide enough and accurate information about the ocean variability. We proposed a new metric based on the information theory (the Entropy) that can be used to characterize and study more complex ensemble evolutions in both Gaussian and non-Gaussian cases. Another advantage of this approach is that intrinsic and forced variabilities do not require any artificial splitting, a conceptual step that is made most of the time when diagnosing ensemble simulations, but that is not supported by the dynamical systems theory (see e.g., Pierini et al., 2018). Our entropy metric measures the time-varying constraint exerted by the atmosphere on the ocean's chaotic variability, without the need to crudely split the variability as in the previous approach. In our application, this entropy metric measures every day at each grid-point the information brought by the atmosphere (with respect to

the ensemble of all possible states) to describe the current ocean state.

The temporal means and standard deviations of entropy allowed us to identify regions such as the Gulf Stream and the Loop Current, where the atmospheric constraint on the ocean chaotic variability is constantly weak. On the contrary, the average and standard deviation of entropy indicate significant fluctuations of this atmospheric constraint on the chaotic variability in the coastal areas of the GoM, around the Antilles and east of the Lesser Antilles. The strength and fluctuating nature of this atmospheric constraint on the oceanic chaotic variability was then investigated separately for high and low-frequency SLA variabilities.

In the case of High-Frequency SLA, we showed that hurricanes and winter storms are able to force in all members simultaneous storm surges where they hit the GoM coastline, hence driving sharp drops in entropy (strong instantaneous constraint by the atmosphere). These entropy minima then travel in an anti-clockwise direction around the GoM coastline as coastally-trapped waves which progressively decay. Storms blowing over deep waters elsewhere in the tropical Atlantic also yield sharp entropy decreases, which decay as the ambient chaotic variability progressively takes over the sharp storm-driven changes in the SLA ensemble PDFs.

At Low-Frequency, we observe slower atmospherically-driven reductions in entropy that occur at larger scale, especially around the Greater Antilles, where low-frequency SLA entropy minima emerge and propagate through the Caribbean Sea into the GoM, and sometimes up to the Florida Current. The specific atmospheric drivers of these fluctuations of the entropy of the low frequency SLA have not yet been identified and interpreted physically; this will require further research.

- Our results show that the Gaussian and non-Gaussian metrics provide very consistent results, with an almost linear relationship of these metrics: high intrinsic variability (large σ_I/σ_T) means large mean entropy and weak constraint of the atmospheric variability on the ocean. Our entropy metric is not only consistent with the σ_I/σ_T ratio; it has three advantages over it. [1] It is in line with the Dynamical System Theory since no questionable splitting between forced and intrinsic variability is made. [2] Entropy is more general than the σ_I/σ_T ratio since it is valid in both Gaussian and non-Gaussian cases;[3] the entropy naturally provides the time

dependence of the atmospheric constraint exerted on the chaotic oceanic variability. Identifying the origin of the relationship between Gaussian and non-Gaussian metrics would require analytical development, which is left for the future.

Possible limitations of the study

This study took advantage of a 50-member ensemble of eddy-permitting ocean simulations and led to various results about the origin, structure, and features of the ocean variability in the GoM. What are the limitations of this numerical dataset regarding the robustness of our results, and would a different model approach have led to substantially different results?

One may first wonder whether the $1/4^\circ$ model resolution, which remains modest by today's standards, represents a significant limitation for this study. Le Hénaff et al. (2012) for instance used a one-member $1/25^\circ$ model to study the Loop Current dynamics, and showed a substantial contribution of small-scale frontal eddies that develop along the edge of the Loop Current and the LC Eddy sheddings. Such structures are not captured at $1/4^\circ$ resolution; their suggested impact on the intensification of Loop Current Eddies and their shedding sequence (two processes that are involved in the chaotic GoM variability) would be probably represented with more realism at finner resolution. It is important to note, however, that the simulation we used required 400000 hours CPU: its ensemble dimension explains this large cost, which was crucial for our study. Dividing by six the model grid size to reach a resolution of $1/24^\circ$ as in Le Hénaff et al. (2012) while keeping the benefits of 50 members would multiply the simulation cost by about $6^3 = 216$, which lies beyond the limits of computational resources available to us. Nevertheless, we showed in chapter 3 that the model variability compares well with altimeter observations regarding several metrics, in particular in the Loop Current. Despite the limited model resolution, this shows that the main processes and dynamical features in the basin are correctly simulated for the purpose of this study.

One may also wonder whether 50 members are numerous enough to characterize the complex variability of the region and, in particular, of the Loop Current. The number of degrees of freedom of the chaotic ocean is certainly much larger than 50, but further increasing the ensemble size would of course lead to additional CPU costs. Nevertheless, the size of our ensemble is larger than other ensemble model studies in the region (e.g., Yu et al., 2019, 20 members) and our period of integration is much longer than in other studies (e.g. Hoteit et al., 2013, up to 200 members, but only 6 months). We also showed that 50 members is adequate to characterize the daily evolution of the system

entropy (section 2.5.2, Fig. 2.10), and relatively complex (bimodal) behaviors. Since in addition the uncertainty of ensemble statistics (mean and standard deviation, see e.g. Leroux et al., 2018) decreases as the inverse of the square root of the ensemble size, one would need $4x50 = 200$ members to divide by 2 this uncertainty.

This simulation is thus a compromise between model resolution and ensemble size given the available computational power. It is clear that a higher resolution model would improve the representation of the dynamics, and that a larger ensemble would improve the statistical description of the variability. However each of these changes would strongly increase the computational cost of the integration and of the post-processing, with no obvious benefits regarding the conceptual part of this study and its qualitative results. Note that a restriction of the model domain on the GoM itself would allow a substantial increase in resolution and/or ensemble size, but the intrinsic variability produced far upstream (e.g. in the Brazil Current retroflection or in the Caribbean Sea) and influencing the GoM dynamics would be missing.

These arguments and the results of our assessment chapter thus suggest that the 50-member and $1/4°$-resolution compromise was reasonable, and adequate for the present study. Testing the robustness of our results to the ensemble model configuration will require comparisons with existing (and future) ensemble simulations of the region, at various resolutions and with different models; this is left for future studies.

5.1 Perspectives

The analysis of ocean simulation ensembles and of the links between the atmospheric forcing and the oceanic intrinsic variability are quite new: in this study we have investigated certain questions in this context but many others remain open. Let us cite a few of them, focusing only on physical oceanography.

An interesting question to investigate in the future concerns the features and mechanisms of propagation of forced and intrinsic variabilities, into and out of the Gulf of Mexico. Several studies have indeed suggested a relationship between the variability in the Loop Current and in the Caribbean Sea, via the transport of volume or vorticity through the Yucatan Channel (e.g., Bunge et al., 2002; Candela et al., 2002; Oey, 2004; Lin et al., 2009; Lin et al., 2012; Mildner et al., 2013; Nedbor-Gross et al., 2014). Some authors even relate the variability observed in the Yucatan Channel with the variability observed in the North Brazil Current retroflection (Westen et al., 2018). However, in

general these authors did not use ensemble simulations to characterize the intrinsic or forced origin of such remote influences. We have documented some propagating signals from entropy analyses, which could be further analyzed in terms of physical processes. Further analyzing the ensemble simulation could provide new information about the propagation of the intrinsic variability produced in the North Brazil Current or in the Caribbean Sea toward the Loop Current, the Gulf of Mexico, and the Florida Current.

Some studies have demonstrated the impact of the LC variability on the transport in the Florida Straits and the Florida-Bahamas Strait (e.g., Lin et al., 2010; P. S. Fratantoni., 1998). Some other authors (Hirschi et al., 2019) reported a distant influence of the LC transport variability on the surface velocity at Cape Hatteras and in the Gulf Stream extension, suggesting a potential predictability of the variability in the latter region from the monitoring of the LC evolution. Again, the use of an ensemble simulation and of entropy analyses could be interesting to further analyze these links in terms of intrinsic and forced components, and to disentangle the respective contributions of the LC intrinsic variability and of the atmospheric forcing in such remote connections.

In this thesis, we mostly reported on the surface variability as seen in sea level. However, we conducted some preliminary analyses of the link between the atmospherically-modulated chaotic LC fluctuations, and the transports across the Gulf of Mexico boundaries in two layers. Further developments in statistical methodologies, and additional analyses in the vertical would help complement our first results, which illustrate the propagation of forced and intrinsic signals into and out of the Gulf of Mexico at different depths and different time scales.

Beyond these perspectives, it would be important to identify the physical mechanisms associated with the ensemble behavior that we characterized in this thesis. We have studied probabilistically the response of the ocean to storms and hurricanes, and showed how extreme winds modulate the high-frequency intrinsic variability along the coasts. However, dedicated process studies need to be conducted to precisely identify the mechanisms involved in other phenomena we reported about, such as the atmospheric modulation of the Loop Current chaotic evolution, or the emergence and slow propagation of low-frequency entropy anomalies. It is likely that such studies would benefit from the ensemble dimension of the simulation, since it provides information about the external and internal drivers of the oceanic evolution; however, a methodology needs to be built to adapt classical approaches used in process studies (analysis of terms in budgets, Reynolds decompositions, etc) to the ensemble context. The use of

Reynolds decompositions in the ensemble dimension may be useful in this regard.

We have shown that the variability in our region of interest is the complex result of intrinsic/chaotic oceanic dynamics modulated by the atmosphere. The interplay between these two drivers remains to be studied in more detail. Ensemble simulations are promising to progress on such questions, but their analysis is not straightforward: additional research is needed on statistical methods and diagnostics, on the physical processes at work, and to identify the implications of the present results e.g. in terms of predictability, or for operational applications.

Bibliography

Athié, Gabriela, Julio Sheinbaum, Robert Leben, José Ochoa, Michael R. Shannon, and Julio Candela (2015). "Interannual variability in the Yucatan Channel flow". In: *Geophysical Research Letters* 42.5, pp. 1496–1503. ISSN: 19448007. DOI: 10.1002/2014GL062674.

Baringer, Molly O.Neil and Jimmy C. Larsen (2001). "Sixteen years of Florida current transport at 27° N". In: *Geophysical Research Letters* 28.16, pp. 3179–3182. ISSN: 00948276. DOI: 10.1029/2001GL013246.

Barnier, Bernard, Gurvan Madec, et al. (2006). "Impact of partial steps and momentum advection schemes in a global ocean circulation model at eddy-permitting resolution". In: *Ocean Dynamics* 56.5-6, pp. 543–567. DOI: 10.1007/s10236-006-0082-1.

Barnier, Bernard, Thierry Reynaud, Aike Beckmann, Claus Böning, Jean Marc Molines, Sally Barnard, and Yanli Jia (2001). "On the seasonal variability and eddies in the North Brazil Current: Insights from model intercomparison experiments". In: *Progress in Oceanography* 48.2-3, pp. 195–230. ISSN: 00796611. DOI: 10.1016/S0079-6611(01)00005-2.

Bessières, Laurent, Stéphanie Leroux, Jean Michel Brankart, Jean Marc Molines, Marie Pierre Moine, Pierre Antoine Bouttier, Thierry Penduff, Laurent Terray, Bernard Barnier, and Guillaume Sérazin (2017). "Development of a probabilistic ocean modelling system based on NEMO 3.5: Application at eddying resolution". In: *Geoscientific Model Development* 10.3, pp. 1091–1106. ISSN: 19919603. DOI: 10.5194/gmd-10-1091-2017.

Bilskie, Matthew V; S.C. Hagen, S.C. Medeiros, A.T. Cox, M. Salisbury, and D. Coggin (2016). "Data and numerical analysis of astronomic tides, wind-waves, and hurricane stormsurge along the northern Gulf of Mexico". In: *Journal of Geophysical Research : Oceans* 121, pp. 3625–3658. ISSN: 21699275. DOI: 10.1002/2015JC011421.Received.

Brankart, J. M., G. Candille, F. Garnier, C. Calone, A. Melet, P. A. Bouttier, P. Brasseur, and J. Verron (2015). "A generic approach to explicit simulation of uncertainty in the NEMO ocean model". In: *Geoscientific Model Development* 8.5, pp. 1285–1297. ISSN: 19919603. DOI: 10.5194/gmd-8-1285-2015.

Bunge, L., José Ochoa, Antonio Badan, Julio Candela, and Julio Sheinbaum (2002). "Deep flows in the Yucatan Channel and their relation to changes in the Loop Current extension". In: *Journal of Geophysical Research* 107.C12, pp. 1–7. ISSN: 0148-0227. DOI: 10.1029/2001JC001256.

Candela, J., J. Ochoa, J. Sheinbaum, M. López, P. Pérez, M. Tenreiro, E. Pallàs-Sanz, G. Athie, and L. Arriaza-Oliveros (2019). "The flow through the Gulf of Mexico". In: *Journal of Physical Oceanography* 49.6, pp. 1381–1401. ISSN: 0022-3670. DOI: 10.1175/JPO-D-18-0189.1. URL: http://journals.ametsoc.org/doi/10.1175/JPO-D-18-0189.1.

Candela, Julio, Julio Sheinbaum, José Ochoa, and Antoine Badan (2002). "The potential vorticity flux through the Yucatan Channel and the Loop Current in the Gulf of Mexico". In: *Geophysical Research Letters* 29.22, p. 2059. ISSN: 0094-8276. DOI: 10.1029/2002GL015587.

Candela, Julio, Sorayda Tanahara, Michel Crepon, Bernard Barnier, and Julio Sheinbaum (2003). "Yucatan Channel flow: Observations versus CLIPPER ATL6 and MERCATOR PAM models". In: *Journal of Geophysical Research* 108.C12, p. 3385. ISSN: 0148-0227. DOI: 10.1029/2003JC001961.

Cardona, Yuley and Annalisa Bracco (2016). "Predictability of mesoscale circulation throughout the water column in the Gulf of Mexico". In: *Deep-Sea Research Part II: Topical Studies in Oceanography* 129, pp. 332–349. ISSN: 09670645. DOI: 10.1016/j.dsr2.2014.01.008. URL: http://dx.doi.org/10.1016/j.dsr2.2014.01.008.

Chang, Y-L. and L-Y. Oey (2010a). "Eddy and Wind-Forced Heat Transports in the Gulf of Mexico". In: *Journal of Physical Oceanography* 40.12, pp. 2728–2742. ISSN: 0022-3670. DOI: 10.1175/2010JPO4474.1.

Chang, Y.-L. and L.-Y. Oey (2010b). "Why Can Wind Delay the Shedding of Loop Current Eddies?" In: *Journal of Physical Oceanography* 40.11, pp. 2481–2495. ISSN: 0022-3670. DOI: 10.1175/2010JPO4460.1.

— (2012). "Why does the Loop Current tend to shed more eddies in summer and winter?" In: *Geophysical Research Letters* 39.5, pp. 1–7. ISSN: 00948276. DOI: 10.1029/2011GL050773.

— (2013). "Coupled Response of the Trade Wind, SST Gradient, and SST in the Caribbean Sea, and the Potential Impact on Loop Current's Interannual Variability*". In: *Journal of Physical Oceanography* 43.7, pp. 1325–1344. ISSN: 0022-3670. DOI: 10.1175/JPO-D-12-0183.1. URL: http://journals.ametsoc.org/doi/abs/10.1175/JPO-D-12-0183.1.

Chassignet, Eric P. and Xiaobiao Xu (2017). "Impact of horizontal resolution (1/12° *to* 1/50°) on Gulf Stream separation, penetration, and variability". In: *Journal of Physical Oceanography* 47.8, pp. 1999–2021. DOI: 10.1175/JPO-D-17-0031.1.

Chérubin, Laurent M., Yves Morel, and Eric P. Chassignet (2006). "Loop Current Ring Shedding: The Formation of Cyclones and the Effect of Topography". In: *Journal of Physical Oceanography* 36, pp. 569–591.

Cleveland, William S. (1979). "Robust locally weighted regression and smoothing scatterplots". In: *Journal of the American Statistical Association* 74.368, pp. 829–836. ISSN: 1537274X. DOI: 10.1080/01621459.1979.10481038.

Cover, Thomas M. and Joy A. Thomas (2006). *Elements of Information Theory, Second Edition*. New York, NY, USA: Wiley-Interscience, p. 576. ISBN: 9780471748823. DOI: 10.1002/047174882X.

Cunningham, S., T. Kanzow, et al. (2007). "Temporal variability of the Atlantic meridional overturning circulation at 26.5N". In: *Science* 317.5840, pp. 935–8. ISSN: 1095-9203. DOI: 10.1126/science.1141304. URL: http://www.ncbi.nlm.nih.gov/pubmed/17702940.

Dijkstra, Henk a and Michael Ghil (2005). "Low-Frequency Variability of the Large-Scale Ocean Circulation: A Dynamical Systems Approach". In: *Reviews of Geophysics* 43.RG3002, pp. 1–38. ISSN: 87551209. DOI: 10.1029/2002RG000122.1.INTRODUCTION.

DiMarco, S F, Jr. W D Nowlin, and R O Reid (2005). "A statistical desciption of the near-surface velocity field from drifters in the Gulf of Mexico". In: *Circulation in the Gulf of Mexico: observations and models*, p 101–10.

DiMego, Geoffrey J., Lance F. Bosart, and G William Endersen (1976). "An examination of the frequency and mean conditions surrounding frontal incursions into the Gulf of Mexico and Caribbean Sea". In: *Monthly Weather Review* 104.6.

Drijfhout, Sybren, Wilco Hazeleger, Frank Selten, and Rein Haarsma (2008). "Future changes in internal variability of the Atlantic Meridional Overturning Circulation". In: *Climate Dynamics* 30.4, pp. 407–419. ISSN: 09307575. DOI: 10.1007/s00382-007-0297-y.

Dubranna, Jean, Paula Pérez-Brunius, Manuel López, and Julio Candela (2011). "Circulation over the continental shelf of the western and southwestern Gulf of Mexico". In: *Journal of Geophysical Research* 116.C8, p. C08009. ISSN: 0148-0227. DOI: 10.1029/2011JC007007. URL: http://doi.wiley.com/10.1029/2011JC007007.

Dukhovskoy, Dmitry S., Robert R. Leben, Eric P. Chassignet, Cody A. Hall, Steven L. Morey, and Robert Nedbor-Gross (2015). "Characterization of the uncertainty of loop current metrics using a multidecadal numerical simulation and altimeter observations". In: *Deep-Sea Research Part I: Oceanographic Research Papers* 100, pp. 140–

158. ISSN: 09670637. DOI: 10.1016/j.dsr.2015.01.005. URL: http://dx.doi.org/10.1016/j.dsr.2015.01.005.

Dussin, Raphael, Bernard Barnier, Laurent Brodeau, and Jean Marc Molines (2016). *The Making Of the DRAKKAR FORCING SET DFS5*. Tech. rep. April, pp. 1–34.

Ezer, Tal, Lie-Yauw Oey, and Hyun Chul Lee (2003). "The variability of currents in the Yucatan Channel: Analysis of results from a numerical ocean model". In: *Journal of Geophysical Research* 108.C1, p. 3012. ISSN: 0148-0227. DOI: 10.1029/2002JC001509. URL: http://doi.wiley.com/10.1029/2002JC001509.

Gómez-Valdivia, Felipe and Alejandro Parés-Sierra (2020). "Seasonal Upper Shelf Circulation Along the Central Western Gulf of Mexico : A Preferential Upcoast Flow Reinforced by the Recurrent Arrival of Loop Current Eddies". In: *Journal of Geophysical Research : Oceans*, pp. 1–19. DOI: 10.1029/2019JC015596.

Grégorio, Sandy, Thierry Penduff, Guillaume Sérazin, Jean-Marc Molines, Bernard Barnier, and Joël Hirschi (2015). "Intrinsic Variability of the Atlantic Meridional Overturning Circulation at Interannual-to-Multidecadal Time Scales". In: *Journal of Physical Oceanography* 45.October 2016, pp. 1929–1946. ISSN: 0022-3670. DOI: 10.1175/JPO-D-14-0163.1.

Hall, Cody A. and Robert R. Leben (2016). "Observational evidence of seasonality in the timing of loop current eddy separation". In: *Dynamics of Atmospheres and Oceans* 76, pp. 240–267. ISSN: 03770265. DOI: 10.1016/j.dynatmoce.2016.06.002. URL: http://dx.doi.org/10.1016/j.dynatmoce.2016.06.002.

Hamilton, Peter, G. S. Fargion, and D. C. Biggs (1999). "Loop Current Eddy Paths in the Western Gulf of Mexico". In: *Journal of Physical Oceanography* 29, pp. 1180–1207.

Hamilton, Peter, Jimmy C Larsen, Kevin D Leaman, Thomas N Lee, and Evans Waddell (2005). "Transports through the Straits of Florida". In: *Journal of Physical Oceanography* 35.3, pp. 308–322. ISSN: 0022-3670. DOI: 10.1175/JPO-2688.1.

Hirschi, Joël J.M., Eleanor Frajka-Williams, et al. (2019). "Loop current variability as trigger of coherent gulf stream transport anomalies". In: *Journal of Physical Oceanography* 49.8, pp. 2115–2132. ISSN: 15200485. DOI: 10.1175/JPO-D-18-0236.1.

Hoteit, Ibrahim, Tim Hoar, Ganesh Gopalakrishnan, Nancy Collins, Jeffrey Anderson, Bruce Cornuelle, Armin Köhl, and Patrick Heimbach (2013). "A MITgcm/DART ensemble analysis and prediction system with application to the Gulf of Mexico". In: *Dynamics of Atmospheres and Oceans* 63, pp. 1–23. ISSN: 03770265. DOI: 10.1016/j.dynatmoce.2013.03.002. URL: http://dx.doi.org/10.1016/j.dynatmoce.2013.03.002.

Huot, Pierre-Vincent (2016). "Contribution du chaos et du forçage atmosphérique à la variabilité de l'océan du golfe du Mexique". PhD thesis, p. 31.

Johns, William E, Thomas N Lee, Friedrich A Schott, Rainer J Zantopp, and Robert H Evans (1990). "The North Brazil Current retroflection: Seasonal structure and eddy variability". In: *Journal of Geophysical Research* 95.C12, pp. 22103–22120. DOI: https://doi.org/10.1029/JC095iC12p22103.

Johns, William E., Tamara L. Townsend, David M. Fratantoni, and W. Douglas Wilson (2002). "On the Atlantic inflow to the Caribbean Sea". In: *Deep-Sea Research Part I: Oceanographic Research Papers* 49.2, pp. 211–243. ISSN: 09670637. DOI: 10.1016/S0967-0637(01)00041-3.

Jouanno, Julien, José Ochoa, Enric Pallàs-Sanz, Julio Sheinbaum, Fernando Andrade-Canto, Julio Candela, and Jean-Marc Molines (2016). "Loop Current Frontal Eddies: Formation along the Campeche Bank and Impact of Coastally Trapped Waves". In: *Journal of Physical Oceanography* 46.11, pp. 3339–3363. ISSN: 0022-3670. DOI: 10.1175/JPO-D-16-0052.1. URL: http://journals.ametsoc.org/doi/10.1175/JPO-D-16-0052.1.

Jouanno, Julien, Julio Sheinbaum, Bernard Barnier, and Jean Marc Molines (2009). "The mesoscale variability in the Caribbean Sea. Part II: Energy sources". In: *Ocean Modelling* 26.3-4, pp. 226–239. ISSN: 14635003. DOI: 10.1016/j.ocemod.2008.10.006. URL: http://dx.doi.org/10.1016/j.ocemod.2008.10.006.

Jouanno, Julien, Julio Sheinbaum, Bernard Barnier, Jean Marc Molines, Laurent Debreu, and Florian Lemarié (2008). "The mesoscale variability in the Caribbean Sea. Part I: Simulations and characteristics with an embedded model". In: *Ocean Modelling* 23.3-4, pp. 82–101. ISSN: 14635003. DOI: 10.1016/j.ocemod.2008.04.002.

Le Hénaff, Matthieu Le, Vassiliki H Kourafalou, Yves Morel, and Ashwanth Srinivasan (2012). "Simulating the dynamics and intensification of cyclonic Loop Current Frontal Eddies in the Gulf of Mexico". In: *Journal of Geophysical Research* 117.C02034, pp. 1–20. DOI: 10.1029/2011JC007279.

Le Sommer, Julien, Thierry Penduff, Sébastien Theetten, Gurvan Madec, and Bernard Barnier (2009). "How momentum advection schemes influence current-topography interactions at eddy permitting resolution". In: *Ocean Modelling* 29.1, pp. 1–14. ISSN: 14635003. DOI: 10.1016/j.ocemod.2008.11.007. URL: http://dx.doi.org/10.1016/j.ocemod.2008.11.007.

Leben, Robert R (2005). "Altimeter-Derived Loop Current Metrics". In: *Geophysical Monograph Series*.

Leroux, Stephanie, Thierry Penduff, Laurent Bessières, Jean Marc Molines, Jean Michel Brankart, Guillaume Sérazin, Bernard Barnier, and Laurent Terray (2018). "Intrinsic and atmospherically forced variability of the AMOC: Insights from a large-ensemble

ocean hindcast". In: *Journal of Climate* 31.3, pp. 1183–1203. ISSN: 08948755. DOI: 10.1175/JCLI-D-17-0168.1.

Lin, Yuehua, Richard J. Greatbatch, and Jinyu Sheng (2009). "A model study of the vertically integrated transport variability through the Yucatan Channel: Role of Loop Current evolution and flow compensation around Cuba". In: *Journal of Geophysical Research: Oceans* 114.8, pp. 1–14. ISSN: 21699291. DOI: 10.1029/2008JC005199..

— (2010). "The influence of Gulf of Mexico loop current intrusion on the transport of the Florida Current". In: *Ocean Dynamics* 60.5, pp. 1075–1084. ISSN: 16167341. DOI: 10.1007/s10236-010-0308-0.

Lin, Yuehua, Jinyu Sheng, and Richard J. Greatbatch (2012). "A numerical study of the circulation and monthly-to-seasonal variability in the Caribbean Sea: The role of Caribbean eddies". In: *Ocean Dynamics* 62.2, pp. 193–211. ISSN: 16167341. DOI: 10.1007/s10236-011-0498-0.

Lucas, Marc A., Nadia Ayoub, Bernard Barnier, Thierry Penduff, and Pierre de Mey (2008). "Stochastic study of the temperature response of the upper ocean to uncertainties in the atmospheric forcing in an Atlantic OGCM". In: *Ocean Modelling* 20.1, pp. 90–113. ISSN: 14635003. DOI: 10.1016/j.ocemod.2007.07.006.

Lugo-Fernández, Alexis and Robert R. Leben (2010). "On the Linear Relationship between Loop Current Retreat Latitude and Eddy Separation Period". In: *Journal of Physical Oceanography* 40.12, pp. 2778–2784. ISSN: 0022-3670. DOI: 10.1175/2010JPO4354.1. URL: http://journals.ametsoc.org/doi/abs/10.1175/2010JPO4354.1.

Lugo-Fernández, Alexis, Robert R. Leben, and Cody A. Hall (2016). "Kinematic metrics of the Loop Current in the Gulf of Mexico from satellite altimetry". In: *Dynamics of Atmospheres and Oceans* 76, pp. 268–282. ISSN: 03770265. DOI: 10.1016/j.dynatmoce.2016.01.002. URL: http://dx.doi.org/10.1016/j.dynatmoce.2016.01.002.

Maul, G. (1977). "The annual cycle of the Gulf Loop Current, Part 1 : observations during a one-year time series". In: *Journal of Marine Research* 35, pp. 29–47.

Maul, George a. and Fred M. Vukovich (1993). "The Relationship between Variations in the Gulf of Mexico Loop Current and Straits of Florida Volume Transport". In: *Journal of Physical Oceanography* 23, pp. 785–796. ISSN: 0022-3670. DOI: 10.1175/1520-0485(1993)023<0785:TRBVIT>2.0.CO;2.

Meinen, Christopher S. and Douglas S. Luther (2016). "Structure, transport, and vertical coherence of the Gulf Stream from the Straits of Florida to the Southeast Newfoundland Ridge". In: *Deep-Sea Research Part I: Oceanographic Research Papers* 112, pp. 137–154. ISSN: 09670637. DOI: 10.1016/j.dsr.2016.02.005. URL: http://dx.doi.org/10.1016/j.dsr.2016.03.002.

Mildner, Tanja C., Carsten Eden, and Lars Czeschel (2013). "Revisiting the relationship between loop current rings and Florida Current transport variability". In: *Journal of Geophysical Research: Oceans* 118.12, pp. 6648–6657. ISSN: 21699291. DOI: 10.1002/2013JC009109.

Morey, Steven L., Jorge Zavala-Hidalgo, and James J. O'Brien (2005). "The Seasonal Variability of Continental Shelf Circulation in the Northern and Western Gulf of Mexico from a High-Resolution Numerical Model". In: *Circulation in the Gulf of Mexico: Observations and Models*, pp. 203–218. ISSN: 23288779. DOI: 10.1029/161GM16.

Murphy, Sylvia J., Harley E. Hurlburt, and James J. O'Brien (1999). "The connectivity of eddy variability in the Caribbean Sea, the Gulf of Mexico, and the Atlantic Ocean". In: *Journal of Geophysical Research: Oceans* 104.C1, pp. 1431–1453. DOI: 10.1029/1998jc900010.

Nedbor-Gross, Robert, Dmitry S. Dukhovskoy, Mark a. Bourassa, Steven L. Morey, and Eric P. Chassignet (2014). "Investigation of the Relationship Between the Yucatan Channel Transport and the Loop Current Area in a Multidecadal Numerical Simulation". In: *Marine Technology Society Journal* 48.4, pp. 15–26. ISSN: 00253324. DOI: 10.4031/MTSJ.48.4.8.

Oey, L.-Y. (2003). "Effects of winds and Caribbean eddies on the frequency of Loop Current eddy shedding: A numerical model study". In: *Journal of Geophysical Research* 108.C10, pp. 1–25. ISSN: 0148-0227. DOI: 10.1029/2002JC001698.

— (2004). "Vorticity flux through the Yucatan Channel and Loop Current variability in the Gulf of Mexico". In: *Journal of Geophysical Research C: Oceans* 109.10, pp. 1–10. ISSN: 01480227. DOI: 10.1029/2004JC002400.

Oey, L-Y, T Ezer, and H-C Lee (2005). "Loop Current , Rings and Related Circulation in the Gulf of Mexico : A Review of Numerical Models and Future Challenges". In: *Circulation in the Gulf of Mexico: Observations nad Models* 161, pp. 31–56. DOI: 10.1029/161GM04.

P. S. Fratantoni., Thomas N. Lee (1998). "The Influence of Loop Current Perturbations on the Formation and Evolution of Tortugas Eddies in the Southern Straits of Florida". In: *Journal of Geophysical Research* 103.

Penduff, T., M. Juza, L. Brodeau, G. C. Smith, B. Barnier, J. M. Molines, A. M. Treguier, and G. Madec (2010). "Impact of global ocean model resolution on sea-level variability with emphasis on interannual time scales". In: *Ocean Science* 6.1, pp. 269–284. ISSN: 18120792. DOI: 10.5194/os-6-269-2010.

Penduff, Thierry, Mélanie Juza, Bernard Barnier, Jan Zika, William K. Dewar, Anne Marie Treguier, Jean Marc Molines, and Nicole Audiffren (2011). "Sea level expression of intrinsic and forced ocean variabilities at interannual time scales". In: *Journal of Climate* 24.21, pp. 5652–5670. DOI: 10.1175/JCLI-D-11-00077.1.

Penduff, Thierry, Julien Le Sommer, Jean-Marc Molines, Jean-Michel Brankart, and Aurelie Albert (2020). *Evolution of CMEMS Global High Resolution MFC Trimestrial progress report*. Tech. rep.

Pérez-Brunius, Paula, Paula García-Carrillo, Jean Dubranna, Julio Sheinbaum, and Julio Candela (2013). "Direct observations of the upper layer circulation in the southern Gulf of Mexico". In: *Deep Sea Research Part II: Topical Studies in Oceanography* 85, pp. 182–194. ISSN: 09670645. DOI: 10.1016/j.dsr2.2012.07.020. URL: http://linkinghub.elsevier.com/retrieve/pii/S0967064512001063.

Pierini, Stefano, Mickaël D. Chekroun, and Michael Ghil (2018). "The onset of chaos in nonautonomous dissipative dynamical systems: A low-order ocean-model case study". In: *Nonlinear Processes in Geophysics* 25.3, pp. 671–692. ISSN: 16077946. DOI: 10.5194/npg-25-671-2018.

Portela, Esther, M. Tenreiro, Enric Pallàs-Sanz, Thomas Meunier, Angel Ruiz-Angulo, Rosmery Sosa-Gutiérrez, and Simó Cusí (2018). "Hydrography of the Central and Western Gulf of Mexico". In: *Journal of Geophysical Research: Oceans* 123.8, pp. 5134–5149. ISSN: 21699291. DOI: 10.1029/2018JC013813.

Rivas, David (2017). "Wind-driven coastal-trapped waves off southern Tamaulipas and northern Veracruz, western Gulf of Mexico, during winter 2012–2013". In: *Estuarine, Coastal and Shelf Science* 185, pp. 1–10. ISSN: 02727714. DOI: 10.1016/j.ecss.2016.12.002. URL: http://dx.doi.org/10.1016/j.ecss.2016.12.002.

Rousset, Clément and Lisa M. Beal (2010). "Observations of the Florida and Yucatan Currents from a Caribbean Cruise Ship". In: *Journal of Physical Oceanography* 40.7, pp. 1575–1581. ISSN: 0022-3670. DOI: 10.1175/2010JPO4447.1. URL: http://journals.ametsoc.org/doi/abs/10.1175/2010JPO4447.1.

— (2011). "On the seasonal variability of the currents in the Straits of Florida and Yucatan Channel". In: *Journal of Geophysical Research: Oceans* 116.C08004, pp. 1–17. ISSN: 21699291. DOI: 10.1029/2010JC006679.

— (2014). "Closing the transport budget of the Florida Straits". In: *Geophysical Research Letters* 41.7, pp. 2460–2466. ISSN: 19448007. DOI: 10.1002/2014GL059498.

Schmitz, William J. and Michael S. McCartney (1993). "On the North Atlantic circulation". In: *Reviews of Geophyisics* 31.1, pp. 29–49. ISSN: 01466291. DOI: 10.1016/0146-6291(78)90650-1.

Sérazin, Guillaume, Alexandre Jaymond, Stéphanie Leroux, Thierry Penduff, Laurent Bessières, William Llovel, Bernard Barnier, Jean-Marc Marc Molines, and Laurent Terray (2017). "A global probabilistic study of the ocean heat content low-frequency variability: Atmospheric forcing versus oceanic chaos". In: *Geophysical Research Letters* 44.11, pp. 5580–5589. ISSN: 19448007. DOI: 10.1002/2017GL073026. URL: http://doi.wiley.com/10.1002/2017GL073026.

Sérazin, Guillaume, Thierry Penduff, Bernard Barnier, Jean Marc Molines, Brian K. Arbic, Malte Müller, and Laurent Terray (2018). "Inverse cascades of kinetic energy as a source of intrinsic variability: A global OGCM study". In: *Journal of Physical Oceanography* 48.6, pp. 1385–1408. ISSN: 15200485. DOI: 10.1175/JPO-D-17-0136.1.

Sheinbaum, Julio, Julio Candela, Antoine Badan, and J. Ochoa (2002). "Flow structure and transport in the Yucatan Channel". In: *Geophysical Research Letters* 29.3, pp. 1–6. ISSN: 0094-8276. DOI: 10.1029/2001GL013990.

Vázquez de la Cerda, A.M, Robert O Reid, Steven F. DiMarco, and A. E. Jochens (2005). "Bay of Campeche Circulation: An Update". In: *Geophysical Monograph Series* 161, pp. 279–293.

Velasco, Guillermo Gutiérrez de and Clinton D. Winant (1996). "Seasonal patterns of wind stress and wind stress curl over the Gulf of Mexico". In: *Journal of Geophysical Research* 101.C8, p. 18127. ISSN: 0148-0227. DOI: 10.1029/96JC01442. URL: http://doi.wiley.com/10.1029/96JC01442.

Vukovich, Fred M. (2007). "Climatology of ocean features in the Gulf of Mexico". In: *Bulletin of the American Meteorological Society* 88, pp. 156–157. ISSN: 00030007. DOI: 10.1175/JPO2989.1.

Westen, René M. van, Henk A. Dijkstra, et al. (2018). "Mechanisms of the 40–70 Day Variability in the Yucatan Channel Volume Transport". In: *Journal of Geophysical Research: Oceans* 123.2, pp. 1286–1300. ISSN: 21699291. DOI: 10.1002/2017JC013580.

Yu, Liuqian, Katja Fennel, Bin Wang, Arnaud Laurent, Keith R. Thompson, and Lynn K. Shay (2019). "Evaluation of nonidentical versus identical twin approaches for observation impact assessments: an ensemble-Kalman-filter-based ocean assimilation application for the Gulf of Mexico". In: *Ocean Science* 15.6, pp. 1801–1814. ISSN: 18120792. DOI: 10.5194/os-15-1801-2019.

Zavala-Hidalgo, Jorge, Rosario Romero-Centeno, Adriana Mateos-Jasso, Steven L. Morey, and Benjamín Martínez-López (2014). "The response of the Gulf of Mexico to wind and heat flux forcing: What has been learned in recent years?" In: *Atmósfera* 27.3, pp. 317–334. ISSN: 01876236. DOI: 10.1016/S0187-6236(14)71119-1. URL: http://dx.doi.org/10.1016/S0187-6236(14)71119-1.